

**Materials, Processes, and Characterization of Extended Air-gaps  
for the Intra-level Interconnection of Integrated Circuits**

A Dissertation  
Presented to  
The Academic Faculty

By

Seongho Park

In Partial Fulfillment  
Of the Requirements for the Degree  
Doctor of Philosophy in the School of Chemical and Biomolecular Engineering

Georgia Institute of Technology

May 2008

**Materials, Processes, and Characterization of Extended Air-gaps  
for the Intra-level Interconnection of Integrated Circuits**

Approved by:

Dr. Paul A. Kohl, Co-Advisor  
School of Chemical and Biomolecular  
Engineering  
*Georgia Institute of Technology*

Dr. Sue Ann Bidstrup Allen, Co-Advisor  
School of Chemical and Biomolecular  
Engineering  
*Georgia Institute of Technology*

Dr. Dennis W. Hess  
School of Chemical and Biomolecular  
Engineering  
*Georgia Institute of Technology*

Dr. J. Carson Meredith  
School of Chemical and Biomolecular  
Engineering  
*Georgia Institute of Technology*

Dr. W. Brent Carter (MSE)  
Materials Science & Engineering  
*Georgia Institute of Technology*

Dr. A. Bruno Frazier (ECE)  
School of Electrical and Computer  
Engineering  
*Georgia Institute of Technology*

Date Approved: November 19, 2007

## ACKNOWLEDGEMENTS

I was able to succeed in Ph.D at GeorgiaTech through the warm and grateful help and support from a number of people. First of all, my thesis advisors, Dr. Paul A. Kohl and Dr. Sue Ann Bidstrup Allen guided me during this project and showed me the deep and wide scientific knowledge. They trained me to find the proper approach to solve a problem and gave me an opportunity to expand my knowledge far beyond chemical engineering.

When I started my research project, Dr. Hollie A Reed helped me for working in the cleanroom and gave me the general knowledge of the project. Thus, I really appreciate her help. Also I want to acknowledge the entire research group members. In particular, Harley Hayden was not only a good friend, but also a great teacher for writing. I was really happy to meet Dr. William Mustain and Shruti Prakash. Osborn N. Tylor, who shared the office, gave me a great opportunity to discuss our project and it was fruitful.

I want to thank all the cleanroom staff for their great assistances. Especially, I really appreciate Dr. Raghunath Murali and Devin Brown for their help and cooperation in electron-beam lithography work.

I was really happy to meet the Korean students in the school of Chemical and Biomolecular Engineering who gave me a warm affection and kind interests.

Finally, I would like to thank my entire family for their big endurance and constant support. My parents and my wife's parents have always been there for me and gave me the endless and unlimited love. But I want to give the biggest appreciation to my wife, Hyejeong Lee. She has always been there for supporting and motivating me. In addition, my son, Soocheol Park and my sweet daughter, Soohyeon Park were always in my mind and gave me the peace and the happiness.

## TABLE OF CONTENTS

<b>ACKNOWLEDGEMENTS</b> .....	<b>iii</b>
<b>LIST OF TABLES</b> .....	<b>viii</b>
<b>LIST OF FIGURES</b> .....	<b>ix</b>
<b>NOMENCALTURE</b> .....	<b>xiii</b>
<b>SUMMARY</b> .....	<b>xv</b>
<b>CHAPTER 1: INTRODUCTION</b> .....	<b>1</b>
1.1 Back-end-of-the-line (BEOL) interconnects in integrated circuits.....	1
1.2 Air-gaps and extended air-gaps as an ultra low-k intra-metal dielectric materials .....	11
1.3 Thermally decomposable sacrificial polymers .....	14
1.4 Objectives of the research .....	18
<b>CHAPTER 2: AIR-GAP LITERATURE REVIEW</b> .....	<b>20</b>
<b>CHAPTER 3: EXPERIMENTAL TECHNIQUES, MATERIALS, AND EQUIPMENTS</b> .....	<b>31</b>
3.1 Thermally decomposable sacrificial polymers .....	31
3.2 Analysis methods and procedures .....	31
3.2.1 Thermo-gravimetric analysis (TGA) .....	32
3.2.2 Nanoindentation .....	32
3.2.3 Fourier Transform – Infrared Spectroscopy (FT-IR) .....	33
3.2.4 X-ray photoelectron spectroscopy (XPS) .....	33
3.2.5 Secondary Ion Mass Spectroscopy (SIMS) .....	34
3.2.6 Contact angle measurement .....	34
3.2.7 Profilometer .....	35
3.2.8 Mass spectroscopy (GC-MS) .....	35
3.2.9 Capacitance measurement of the comb testing structures .....	36

<b>CHAPTER 4: ELECTRON-BEAM HARDENING OF NORBORNENE-BASED SACRIFICIAL POLYMERS .....</b>	<b>37</b>
4.1 Background of electron-beam hardening of polymer thin films .....	37
4.2 Experiments .....	41
4.3 Results .....	44
4.3.1 The effect of electron energy on the properties of polymer thin films .....	44
4.3.2 The effect of electron dose on the properties of polymer thin films....	53
4.3.3 The structure change due to electron beam irradiation .....	53
4.3.4 The aging effect.....	58
4.3.5 The effect of operating gas on the properties of polymer thin films...	60
4.3.6 The effect of temperature on the properties of polymer thin films.....	64
4.4 Conclusion.....	66
<b>CHAPTER 5: IMPROVEMENT IN THERMALLY DECOMPOSABLE TEMPLATE MATERIAL FOR IC AIR-GAP STRUCTURES .....</b>	<b>69</b>
5.1 Background .....	69
5.2 Experiments.....	73
5.2.1 Preparation of thin films and decomposition residues of sacrificial polymers .....	73
5.2.2 Nanoindentation .....	74
5.2.3 Fabrication of sacrificial polymer lines and image processing .....	75
5.2.4 Thermo-gravimetric analysis .....	78
5.2.5 X-ray photoelectron spectroscopy analysis .....	79
5.2.6 Contact angle measurement .....	80
5.3 Results .....	80
5.3.1 The qualitative comparison of hardness by the nanoindentation .....	80
5.3.2 The effect of hardness on the process reliability of the sacrificial polymers .....	84
5.3.3 Thermal properties of sacrificial polymer thin films .....	89
5.3.4 Characterization of decomposition residues of sacrificial polymers ...	91
5.3.5 Hydrophobicity of the surface of thin films and decomposition residues .....	96
5.4 Conclusion .....	98

<b>CHAPTER 6: FABRICATION AND CHARACTERIZATION OF ULTRA LOW-K CU/AIR-GAP AND EXTENDED CU/AIR-GAP STRUCTURES USING HIGH MODULUS SACRIFICIAL POLYMER .....</b>	<b>99</b>
6.1 Background .....	99
6.2 Fabrication of the single layer Cu/air-gaps and extended Cu/air-gaps interconnect structures using the lift-off metallization technique .....	106
6.2.1 Fabrication of Cu/air-gaps interconnect structures .....	106
6.2.2 Fabrication of extended Cu/air-gaps interconnect structures .....	109
6.3 Experiments .....	111
6.3.1 Capacitance measurement of the comb structure devices .....	111
6.3.2 Moisture uptake of extended Cu/air-gaps interconnect structures .....	112
6.4 Electrostatic modeling .....	113
6.4.1 Modeling geometry .....	113
6.4.2 Effect of the integration of air-gaps and extended air-gaps on the interconnect capacitance .....	113
6.4.3 Effect of the dielectric constant of inter-level dielectric materials on the interconnect capacitance .....	116
6.4.4 Effect of the extended height of air-gaps and the space between metal lines on the interconnect capacitance .....	118
6.5 Results .....	120
6.5.1 Measured effective dielectric constants of Cu/air-gaps and extended Cu/air-gaps interconnect structures .....	120
6.5.2 Effect of moisture uptake of extended air-gaps/Cu interconnect structures on the effective dielectric constant .....	123
6.6 Discussion .....	128
6.6.1 Dual damascene Cu/air-gap process .....	128
6.6.2 Critical review of the different approaches for the integration of dual damascene air-gaps .....	131
6.6.3 Dual Damascene extended Cu/air-gap process .....	137
6.7 Conclusion .....	139
<b>CHAPTER 7: CONCLUSION.....</b>	<b>141</b>
7.1 Conclusion of the dissertation.....	141
7.2 Future work.....	146
<b>REFERENCES .....</b>	<b>148</b>

## LIST OF TABLES

Table 1.1.1 Commercialized low-k materials .....	10
Table 4.3.1 The most probable peak identifications for the gas byproducts of BuPNB-TESPMB .....	52
Table 4.3.2 The area ratio of major FTIR spectra peaks to CH stretching peak .....	59
Table 5.3.1 The nanoindentation results for thin films of TD-based and NB-based sacrificial polymers .....	84
Table 5.3.2 The summary of SEM image processing for the evaluation of the linearity of TD-based and NB-based sacrificial polymer lines .....	89
Table 5.3.3 The atomic composition of thin films and decomposition residues of TD-based sacrificial polymer .....	96
Table 5.3.4 The summary of the contact angle measurements of the polymer films itself and decomposition residues of TD-based and NB-based sacrificial polymers with the variation of the purging gases and the initial thickness of polymer thin films .....	97
Table 6.1.1 The summary of the different approaches for the integration of air-gaps in terms of the number of lithography and additional process steps compared to the conventional dual damascene process .....	102
Table 6.2.1 The temperature profile for the decomposition of sacrificial polymer with 0.5 weight % /min .....	109
Table 6.4.1 The summary of the electric flux density, capacitance, and $k_{eff}$ of homogeneous Cu/SiO <sub>2</sub> , Cu/air-gaps and extended Cu/air-gaps interconnect .....	115
Table 6.5.1 The summary of the measured effective dielectric constants of the comb structure devices .....	122



## LIST OF FIGURES

Figure 1.1.1 The cross section of a semiconductor device, showing the multi-layer interconnect structure .....	3
Figure 1.1.2 Schematic of the via-first dual damascene process .....	6
Figure 1.1.3 Frequency response of dielectric mechanisms .....	9
Figure 1.3.1 The chemical structures of monomer units of sacrificial polymers (a) norbornene (NB) (b) tetracyclododecene (TD) .....	15
Figure 1.3.2 The necessities of a harder sacrificial polymer in the dual damascene process flow .....	17
Figure 2.1.1 Cross-sectional scanning electron microscopy of Cu/air-gap structure fabricated via thermal decomposition of the norbornene-based sacrificial polymer [16] .....	23
Figure 2.1.2 The proposed decomposition mechanisms of the functionalized polynorbornene sacrificial polymer by Wedlake et. al. [24] .....	24
Figure 2.1.3 The pinch-off shape air-gaps formed by non-conformal deposition of the SiO <sub>2</sub> inter-layer dielectric material [29] .....	26
Figure 2.1.4 Cross-sectional secondary electron spectroscopy of Cu/air-gap structure fabricated by wet etching of the SiO <sub>2</sub> intra-metal dielectric material [19] ....	30
Figure 4.2.1 The chemical structures of the norbornene monomer units (a) butyl norbornene (b) triethoxy silyl norbornene .....	42
Figure 4.3.1 Electron energy distribution vs. depth for (a) 1keV (b) 5keV (c) 10keV e-beam acceleration .....	45

Figure 4.3.2 Dynamic TGA of polymer films e-beam irradiated at 2000 $\mu\text{C}/\text{cm}^2$ dose: (a) control sample (b) 1keV, 100°C (c) 5keV, 100°C (d) 10keV, 100°C .....	46
Figure 4.3.3 Nanoindentation for polymers e-beam irradiated at 2000 $\mu\text{C}/\text{cm}^2$ dose (a) control sample (b) 1 keV, 100°C (c) 5 keV, 100°C (d) 10 keV, 100°C .....	48
Figure 4.3.4 Pyrolyzer-MS spectra at 350°C a) control sample, b) 1 keV, 2000 $\mu\text{C}/\text{cm}^2$ , 100°C, c) 5 keV, 2000 $\mu\text{C}/\text{cm}^2$ , 100°C, d) 10 keV, 2000 $\mu\text{C}/\text{cm}^2$ , 100°C .....	50
Figure 4.3.5 Pyrolyzer-MS spectra at 400°C a) control sample, b) 1 keV, 2000 $\mu\text{C}/\text{cm}^2$ , 100°C, c) 5 keV, 2000 $\mu\text{C}/\text{cm}^2$ , 100°C, d) 10 keV, 2000 $\mu\text{C}/\text{cm}^2$ , 100°C .....	51
Figure 4.3.6 Dynamic TGA of polymer films irradiated at 5 keV energy: (a) control sample, (b) 500 $\mu\text{C}/\text{cm}^2$ , 50°C, (c) 1000 $\mu\text{C}/\text{cm}^2$ , 50°C, and (d) 2000 $\mu\text{C}/\text{cm}^2$ , 50°C .....	54
Figure 4.3.7 Nanoindentation of polymer films irradiated at 5 keV electron energy: (a) control sample, (b) 500 $\mu\text{C}/\text{cm}^2$ , 50°C, (c) 1000 $\mu\text{C}/\text{cm}^2$ , 50°C, and (d) 2000 $\mu\text{C}/\text{cm}^2$ , 50°C .....	55
Figure 4.3.8 FTIR spectra for (a) control sample (b) 1 keV, 2000 $\mu\text{C}/\text{cm}^2$ , 50°C (c) 5 keV, 2000 $\mu\text{C}/\text{cm}^2$ , 100°C and (d) 10 keV, 2000 $\mu\text{C}/\text{cm}^2$ , 100°C .....	57
Figure 4.3.9 Dynamic TGA for a polymer exposed to 5 keV, 500 $\mu\text{C}/\text{cm}^2$ , 50°C: (a) immediately after exposure and (b) after 2 month of air storage .....	61
Figure 4.3.10 Dynamic TGA for polymer films e-beam exposed at 5 keV, 500 $\mu\text{C}/\text{cm}^2$ , 50°C, using different purging gas (a) control sample (b) nitrogen purged sample during exposing (c) 2% hydrogen balanced nitrogen purged sample during exposure .....	62
Figure 4.3.11 Nanoindentation of the polymer films exposed to 5 keV, 500 $\mu\text{C}/\text{cm}^2$ , 50°C e-beam using different purging gases: (a) control sample (b) nitrogen exposure (c) 2% hydrogen and 98% nitrogen .....	63

Figure 4.3.12 Dynamic TGA for the polymer e-beam exposed at 5 keV, 2000 $\mu\text{C}/\text{cm}^2$ , (a) control sample at 100°C (b) ambient temperature, and (c) heated to 300°C in the e-beam chamber after irradiation .....	65
Figure 4.3.13 Nanoindentation of polymers exposed to 5 keV, 2000 $\mu\text{C}/\text{cm}^2$ : (a) control sample at 100°C, (b) ambient temperature, and (c) heated to 300°C prior to air exposure .....	67
Figure 5.1.1 The schematic diagram of the fabrication process of the single layer Cu/air-gap interconnect structure .....	71
Figure 5.2.1 The fabrication processes of sacrificial polymer lines, 50nm in width and 85 nm in height .....	76
Figure 5.3.1 The load-displacement curves of thin films of TD-based and NB-based sacrificial polymers using a nanoindenter .....	82
Figure 5.3.2 A sample image to determine the ideal straight center lines and the calculated center lines reflecting the actual shapes of polymer lines, NB-based sacrificial polymer, RF power = 300W .....	85
Figure 5.3.3 Top view scanning electron microscopic images of the patterns of SiO <sub>2</sub> hard mask on top of hard-baked sacrificial polymer layers .....	87
Figure 5.3.4 Top view scanning electron microscopic images of the lines of TD-based and NB-based sacrificial polymers, RF power = 400 W .....	88
Figure 5.3.5 Dynamic TGA of TD-based and NB-based sacrificial polymers .....	90
Figure 5.3.6 XPS Depth profiling of the decomposition residues of TD-based sacrificial polymer with different purging conditions during the thermal decomposition: (a) bare Al on Si-wafer, (b) purging condition A, (c) purging condition B, (d) purging condition C .....	92
Figure 5.3.7 TOF-SIMS carbon and SiC elemental mapping images of decomposition residues of TD-based sacrificial polymer: (a) purging condition A, (b) purging condition B, (c) purging condition C .....	95
Figure 6.1.1 The different integration approaches of dual damascene air-gaps ....	101

Figure 6.2.1 The fabrication processes flow for Cu/air-gaps interconnect structures using the Cu metallization first process .....	107
Figure 6.2.2 The fabrication processes flow for extended Cu/air-gaps interconnect structures using the Cu metallization first process .....	110
Figure 6.4.1 The electrostatic modeling geometry of the interconnect .....	114
Figure 6.4.2 The effect of dielectric constants of inter-layer dielectric materials on the percent reduction in capacitance and $k_{eff}$ (a) Percent reduction in capacitance, (b) Effective dielectric constant .....	117
Figure 6.4.3 The effect of the space between metal lines and extended height of air-gaps on the percent reduction in capacitance and $k_{eff}$ (a) Percent reduction in capacitance, (b) Effective dielectric constant .....	119
Figure 6.5.1 The cross sectional secondary electron microscopic image of extended Cu/air-gaps structure .....	121
Figure 6.5.2 The cross sectional secondary electron microscopic image of multi-layer air-gaps and Cu patterns .....	124
Figure 6.5.3 The effect of moisture uptake of extended Cu/air-gaps interconnect structures on the $k_{eff}$ .....	126
Figure 6.5.4 The effect of HMDS vapor treatment on the $k_{eff}$ of extended Cu/air-gaps interconnect structures .....	127
Figure 6.6.1 The proposed fabrication processes flow for Cu/air-gaps interconnect structure using dual damascene processes .....	129
Figure 6.6.2 The process flow of an embedded via-first dual damascene air-gap using a spin-on thermal degradable sacrificial polymer [10] .....	132
Figure 6.6.3 The challenges in the air-gap formation during non-conformal deposition of the inter-layer dielectric (a) Breakthrough of air-gaps, (b) Un-landed via due to misalignment .....	135
Figure 6.6.4 The proposed fabrication process flow for extended Cu/air-gaps interconnect structure using dual damascene processes .....	138

## NOMENCLATURE

$\varepsilon_0$  – the permittivity of the free space

$\boldsymbol{\varepsilon}_r$ ,  $\boldsymbol{K}$  – the dielectric constant of an insulator

$\chi$  – the electric susceptibility of a dielectric material

$A$  – Electrode area

$A(h_c)$  – Indentation contact area

$C$  – Capacitance

$C_{L-L}$  –Capacitance between the interconnect metal lines

$C_{total}$  – Total capacitance of a device

$d$  – Distance between two electrode

$D$  – Electric flux density

$E$  – Electric field

$F$  – Clock frequency

$h$  – Indenter displacement

$h_c$  – Contact depth

$h_f$  –Final indentation depth

$h_{max}$  – Maximum indentation depth

$H$  – Hardness

$I$  – Current

$P$  – Electric polarization

$P_I$  – Indentation load

$P_{max}$  – Maximum load

$Q$  – Amount of charge that passed through the surface in the time  $t$

$R$  – Resistance

$S$  – Contact stiffness

$V$  – Voltage

$W$  – Energy stored in a capacitor

AM – Applied Materials Co.

BARC – Bottom anti-reflection coating

BEOL – the back-end-of-the lines

BD – Black Diamond

BOE – Buffered oxide etch

BuPNB – Butyl-polynorbornene  
CMP – Chemical mechanical polishing  
CVD – Chemical vapor deposition  
E-beam – Electron-beam  
EI – electron ionization  
FTIR – Fourier transform infrared spectrometer  
HMDS – Hexamethyldisilazane  
HF – hydro-fluoric acid  
ICs – Integrated circuits  
IMD – Intra-level dielectric or Inter-metal dielectric  
ILD – Inter-layer dielectric  
IITC – international interconnect technology conference  
IPA – Isopropyl alcohol  
ITRS – International Technology Roadmap for Semiconductors  
 $k_{eff}$  – effective dielectric constant  
Low-k – the low dielectric constant  
MS – Mass spectroscopy  
NB – Norbornene  
NMP – N-methyl-2-pyrrolidone  
PECVD – Plasma enhanced chemical vapor deposition  
PMMA – Polymethyl-metacrylate  
PR – Photoresist  
RC – Resistance-Capacitance  
RF – Radio frequency  
RH – Relative humidity  
RIE – Reactive ion etching  
SEM – Scanning electron microscopy  
SIMS – Secondary ion mass spectroscopy  
TD – Tetracyclododecene  
TES – Triethoxy silane  
TESPNB – Triethoxy silyl-polynorbornene  
TGA – Thermal gravimetric analysis  
TOF-SIMS – Time-of-flight secondary ion mass spectroscopy  
XPS – X-ray photoelectron spectroscopy

## SUMMARY

Air-gap as an ultra low-k dielectric is an ultimate limit for the intra-metal dielectric material of the advanced interconnects in integrated circuits due to its low dielectric constant close to 1.0. Different integration approaches of the air-gaps have been developed and the integration technique of the air-gaps using a thermally decomposable sacrificial polymer provides a good control over the air-gap geometry and the full air-gap incorporation in the intra-metal dielectric region without the deposition of a dielectric at the side wall of metal lines. In terms of process reliability, it is required to improve the hardness of the sacrificial polymer and demonstrate an integration of air-gaps using the hard sacrificial polymer. In addition, to further improve the interconnect performance, the reduction of fringing field effect may be an issue for 22 nm node and beyond. The research presented here has three main objectives: (1) the improvement of hardness of a conventional sacrificial polymer; (2) the investigation and characterization of the new hard sacrificial polymer; and (3) the demonstration and characterization of air-gap integration and extension of air-gap into the inter-layer dielectric regions via thermal decomposition of the hard sacrificial polymer.

Chapter 1 communicates the need for air-gaps technology in the advanced integrated circuits and the objectives of the research in detail. Chapter 2 summarizes the current state of air-gap integration technology.

The specific details of the research begin in Chapter 3 with a general description of the experimental techniques and equipments. Also included in Chapter 3 is a brief description of the thermally decomposable sacrificial polymers.

In order to improve the hardness of a conventional norbornene-based sacrificial polymer, in Chapter 4, the effects of electron-beam exposure on the mechanical and thermal properties of the sacrificial polymers were investigated. Also, the structural changes of the irradiated sacrificial polymer depending on the electron energy and dose were discussed and related to the mechanical and thermal properties.

In Chapter 5, the mechanical and thermal properties of tetracyclododecene-based sacrificial polymer as a hard polymer were characterized and compared to the conventional norbornene-based sacrificial polymer. In addition, the effect of the difference in hardness on the process reliability was evaluated by qualitatively comparing the polymer lines of 50 nm in width and quantitatively evaluating the secondary electron microscopic images of those polymer lines.



The focal point of Chapter 6 is the fabrication and characterization of Cu/air-gap and Cu/extended air-gap interconnect structures using the harder tetracyclododecene-based sacrificial polymer. The advantages of air-gap and extended air-gap integration in the interconnect performance were discussed via 2-D electrostatic modeling and demonstrated by measuring the effective dielectric constant. The moisture uptake of extended Cu/air-gap interconnect structure was evaluated and the removal of adsorbed moisture was also discussed. In Chapter 6.6, the dual damascene integration schemes of air-gaps and extended air-gaps via thermal decomposition of the sacrificial polymer were proposed, and the critical issues in the proposed processes were discussed and compared with other integration approaches.

## CHAPTER 1: INTRODUCTION

### 1.1 Back-end-of-line (BEOL) interconnects in integrated circuits

The performance of semiconductor devices has been advanced by a continuous decrease in the size of transistors and interconnects [1] for the last 5 decades. Since the first point-contact transistor was invented in 1947 at Bell Labs by John Bardeen and Walter Brattain, the minimum feature size of the transistors has continuously shrunk from 10  $\mu\text{m}$  in 1970 [3] to 0.025  $\mu\text{m}$  in 2007 [1], resulting in cheaper, faster and higher performance devices. Also, as the minimum feature size of the transistors decreased, the interconnects became multi-layered and complex, and decreased in size to increase the integrity of the devices. For instance, the 2006 updated version of the International Technology Roadmap for Semiconductors (ITRS) [1] predicted that in 2010, there would be twelve metal levels, the metal one wiring pitch would be 90 nm, and the total interconnect length for metal one and five intermediate levels would be 2222 m/cm<sup>2</sup>. As a result, the continuous shrinkage of the minimum feature size of the integrated circuits caused many challenges for interconnects, and the device performances are dominated by the performance of the interconnects.

In microelectronics, interconnects serve as the link between the chip and other devices which allows each to function as intended. Therefore, interconnects include not only packaging but the entire infrastructure which bridges the gap between the semiconductor chips and their ultimate applications [4]. In a semiconductor chip, interconnects refer to the back-end-of-the-line (BEOL) which connect the transistors to power and signal sources outside of the chip. Interconnects in integrated circuits (ICs) are composed of multi-level metal lines for the transfer of both the signal and electrical power and dielectric materials to insulate the adjacent metal lines as shown in Figure 1.1.1. Therefore, the performance of the interconnects is determined by the properties of the metal, the dielectric materials and the geometry. The material properties related to the interconnect performance are the resistivity of the metal and dielectric constant of insulators, while geometry is determined by design rules. These properties affect interconnect performance through resistance-capacitance (RC) delay, cross talk, and power dissipation [1].

Multiplication of the resistance ( $R=V/I$  (Voltage·sec/Coulomb)) with the capacitance ( $Q/V$  (Coulomb/Voltage)) of the interconnects results in the dimension of time, which is the time delay caused by the interconnect structures. Scaling down the minimum feature size improves the gate delay; while interconnect RC

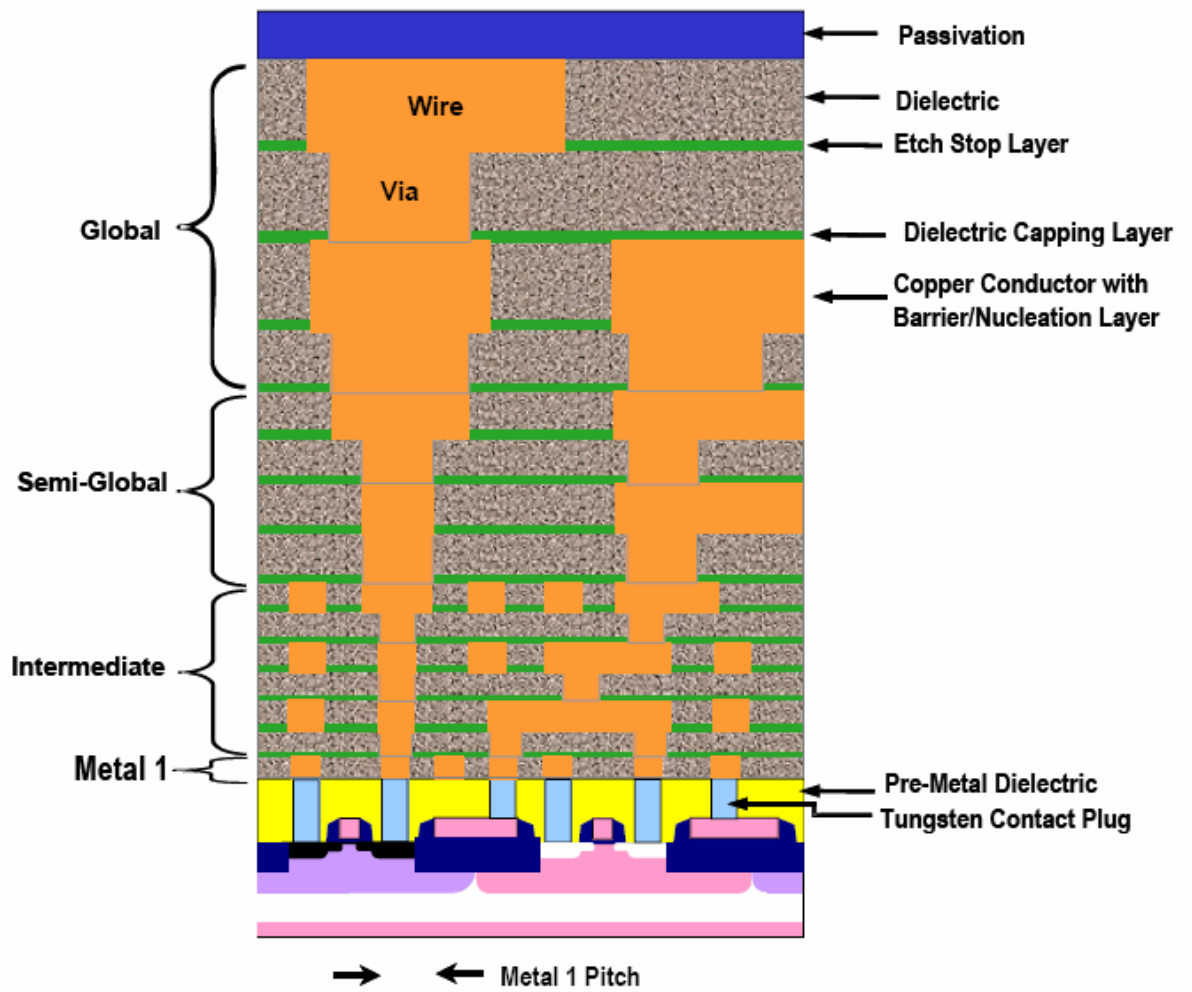


Figure 1.1.1 The cross section of a semiconductor device, showing the multi-layer interconnect structure [2]

delay degrades with feature size reduction [5]. Therefore, in order to continuously improve the device performance by scaling down, the low resistance metal lines and the reduction of the interconnect capacitance are required. The cross talk noise can be evaluated by the ratio of capacitance between interconnect metal lines ( $C_{L-L}$ ) to total capacitance of a device ( $C_{total}$ ) [6]. Thus, low interconnect capacitance is again required. Power dissipation of interconnects is approximated by the well-known expression [7];

$$\mathbf{Power} \propto \mathbf{C} \times \mathbf{V}^2 \times \mathbf{f} \quad (1.1)$$

where,  $C$  is the interconnect capacitance,  $V$  is the supply voltage, and  $f$  is the clock frequency. In a device, the supply voltage and clock frequency are fixed and thus, in order to reduce the power dissipation due to the interconnects, the interconnect capacitance must decrease. Overall, the interconnect challenges are intimately related to the resistivity of metal lines and the interconnect capacitance.

In order to decrease line resistance, the dual damascene Cu metallization processes were developed by IBM in 1997 to replace Al [8]. Cu has the advantages of lower resistance, higher allowable current density, better electromigration resistance, and increased scalability [8-10]. In order to address the difficulty in etching Cu patterns and the need to prevent Cu diffusion through the dielectric materials through the use of a metal barrier layer, the dual damascene process was

developed and is composed of dielectric patterning, deposition of a metal barrier and a Cu seed layer, the superfill process of Cu by electroplating, and the removal of extra Cu. Figure 1.1.2 shows the conventional via-first dual damascene process. There are two lithography steps for via and trench. In order to take advantage of low-k materials no etch stop layers are preferred.

In terms of lowering the interconnect capacitance, low-k materials should be incorporated in interconnect structures, because the interconnect capacitance is proportional to the dielectric constant ( $\kappa$ ) of the insulator or dielectric material as shown in Equation (1.2).

$$C = \epsilon_0 \cdot \kappa \cdot \frac{A}{d} \quad (1.2)$$

where C is the ideal parallel plate capacitance ( $F = \frac{\text{Coulomb}}{\text{Voltage}}$  )

$\epsilon_0 = \frac{1}{C^2 \mu_0} \approx 8.8541878176 \times 10^{-12} \frac{F}{m}$  (or  $\frac{C^2}{Nm^2}$ ) is the permittivity of the free space,

$\kappa$  is a dielectric constant of the insulator,

A is the electrode area ( $m^2$ ),

d is the distance between two electrodes (m).

The dielectric constant of an insulator, however, is related to electric polarization.

The electric polarization is the tendency of a material to allow an externally applied electric field to induce an electric dipole (separated positive and negative charges) in a material. Low-k materials are insulators that exhibit weak electric polarization

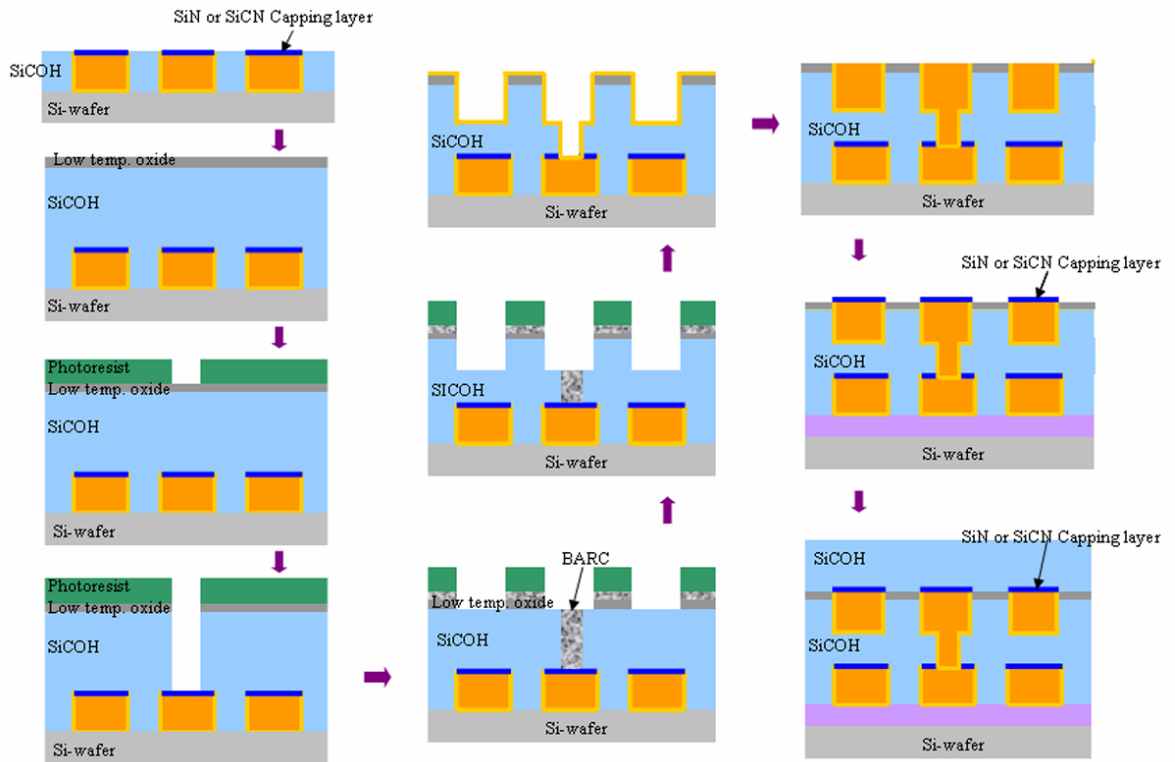


Figure 1.1.2 Schematic of the via-first dual damascene process

when subjected to an externally applied electric field. The electric polarization  $P$  is related to the electric field  $E$  and electric flux density (or electric displacement field)

$D$  by

$$\mathbf{D} = \epsilon_0 \mathbf{E} + \mathbf{P} \quad (1.3)$$

Also, the electric polarization  $P$  has a relationship with the electric field  $E$  through the electric susceptibility of a dielectric material  $\chi$  by

$$\mathbf{P} = \epsilon_0 \chi \mathbf{E} \quad (1.4)$$

Therefore, the electric flux density  $D$  is

$$\mathbf{D} = \epsilon_0 \mathbf{E} + \epsilon_0 \chi \mathbf{E} = \epsilon_0 (1 + \chi) \mathbf{E} = \epsilon_0 \kappa \mathbf{E} \quad (1.5)$$

and the dielectric constant of an insulator is related to the electric polarization by

$$\kappa = 1 + \chi = 1 + \frac{P}{\epsilon_0 E} \quad (1.6)$$

As a result, from Equation (1.6), the low dielectric constant of a material comes from low electric polarization. For instance, in a perfect vacuum, there is no electric polarization due to no atoms or molecules being present, indicating  $\chi = 0$  and  $k = 1$ .

In a solid state material, there are three polarization mechanisms: electronic polarization; atomic or ionic polarization; and dipolar or orientational polarization.

The electronic polarization occurs in neutral atoms such as hydrogen atoms, when an electric field displaces the nucleus with respect to the electrons that surround it.

Atomic or ionic polarization occurs when adjacent positive and negative ions stretch



under an applied electric field and NaCl or ZnO are examples of materials exhibiting ionic polarization. Dipolar or orientational polarization occurs when permanent dipoles in asymmetric molecules such as H<sub>2</sub>O respond to an applied electric field. Each polarization mechanism has an associated response time and thus will not contribute to the dielectric constant  $k$  beyond some corresponding frequency [11]. At the frequency range of interest to us, all three polarization mechanisms contribute to the polarization as shown in Figure 1.1.3 [12], but the relative contributions of the three polarization mechanisms may be different from material to material.

Numerous low dielectric constant (low- $k$ ) materials have been developed and processed including; fluorine doped silicon dioxide (F-SiO<sub>2</sub>), polymers, spin-on-glasses, foams [13], plasma enhanced chemical vapor deposition (PECVD) SiOC [14], PECVD SiCOH [15], porous materials [14,15] and air-gaps [16-21]. In Table 1.1.1, the commercialized low- $k$  materials are summarized. Air is composed of 78.09% nitrogen ( $k=1.00058$ ), 20.95% oxygen ( $k=1.000494$ ), 0.93% argon ( $k=1.000513$ ), and 0.03% CO<sub>2</sub> ( $k=1.6$ ) and those have weak electric polarization. Therefore, the dielectric constant of air is very low, close to 1.0. However, the moisture in the air has a larger dielectric constant of more than 80 and degrades the effective dielectric constant of air-gaps as an intra-metal dielectric material. Therefore, moisture should be excluded from pores and air-cavities in the

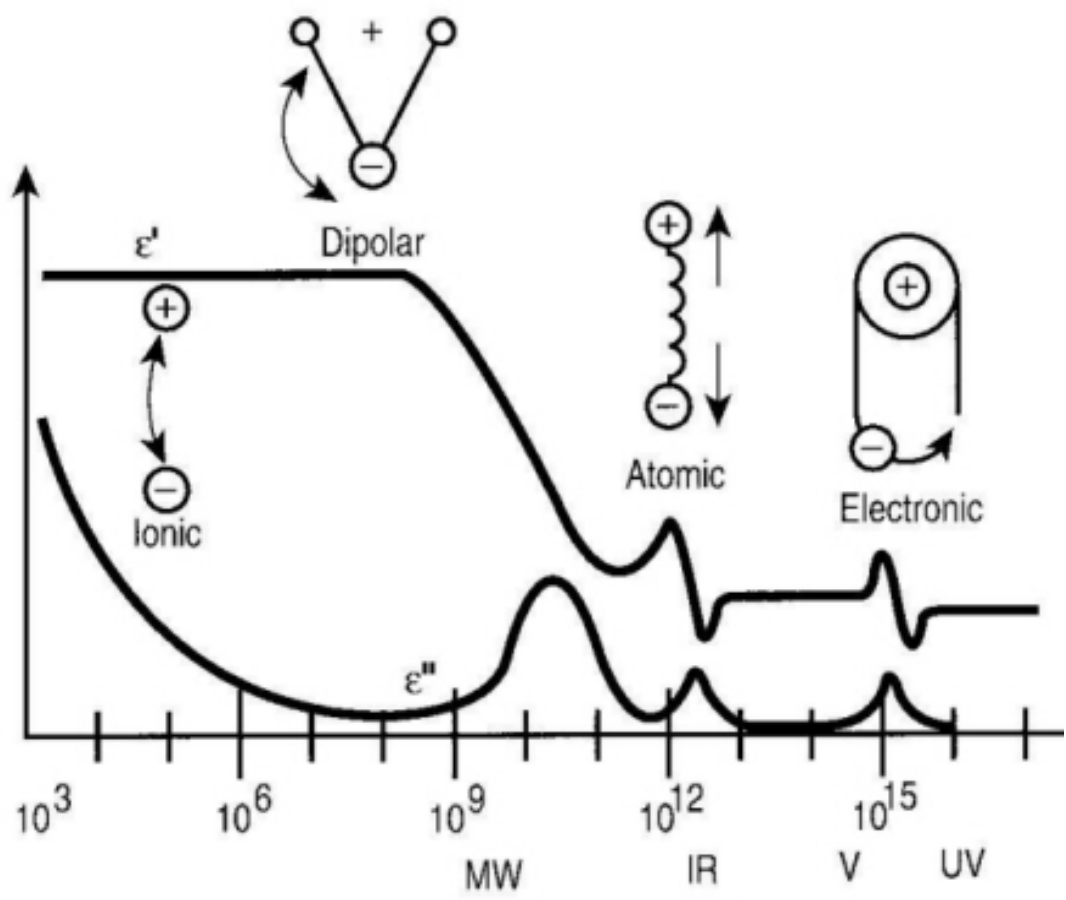


Figure 1.1.3 Frequency response of dielectric mechanisms [12]

Table 1.1.1 Commercialized low-k materials

Materials	K= 4.1	K= 3.5	K=2.6-3.2	K=2.0-2.5	Process	Company
Organic			SiLK Flare		Spin-on Spin-on	Dow Chem. Honeywell
Hybrid			BD I <sup>1</sup> CORAL Flowfill	BD II <sup>1</sup> POLA Orion	CVD CVD CVD	AM <sup>2</sup> Novellus Trikon
			HOSP  HSGRZ26 OCD	Nanoglass-E ALCAP-S HSG 6210 OCL Zircom	Spin-on Spin-on Spin-on Spin-on Spin-on	Honeywell Asahi Chem. Hitachi Chem Tokyo Ohka Shibley
Inorganic	SiO <sub>2</sub>	F-SiO <sub>2</sub>	Fox	XLK	CVD Spin-on	Dow Corning

BD<sup>1</sup> = Blackdiamond, AM<sup>2</sup> = Applied Materials,

interconnects. Due to a low dielectric constant close to 1.0, the incorporation of air, in the form of air-gaps, is an ultimate limit for the intra-metal dielectric material for advanced interconnects in integrated circuits.

## **1.2 Air-gaps and extended air-gaps as an ultra low-k intra-metal dielectric materials**

Air-gaps as an intra-metal dielectric material use air or gas as an insulator to electrically separate adjacent metal interconnect lines. After deposition of an inter-layer dielectric material or encapsulating material, sacrificial polymers in between Cu lines are removed by thermal decomposition and air-gaps are formed. During the thermal decomposition, the gaseous byproducts in a cavity between metal conductors will quickly come into equilibrium with the ambient atmosphere. If air is the ambient gas, it will exchange with the original gaseous byproducts in a cavity, forming air-gaps for the intra-metal dielectric. In the fabrication processes, the challenges at the process level are the high aspect ratio and anisotropic patterns of sacrificial polymers, and chemical mechanical polishing (CMP) process. In addition, the sacrificial polymer should be thermally stable in the plasma enhanced chemical vapor deposition (PECVD) process and leave no residues after decomposition. Therefore, the thermal and mechanical properties of the sacrificial polymers and

percent residue after decomposition are critical for the performance and reliability of Cu/air-gaps interconnect structures.

As mentioned previously, the interconnect challenges are intimately related to interconnect capacitance or the effective dielectric constant ( $k_{eff}$ ) of the interconnects, and as the minimum feature size of the semiconductor devices decreases, concerns about those challenges increase. Therefore, in order to attack these issues on interconnects, the interconnect capacitance or  $k_{eff}$  should be reduced and low-k materials should be incorporated in the interconnect structures.

The capacitance of a capacitor can be calculated by

$$\vec{D} = \epsilon_0 k \vec{E} \quad (1.7)$$

$$W = \frac{1}{2} (CV^2) = \int \vec{D} \cdot d\vec{E} \quad (1.8)$$

$$\Rightarrow C = 2 \cdot \frac{\int \vec{D} \cdot d\vec{E}}{V^2} = 2 \cdot \frac{\int \epsilon_0 k \vec{E} \cdot d\vec{E}}{V^2} \quad (1.9)$$

$$= 2\epsilon_0 k \frac{\int \vec{E} \cdot d\vec{E}}{V^2} \quad (1.10)$$

where  $\vec{D}$  is the electric flux density or electric displacement field ( $\frac{1}{m^2}$ ),

$\vec{E}$  is the electric field ( $\frac{N}{C}$ ),

$V$  is the applied voltage ( $V = \frac{Nm}{As} = \frac{kgm^2}{As^3}$ )

Equation (1.10) shows that with a given applied voltage and electric field, the capacitance can be reduced by using low dielectric constant materials. By incorporation of air as an intra-metal dielectric material in-between Cu metal lines,

the dielectric constant of the intra-metal dielectric region decreases from 4.0 (SiO<sub>2</sub>) to 1.0 (air) and the electric flux density decreases as well. As the half pitch of the interconnect decreases, the advantage of integration of the air-gaps as an intra-metal dielectric material on the interconnect capacitance and  $k_{eff}$  may increase, because the electric field strength increases and further concentrates on the intra-metal dielectric region.

On the other hand, a fringing electric field always exists at the corners of metal lines. As the gap between the metal lines decreases, the fringing electric field increases resulting in an increase in the interconnect capacitance and  $k_{eff}$ . Hence, in the future technology node beyond 22 nm, the increase in the interconnect capacitance due to of the high fringing electric field may be an issue. In order to alleviate the effect of the fringing electric field on the interconnect capacitance and  $k_{eff}$  and further reduce the interconnect capacitance, air-gaps can be extended into the top and bottom inter-layer dielectric region.

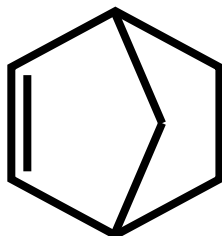
There are three different approaches to integrate air-gaps into an intra-metal dielectric region, which are compatible with the dual damascene process. The first approach is the use of thermally decomposable sacrificial polymers as place holders in between Cu metal lines [16-18]. The second approach is the wet etching of sacrificial materials in between the Cu metal lines [19] and the third is the use of a

non-conformal deposition of the inter-layer dielectric material [20,21]. The advantages and challenges of each approach will be discussed in Chapter 6. In this research, the integration of air-gaps in the intra-metal dielectric regions using thermal decomposition of sacrificial polymers as place holders was studied.

### **1.3 Thermally decomposable sacrificial polymers**

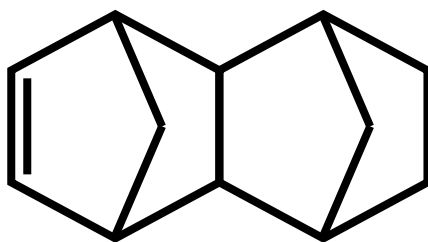
The requirements of a good thermally decomposable sacrificial polymer are:

1) a low amount of decomposition residue, 2) thermal stability during processing, 3) proper chemical resistance, 4) good adherence to the substrate and metal, 5) a hydrophobic surface of both the sacrificial polymer and decomposition residues, 6) good mechanical strength, 7) good process reliability. It is known that cyclic olefin copolymers have high glass transition temperatures, good optical clarity, low shrinkage, low moisture absorption, and low birefringence, because of the bulky cyclic olefin units that are either randomly or alternately attached to polymer backbone [9,10]. In this research, two cyclic olefin copolymers were investigated as thermally decomposable sacrificial polymers. Those were norbornene based (Unity4011<sup>TM</sup>, Promerus LLC) and tetracyclododecene based (Unity4131<sup>TM</sup>, Promerus LLC) sacrificial polymers, whose molecular structures are shown in Figure 1.3.1. The NB- based sacrificial polymer has good adhesion to substrates due



(a) The base structure of the norbornene polymer

(Unity4011<sup>TM</sup>, Promerus LLC.)



(b) The base structure of the tetracyclododecene polymer

(Unity4131<sup>TM</sup>, Promerus LLC)

Figure 1.3.1. The chemical structures of monomer units of sacrificial polymers

(a) norbornene (NB) (b) tetracyclododecene (TD)



to silane side-groups and a high glass-transition temperature of more than 350 °C [23]. In addition, the NB-based sacrificial polymer is thermally stable at 300 °C and remains residue less than 1 % [24]. Along with these properties, the NB-based thermally decomposable sacrificial polymer was considered as a low-k dielectric material due to its low dielectric constant of 2.4-2.6 [22], and has been used as a sacrificial placeholder to fabricate air-gaps in the intra-metal dielectric regions [16,25]. However, it has been known that the hardness of the templating sacrificial polymers is critical to the mechanical fidelity of the structure during processing. Figure 1.3.2 shows that, for trench formation of the sacrificial polymer in the dual damascene process flow, high aspect ratio and anisotropic etching of sacrificial polymers is required. The hardness of sacrificial polymers is also important during the CMP process. Thus, the effects of the exposure of thin films of NB-based sacrificial polymer to electron-beam on the hardness and thermal properties were investigated in Chapter 4. The TD-based sacrificial polymer, on the other hand, was expected to be harder than the NB-based sacrificial polymer due to a more rigid molecular structure. The hardness of the TD-based sacrificial polymer was compared with the NB-based sacrificial polymer in Chapter 5, and its' material properties were also investigated.



#### **1.4 Objectives of the research**

The first objective of this research was the investigation of the effects of electron-beam exposure on thermal and mechanical properties of sacrificial polymers. As mentioned previously, the hardness of sacrificial polymer is critical for better process reliability of the Cu/air-gap interconnect structure. Thus, in order to harden the conventional NB-based sacrificial polymer, it was exposed to the electron-beam with the variation of electron energy and dose. The effects of electron energy and dose on the thermal and mechanical properties were investigated using nanoindentation and thermal-gravimetric analysis. In addition, how structural changes of the irradiated sacrificial polymer affect the thermal and mechanical properties was investigated.

The second objective was the identification and characterization of a harder sacrificial polymer for the better process reliability. TD-based sacrificial polymer which shows the more rigid molecular structure than NB-based sacrificial polymer was studied in terms of hardness, thermal properties. In addition, the effect of the hardness of the sacrificial polymer on the process repeatability was qualitatively and quantitatively evaluated.

The third objective was the simulation and demonstration of the improvement of the interconnect performance using air-gaps and extended air-gaps

as the intra-metal dielectric materials by electrostatic modeling and fabrication of test devices. Moisture uptake of extended Cu/air-gaps interconnects was studied as well in terms of integration reliability. A critical review of the different approaches of dual damascene air-gaps fabrication processes was performed in order to compare and evaluate the critical challenges in each approach.

As a result, this research project was performed in order to address challenges related to interconnects of integrated circuits and contribute to the development of advanced interconnects and semiconductor devices through the fabrication and characterization of air-gaps and extended air-gaps using thermally decomposable sacrificial polymers.

## CHAPTER 2. AIR-GAP LITERATURE REVIEW

The concept of air-gap integration as an intra-metal dielectric material was first introduced by R.H. Havemann et al. (Texas Instrument Inc.), in 1995 [26]. In their approach, disposable solid materials (e.g. photoresist) between Al metal lines were removed by wet etching or ashing through the porous materials, resulting in the formation of air-gaps between the Al metal lines. In this process, Al metal lines were first formed by etching and then the air-gaps in between the Al metal lines were formed one layer at a time. However, in case of Cu metal lines for advanced interconnect structures, it is difficult to make high aspect ratio (more than 2.0) Cu lines by etching; hence, dual damascene Cu metallization processes were developed in 1997 [8]. In the dual damascene Cu metallization process, trench patterns of an intra-metal dielectric layer are formed before Cu metallization as shown in Figure 1.1.2. Therefore, this approach (the metallization first process) is not applicable to multi-layer Cu interconnect structures.

M.B. Anand et al. proposed a gas-dielectric interconnect process which was called NURA [27,28]. In the proposed process flow, a carbon layer deposited by sputtering was used as a temporary place holder between metal lines. On the carbon trench patterns, metal was deposited and etched back. After the deposition of a thin

SiO<sub>2</sub> bridge layer on top of the carbon and metal trench patterns, the carbon between metal lines was removed by furnace ashing in an oxygen ambient at about 400~450 °C. Oxygen diffused through the thin bridge layer and reacted with carbon to form carbon dioxide, leaving the space between metal lines filled with gas. Anand et. al. [27,28] thoroughly investigated properties of the thin SiO<sub>2</sub> bridge layer because of engineering issues such as deformation of the layer during the furnace ashing step of the carbon, and dielectric constant of the bridge layer. The effect of the poor heat conduction capability of the gas on the temperature rise of the interconnect was studied as well by finite element simulation. The simulation results showed that the interconnect temperature during the operation of a device could increase by only a few degrees because most of the resistance heat was conducted through the good metal conductors. Those simulation results were supported by an additional study by Shieh et al. [29]. In the Anand's studies, the presence of residues and their effect on interconnect performance was not discussed. In addition, multi-layer interconnect fabrication procedures were not explained.

Kohl et al. also reported the use of sacrificial materials as place holders between Cu metal lines in 1998 [16, 30]. In their process, a thermally decomposable functionalized polynorbornene was used as the place holder and a thick PECVD SiO<sub>2</sub> layer was deposited to serve as an encapsulating layer and a diffusion pathway

of decomposition gaseous byproduct and air. They followed the dual damascene process flow and demonstrated a Cu/air-gap structure of 0.26  $\mu\text{m}$  in width, as shown in Figure 2.1.1. On the trench patterns of the sacrificial polymer as a temporary intra-metal dielectric material, the Cu lines were deposited by electroplating and a CMP step. After deposition of an inter-layer dielectric material, the sacrificial polymers in between the Cu lines were removed by thermal decomposition in a furnace with purging nitrogen gas, and air-gaps were formed. During the thermal decomposition, the ambient gases exchanged with the original gaseous byproducts in a cavity, forming air-gaps for the intra-metal dielectric. In another paper [24], thermal decomposition kinetics of the functionalized polynorbornene were studied, and a first-order reaction was proposed. The authors concluded that the degradation mechanism of the functionalized polynorbornene involved scission of the linkage joining the bicyclic repeat units as shown in Figure 2.1.2. The effect of decomposition rate and encapsulating materials on the deformation of air-gaps and air-channels was thoroughly studied by Xiaoqun et al. [31]. Adhesion and mechanical properties of the functionalized polynorbornene were investigated by Grove et al. [32], and it was shown that attaching a triethoxysilyl group and alkyl group to the polymer backbone substantially improved the adhesion and elongation-to-break value of the homopolymer.

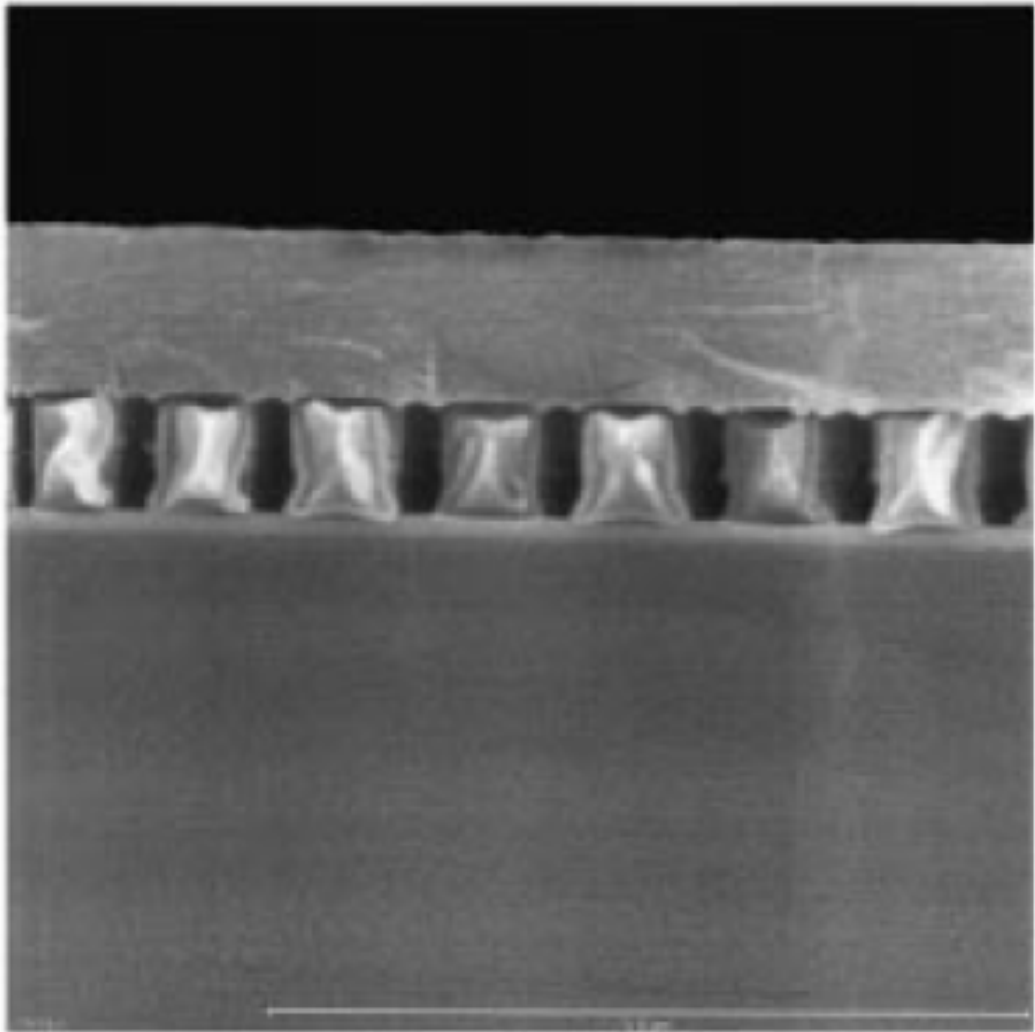
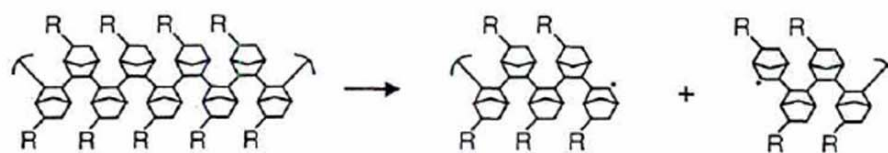


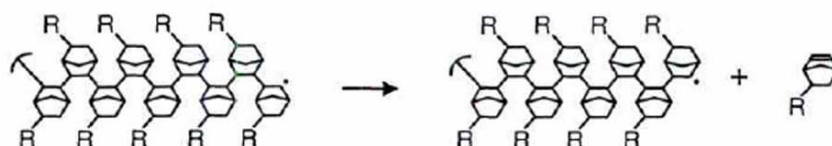
Figure 2.1.1 Cross-sectional scanning electron microscopy of Cu/air-gap structure fabricated via thermal decomposition of the norbornene-based sacrificial polymer [16].



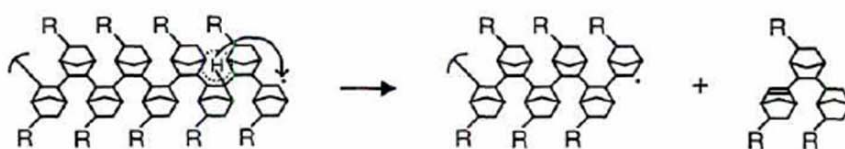
Initiation:



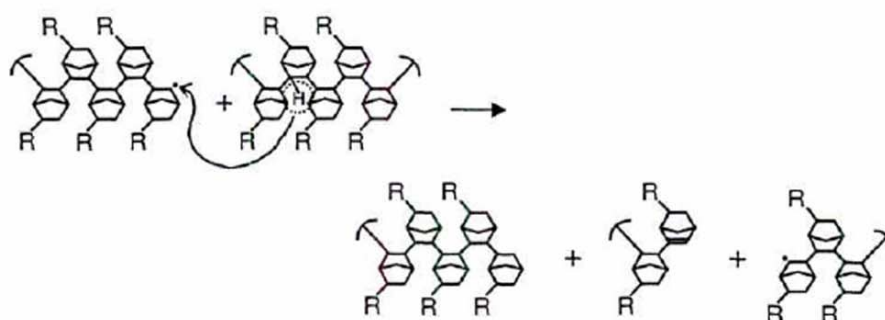
Depropagation:



Intramolecular Transfer:



Intermolecular Transfer:



Termination:

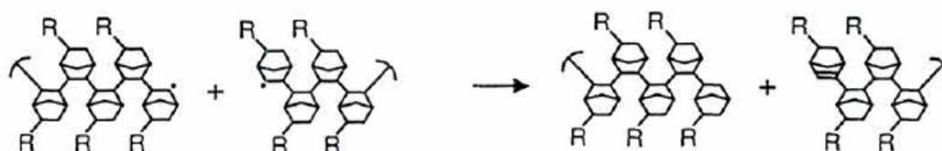


Figure 2.1.2 The proposed decomposition mechanisms of the functionalized polynorbornene sacrificial polymer by Wedlake et al. [24]

Gosset et al. have also studied the integration of air-gaps using thermally degradable polymers [34, 35]. A thermally degradable polymer from Dow Chemical Company was used for improved thermal stability during processing. A thin porous oxide-like hard mask layer above the thermal degradable polymer was used to improve the mechanical stability of the stack during CMP and thermal decomposition steps. Thus, a porous Black Diamond<sup>TM</sup> CVD layer instead of a spin-on hard mask was used. Two Cu metal layers with air-gaps fabricated by embedded via-first dual damascene processes were demonstrated [18].

Air-gap formation during non-conformal CVD deposition of an inter-layer dielectric material was first introduced by Saraswat and Havemann in 1998 [29,36]. In the 1998 International Interconnect Technology Conference (IITC) [29], they showed pinch-off shape air-gaps with deposition of SiO<sub>2</sub> inter-layer dielectric materials at the side wall of metal lines as shown in Figure 2.1.3. In addition, they discussed the process integration issues of thermal and electromigration reliability. They concluded that thermal performance and electromigration resistance of air-gap interconnect stacks were comparable to a homogeneous SiO<sub>2</sub> interconnect. However, process integration and reliability issues such as the opening of air-gaps during CMP and the via etch process, and misalignment of the via were realized [29,37]. In order to solve those issues, Ueda et al. [37] suggested self-aligned via plugs by SiO<sub>2</sub> etch

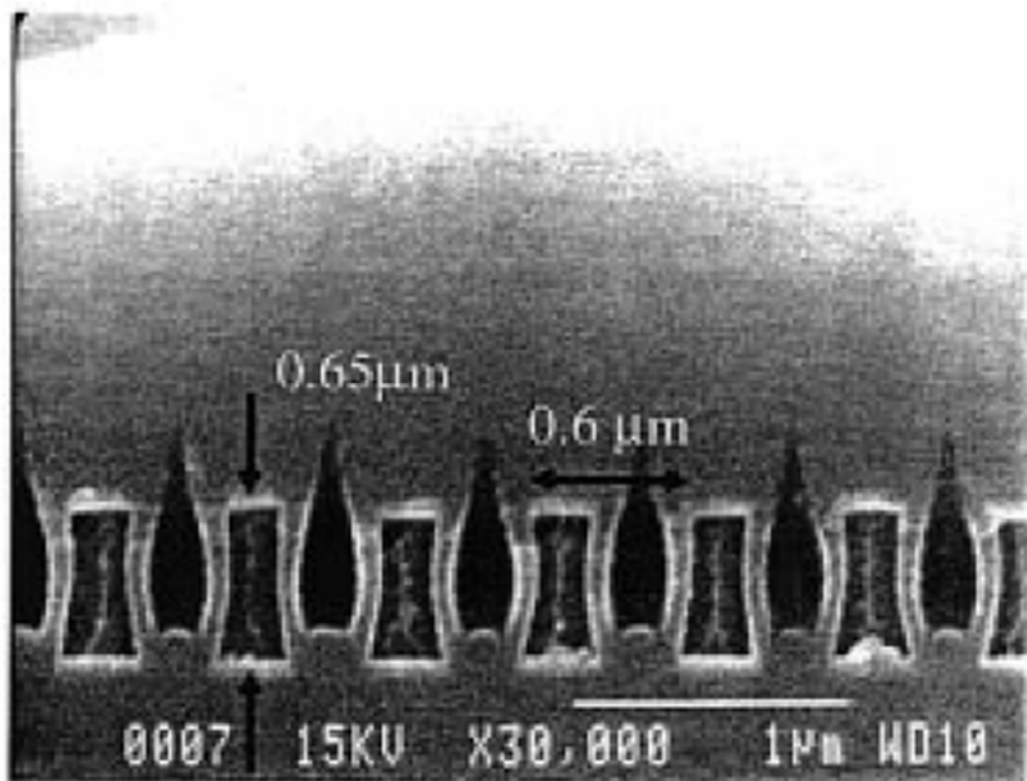


Figure 2.1.3 The pinch-off shape air-gaps formed by non-conformal deposition of the  $\text{SiO}_2$  inter-layer dielectric material [29].

back. He also demonstrated the measured  $k_{eff}$  of 1.8 at 0.3  $\mu\text{m}$  line spacing and a small leakage current less than  $1.0\text{E-}12$  (A). However, in their processes, the metal lines were an alloy of Al and Cu, and the trench patterns of Al-Cu metal were formed by etching, which is not applicable to forming Cu interconnect lines.

In order to take advantage of Cu metal as a better electrical conductor than Al, Arnal et al. demonstrated an etch back process of a  $\text{SiO}_2$  intra-metal dielectric material after the standard dual damascene process [38-40]. A silane-based and tetraethoxy silane (TEOS)-based  $\text{SiO}_2$  was used as an intra-metal dielectric and inter-layer dielectric material, and the deposition process was precisely tuned to control the geometry of air-gaps. After the standard dual damascene process,  $\text{SiO}_2$  intra-metal dielectric material in between Cu metal lines with narrow spaces were selectively etched back using an additional lithography and a hard mask to avoid penetration of the via into an air-gap. After the etch-back of the  $\text{SiO}_2$  intra-metal dielectric material, a CVD process of an upper  $\text{SiO}_2$  layer was controlled to avoid metal intrusion and opening of the air-gaps during upper level processing due to higher growth of air-gaps into a via layer. In order to further reduce the interconnect capacitance, PECVD SiOC instead of  $\text{SiO}_2$  was introduced in the fabrication of air-gaps by Gosset [41] and Harada [20]. In their approaches, the width of the trench patterns formed by etch-back of  $\text{SiO}_2$  or SiOC intra-metal dielectric materials in

between Cu lines was kept constant to control the shape and geometry of air-gaps. In 2007, IBM announced the first manufacturing-worthy dual damascene air-gap process [21]. Like Arnal's, Gosset's and Harada's processes, IBM demonstrated that after finishing the dual damascene metallization process, a SiCOH intra-metal dielectric material in between Cu lines were selectively etched-back in the desired dense interconnect region, and the upper SiCOH inter-layer dielectric was non-conformally deposited, forming pinch-off air-gaps.

On the other hand, other sacrificial materials well-known in terms of process integration and mechanical strength within multi-level stacks were also considered for the fabrication of air-gaps. Gueneau De Mussy et al. [42] introduced local air-gaps which were limited close to metal sidewalls by the local modification of SiC or SiCOH and etching by hydro-fluoric acid (HF). However, damage on the metal barrier layer due to exposure to HF and via-misalignment were identified as issues. In the 2003 IITC conference, Gosset et al. proposed hybrid air-gap and SiLK<sup>TM</sup> (Dow Chemical Co.) interconnect structures [19,34]. SiO<sub>2</sub> was used as an intra-metal dielectric material and SiLK<sup>TM</sup> was used as an inter-layer dielectric material. Diluted HF solution or buffered oxide etch (BOE) solution penetrated through the open area of the SiC capping layer and diffused into the interconnect structures, etching only SiO<sub>2</sub> intra-metal dielectric materials between Cu lines. Finally air-gaps

were formed as shown in Figure 2.1.4 and localized in the desired dense area by controlling etch rate and time. The effect of different etch solutions such as 1% HF, BOE and HF vapor on the lateral and vertical etch rate, and damage on metal lines was studied. Due to exposure to hydrofluoric acid chemistries and residual solution, corrosion of Cu metal lines and damage on Ta/TaN metal barrier layer were observed [43]. In the 2007 IITC, Gosset et al. showed the successful integration of two level air-gaps/Cu interconnect structures formed by wet etching of SiO<sub>2</sub> intra-metal dielectric materials [19]. The estimated effective dielectric constant was 1.8 ~ 1.9.

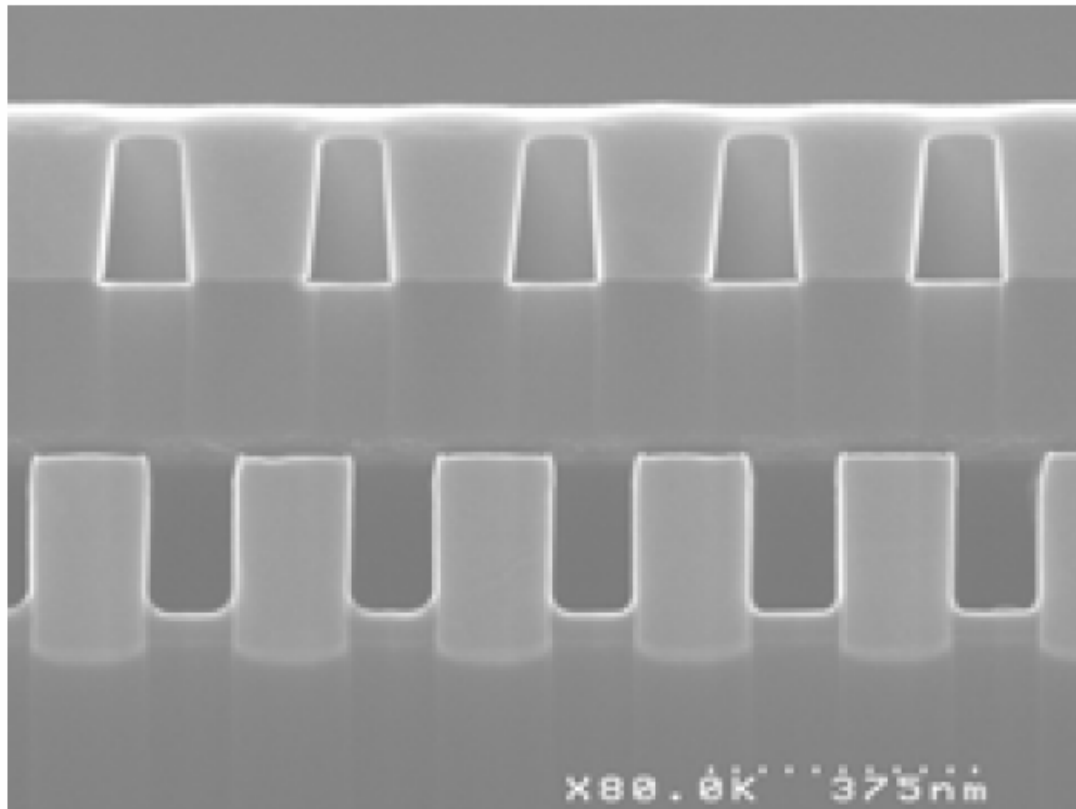


Figure 2.1.4 Cross-sectional secondary electron spectroscopy of Cu/air-gap structure fabricated by wet etching of the SiO<sub>2</sub> intra-metal dielectric material [19].

## **CHAPTER 3: EXPERIMENTAL TECHNIQUES, MATERIALS, AND EQUIPMENTS**

### **3.1 Thermally decomposable sacrificial polymers**

Two different sacrificial polymers were considered in this study, norbornene (NB)-based sacrificial polymer (Unity4011<sup>TM</sup>, Promerus LLC.) and tetracyclododecene (TD)-based sacrificial polymer (Unity4131<sup>TM</sup>, Promerus LLC), both provided by Promerus LLC. The concentrated polymer solutions were diluted to make the desired film thickness using mesitylene (1,3,5-trimethylbenzene) solvent. A spin speed curve of each diluted solution was developed.

The standard processes to make sacrificial polymer films were spin coating and soft-bake at 110 °C for 5 min on a hot-plate. After soft-baking, the polymer films were hard-baked at 300 °C for 1 hour in a furnace with purging nitrogen gas. During hard-baking, residual solvent and low-temperature volatile elements were removed.

### **3.2 Analysis methods and procedures**

The detailed experimental procedures are explained in the following chapters. Thus, the analytical instruments and techniques used in this study are summarized in this section.



### 3.2.1 Thermo-gravimetric analysis (TGA)

A Seiko Instruments Inc. 320 Thermogravimetric Differential Thermal Analyzer (Haake Instrument, Paramus, NJ) was used to investigate thermal properties of sacrificial polymers which included thermal stability, decomposition temperature and amount of residues. The sacrificial polymer films were scraped from the wafer surface and placed in a TGA sample pan. In the TGA experiment, before increasing the temperature, nitrogen gas was purged for 30 min to remove residual oxygen from the furnace and the film samples were heated at 2 °C/min from room temperature to 550 °C. The change in sample weight was recorded as a function of time and temperature.

### 3.2.2 Nanoindentation

The hardness of polymer thin films was measured using the TriboIndenter (Hysitron Inc. Minneapolis, MN) nanoindentation system. The indentation system was enclosed in an acoustic housing and located on an anti-vibration table. For indentation, the Z-axis resolution was 0.04 nm and a three sided Berkovich tip was used. The average radius of curvature for a Berkovich tip was typically between 100 nm and 200 nm. To exclude the substrate effect, the maximum force was chosen so as to indent less than 10 % of the film thickness [44]. For quantitative analysis, the

calculation procedures developed by Oliver and Pharr [42,53,58] were used to calculate the hardness.

### 3.2.3 Fourier Transform – Infrared Spectroscopy (FT-IR)

A Nicolet Magna IR 560 Fourier Transform Infrared Spectrometer (FTIR) was used in attenuated total reflectance (ATR) mode to investigate the structural changes of the polymer thin films after exposure to electron beam. The spectra were scanned from  $500\text{ cm}^{-1}$  to  $4500\text{ cm}^{-1}$  at  $4\text{ cm}^{-1}$  resolution.

### 3.2.4 X-ray photoelectron spectroscopy (XPS)

The thickness and composition of decomposition residues of TD-based sacrificial polymers were investigated using X-ray Photoelectron Spectroscopy (XPS) and depth profiling. XPS measurements were carried out with a Physical Electronics model 1600 XPS system using an aluminum *K $\alpha$*  source and toroidal monochromator. All analyses were setup with a 0.8 mm spot size and  $45^\circ$  take-off angle. The base pressure was less than  $5\text{E-}9$  Torr. 2 keV Ar-ion sputtering was used for depth profiling of the decomposition residue. Even though depth profiling does not give accurate absolute thickness, the rough thickness of the thin films can be estimated and compared with each other. The Ar-ion sputtering rate (2.9 nm/min)

was calibrated by depth profiling of a known thickness sacrificial polymer layer. A neutralizer was always turned on during measurement in order to compensate charging effect from polymer thin films and decomposition residues. Occasionally the spectra would be shifted due to the severe charging effect depending on sample. In that case, adventitious carbon at 284.4 eV was used to calibrate the peak positions [68]. The voltage and current of the neutralizer were 2.0 V and 20 mA, respectively.

### 3.2.5 Secondary Ion Mass Spectroscopy (SIMS)

The elemental mapping images of decomposition residues with different oxygen concentration in the decomposition furnace were taken using time-of-flight secondary ion mass spectroscopy (TOF-SIMS, CAMECA ION-TOF IV, AMETEK Inc. Materials Analysis Division, France) [69] and the mapping area was  $70\ \mu\text{m} \times 70\ \mu\text{m}$ . A Gallium ion gun with the ion energy of 1.5 keV was used.

### 3.2.6 Contact angle measurement

The hydrophobicity of the sacrificial polymer thin films and decomposition residues were evaluated by measuring the contact angle of a water drop on the surface of the samples using a VGA 2500XE (Video Contact Angle System, AST Product Inc., Billerica, MA). The measurements were repeated ten times for each

sample and the contact angles were averaged.

### 3.2.7 Profilometer

The thickness of sacrificial polymer thin films was measured using a KLA-Tencor P-15 profiler. The radius of the diamond stylus tip is 2 mm with 60° cone angle. Thin films of sacrificial polymers were scraped off a silicon wafer using a blade, and the height difference between the surface of the thin films and the bottom in the scratched area was measured. During the measurements, the samples were held in place by vacuum.

### 3.2.8 Mass spectroscopy (GC-MS)

A VG 70SE pyrolyzer-mass spectroscope (MS) with electron ionization (EI) was used to investigate the effect of exposure of sacrificial polymer thin films to electron beam on the structural variation of polymer thin films. The data were collected from 30 Da to 700 Da as a function of temperature. Hard-baked thin films of sacrificial polymers were scraped off a silicon wafer, collected and used for evaluating evaporated elements at each temperature during the thermal decomposition step.

### 3.2.9 Capacitance measurement of the comb test structures

The capacitance of a comb test device was measured using a Keithley 590 CV analyzer and Cascade Microtech Alessi REL-4800 Probe Station at room temperature. The capacitance of the devices was measured at 1 MHz frequency with a voltage sweep from -1 V to 1 V. The effective dielectric constants of Cu/air-gap and extended Cu/air-gap structure were evaluated by comparing the measured capacitance of these structures to the measured capacitance of Cu/SiO<sub>2</sub> structure.

## **CHAPTER 4: ELECTRON-BEAM HARDENING OF NORBORNENE-BASED SACRIFICIAL POLYMERS**

### **4.1 Background of electron-beam hardening of polymer thin films**

As the minimum feature size of microelectronic devices continues to shrink, the development of new materials is needed for low-k insulators and high resolution patterning of devices. Copper has been used in on-chip interconnect since 1998 with silicon dioxide insulation. Further reduction in the resistance-capacitance (RC) delay is possible by lowering the dielectric constant (low-k) of the insulator, has been identified in the National Technology Roadmap for Semiconductors as being critical to the realization of high performance interconnections [45,46]. Numerous approaches to achieving low-k materials are being pursued, including polymers, spin-on-glasses, and foams [47]. However, air-gaps provide the lowest effective dielectric constant available [16].

Air-gaps encompass the use of air, or more accurately, the use of a gas as the dielectric material separating electrical conductors. Air-gaps can be formed by thermally decomposing the sacrificial polymer as a place-holder and allowing the gas byproducts to diffuse through the encapsulating dielectric. During the thermal decomposition process, the gas byproduct in a cavity between metal conductors in a

back-end-of-the-line interconnection structure on ICs will quickly come into equilibrium with the ambient atmosphere. If air is the ambient gas, air will exchange with the original gas byproducts in a cavity, and thus air-gaps for intra-metal dielectric are fabricated. The thermal, mechanical properties, and percent residue after decomposition are important for the performance of these air-gaps as intra-metal dielectrics.

Polynorbornenes have been used in 193 nm photoresist, low- $k$  insulators, and as a sacrificial polymer for the fabrication of air-gap structure in semiconductor devices [16]. This study focuses on norbornene formulations, which have a narrow decomposition temperature window and can be used as sacrificial materials [24,48]. Butyl-polynorbornene (BuPNB)-triethoxy silyl-polynorbornene (TESPNB) copolymer is a functionalized polynorbornene copolymer. Butyl and triethoxysilane substituent groups are attached to norbornene in order to increase elongation-to-break and enhance the adherence of the norbornene polymer to the substrate, respectively [24,48]. Functionalized norbornene polymers are attractive low- $k$  dielectrics [32] and have been shown to possess excellent mechanical, electrical, and chemical properties. However, for the formation of air-gaps using the dual damascene process [16], the sacrificial polymer must have sufficient hardness not to deform during chemical mechanical polishing (CMP). Further, sub-micrometer wide

polymer patterns can distort in the fabrication processes if the polymer is not suitably hard. Hence, a polymer with higher modulus is desirable. In this study, it is of interest to increase the hardness of functionalized polynorbornene without degrading the thermal stability of the polymer.

During electron beam irradiation, the electron loses kinetic energy and momentum due to interactions with the polymer. This interaction between the electron and the polymer thin films can be modeled based on the coulombic interaction between the nucleus and its surroundings electrons with the incoming electron. There are two types of interactions: elastic and inelastic scattering [49]. Inelastic scattering is of most interest because it involves transfer of electron energy to the polymer leading to bond scission or crosslinking depending on the structure of the polymer particular chemical bonds broken. The energy loss due to inelastic scattering can be approximated by Bethe continuous energy loss approximation [49] as shown in Equation (4.1).

$$\frac{dE}{dx} = \left[ \frac{N_A \cdot e^4}{2\pi\epsilon_0^2} \right] \left[ Z \frac{\rho}{A} \right] \left[ \frac{1}{E} \ln \left\{ \frac{E}{66J} \right\} \right] \quad (4.1)$$

where E is the energy of the electron at distance x from the surface, Z is the atomic number of a material, A is the atomic weight (g/mol), ρ is the density of the material



(g/cm<sup>3</sup>),  $\epsilon_0$  is the permittivity of space,  $8.85 \times 10^{-12}$  C<sup>2</sup>/Nm<sup>2</sup>, and J is the mean ionization potential (keV) which can be approximated by  $11.5 \times Z$ .

Previously, electron beam irradiation has been used for polymerizing monomers, curing polymers, and hardening the surface of materials [50-52]. For example, in the electron beam radiation of acrylates [50], the irradiation generates radicals at random sites which leads to polymerization and crosslinking via free radical formed at the end of the polymer chains in the backbone. Cross-linking occurs via radical-radical recombination or radical attack of an acrylate group.

A thermal curing reaction usually requires the addition of chemical additives to the polymer or polymer solution, which act as a reactant or catalyst in the reaction. The chemical additives and effects of the chemical by-products can degrade the polymer properties. In contrast, electron beam irradiation does not require chemical additives and high temperature as in thermal curing. Manepalli et al. [51,52] have studied electron beam curing of functionalized polynorbornene polymers as a low- $k$  dielectric for electrical interconnections. However, the specific properties of the films necessary for sacrificial materials, such as hardness and after decomposition residue, were not evaluated in the previous study.

In this study, thin films of polynorbornene were exposed to electron beam irradiation to cause cross-linking in the polymer and enhancement of the hardness of

the copolymer thin films. The effect of the electron beam energy, dose, and chamber temperature on the thermal, mechanical, and degradation properties of the copolymer thin films were investigated.

## **4.2 Experiments**

In this study, a random copolymer of butylnorbornene (BuPNB)-triethoxysilyl polynorbornene (TESPNB) was spin-coated onto Si substrates. The polymer was provided by Promerus LLC (Brecksville, OH). This copolymer consisted of 90 mol% BuPNB and 10 mol% TESPBNB. The chemical structures of the monomer units are shown in Figure 4.2.1. Mesitylene was used as the casting solvent. The polymer solution was spin-coated onto Si-substrate and soft-baked at 100°C for 5 min on a hotplate. The samples then were heated at 300°C for 1 hour in a nitrogen purged furnace to remove the solvent. The furnace was purged for 30 minutes prior to heating and sample entry. The polymer thickness after solvent removal was 1  $\mu\text{m}$ , unless otherwise noted.

Electron beam irradiation was preformed in an Electroncure 30-200-AT system (Honeywell Electron Vision, San Diego, CA). The samples were flood exposed to the electrons at a specific energy. Nitrogen was used as the process gas in the electron beam chamber. The chamber was twice evacuated and purged using

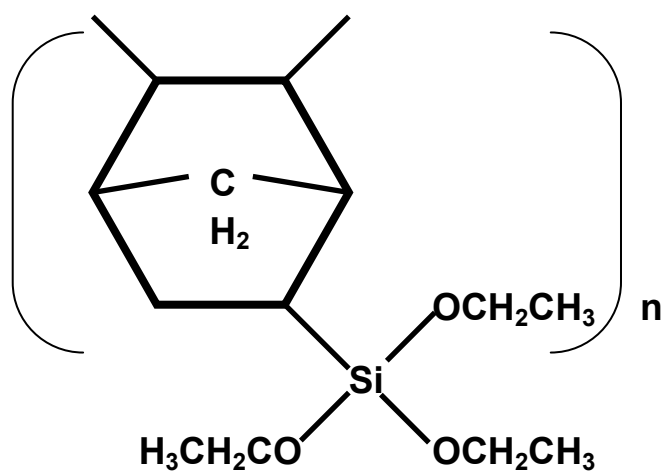
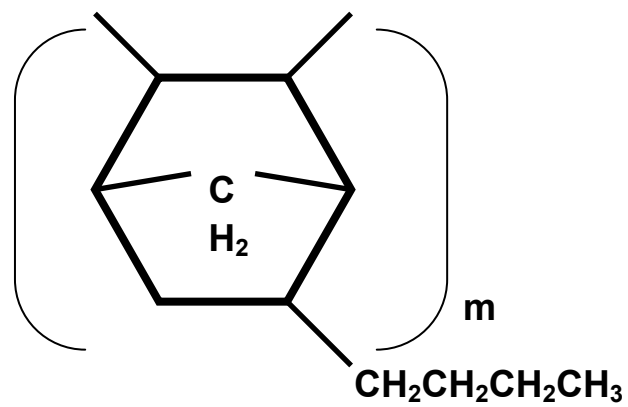


Figure 4.2.1 The chemical structures of the norbornene monomer units (a) butyl norbornene (b) triethoxy silyl norbornene.

nitrogen prior to electron beam exposure, The effect of electron energy, electron dose, and the chamber temperature on the thermal, mechanical, and decomposition properties of BuPNB-TESPNB thin films were investigated.

Dynamic thermal gravimetric analysis (Seiko Instruments) was used to investigate the effect of electron beam exposure on the thermal properties of the films. The mechanical properties of electron beam exposed samples (i.e. hardness and modulus) were measured using a TriboIndenter (Hysitron Inc. Minneapolis, MN). The indentation system was enclosed in a acoustic housing and located on a anti-vibration table. For indentation, the Z-axis resolution was 0.04 nm. A three-sided Berkovich tip was used [53]. The maximum force was chosen so as to indent 10% of the film thickness.

A Bruker IFS66V (Bruker Optics Inc., Billerica, MA) Fourier transform infrared spectrometer (FTIR) was used in transmission mode to investigate the structural changes in of the polymer. The spectra were scanned from  $500\text{ cm}^{-1}$  to  $4500\text{ cm}^{-1}$  at  $4\text{ cm}^{-1}$  resolution.

A VG 70SE pyrolyzer-mass spectroscopy (MS) with electron ionization (EI) was used to investigate the effect of electron energy on the structural variation of polymer thin films. The data was collected from 30 Da to 700 Da as a function of temperature.

### 4.3 Results

The penetration depth of electrons into a polymer thin film and the degree of bond scission or crosslinking is a function of the electron energy and dose. The electron energy distribution in the polymer was calculated by integrating Equation 4.1. Figure 4.3.1 shows the electron energy distribution where the incident energy of the electron beam was 1 keV, 5 keV, and 10 keV. The polymer film was assumed to contain only carbon for the calculation. The average penetration depth of 1, 5 and 10 keV electrons is 0.073, 0.9, and 3.15  $\mu\text{m}$ , respectively. One micrometer thick polymer films were e-beam irradiated at 1 keV, 5 keV, and 10 keV. At an electron energy of 5 keV, the electrons penetrate the full thickness of the polymer film. Higher (10 keV) and lower (1 keV) e-beam exposures were performed to explore the effect of under and lower penetration depths.

#### 4.3.1 The effect of electron energy on the properties of polymer thin films

The TGA spectra of polymer films irradiated at a dose of 2000  $\mu\text{C}/\text{cm}^2$  as a function of exposure temperature is shown in Figure 4.3.2. The nanoindentation results (force vs. depth) for each exposure conditions are shown in Figure 4.3.3. The control sample was the same thickness polymer film without e-beam irradiation. The unexposed (i.e. control) film and the 1 keV e-beam exposed film showed

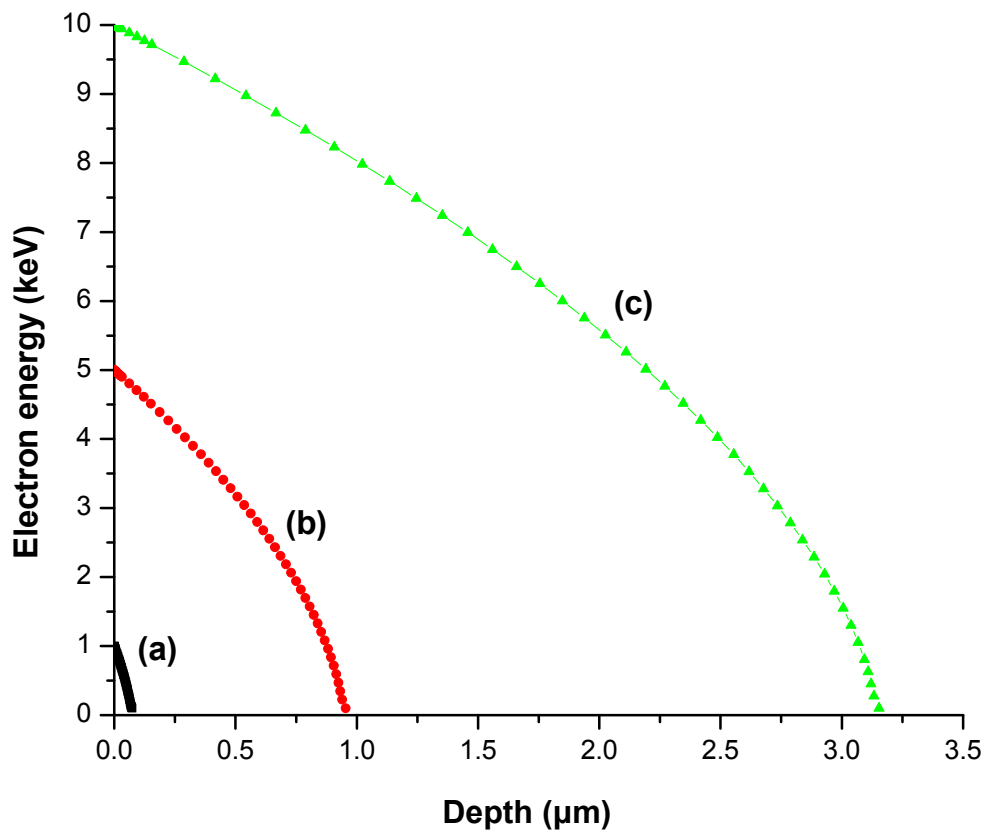


Figure 4.3.1 Electron energy distribution vs. depth for (a) 1keV (b) 5keV (c) 10keV

e-beam energy.

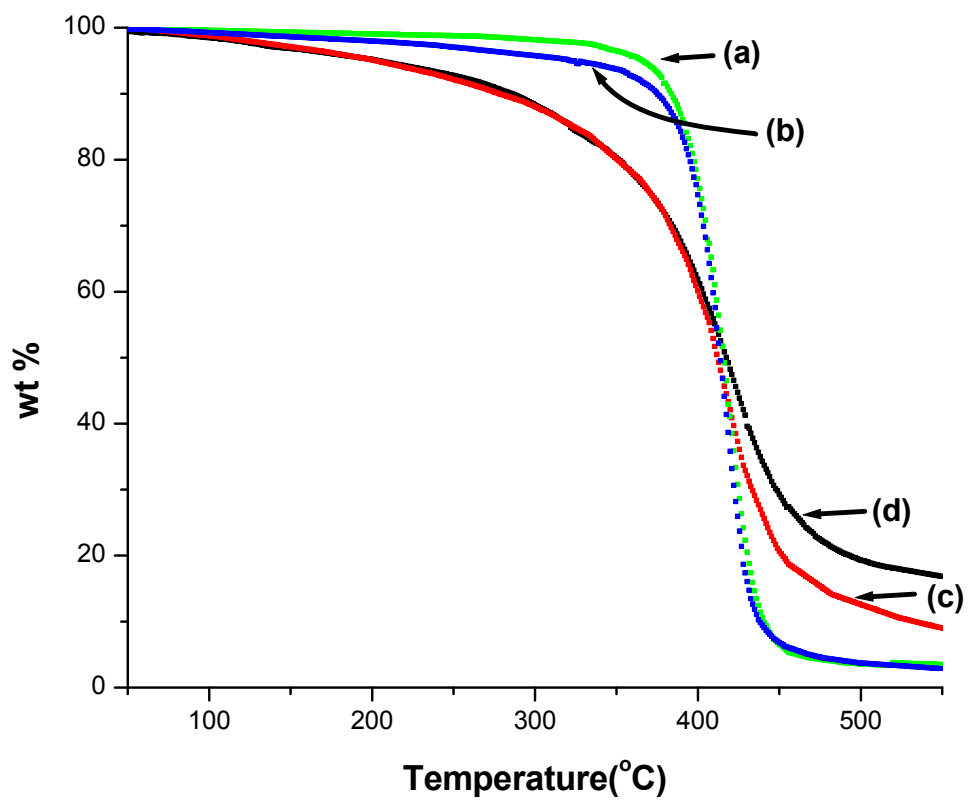


Figure 4.3.2 Dynamic TGA of polymer films e-beam irradiated at  $2000 \mu\text{C}/\text{cm}^2$

dose: (a) control sample (b) 1keV, 100°C (c) 5keV, 100°C (d) 10keV, 100°C.

similar decomposition properties as a function of temperature, as will be shown below. However, in Figure 4.3.3, the indentation depth, at the same force, of the film exposed to 1 keV e-beam is deeper than that of the control sample, showing that the e-beam irradiated sample was softer than the control sample. The electron penetration depth at 1 keV was about 73 nm, and hence the remaining film depth was not irradiated. A possible explanation for the decrease in film hardness with 1 keV exposure is that bond scission of polymer backbone exceeds the hardening due to cross-linking. Hence, chain scission dominates over chain cross-linking at low e-beam energies.

Samples irradiated at 5 keV and 10 keV showed a smaller indentation depth compared to the 1 keV e-beam or control sample, as shown in Fig. 4.3.3. This increase in hardness and elasticity at 5 keV and 10 keV is likely due to a higher level of cross-linking compared chain scission. The thermal stability of the 5 keV and 10 keV films had similar thermal stability, as measured by TGA, and hardness. Hence, at a dose of  $2000 \mu\text{C}/\text{cm}^2$ , the 5 keV e-beam energy is sufficient to cause cross-linking. Films irradiated at 10 keV e-beam energy resulted in a higher percentage of residue. This will be discussed in the next section.

The composition of the gaseous byproducts during thermal decomposition of the polymer after e-beam irradiation was investigated by MS. The MS spectra for



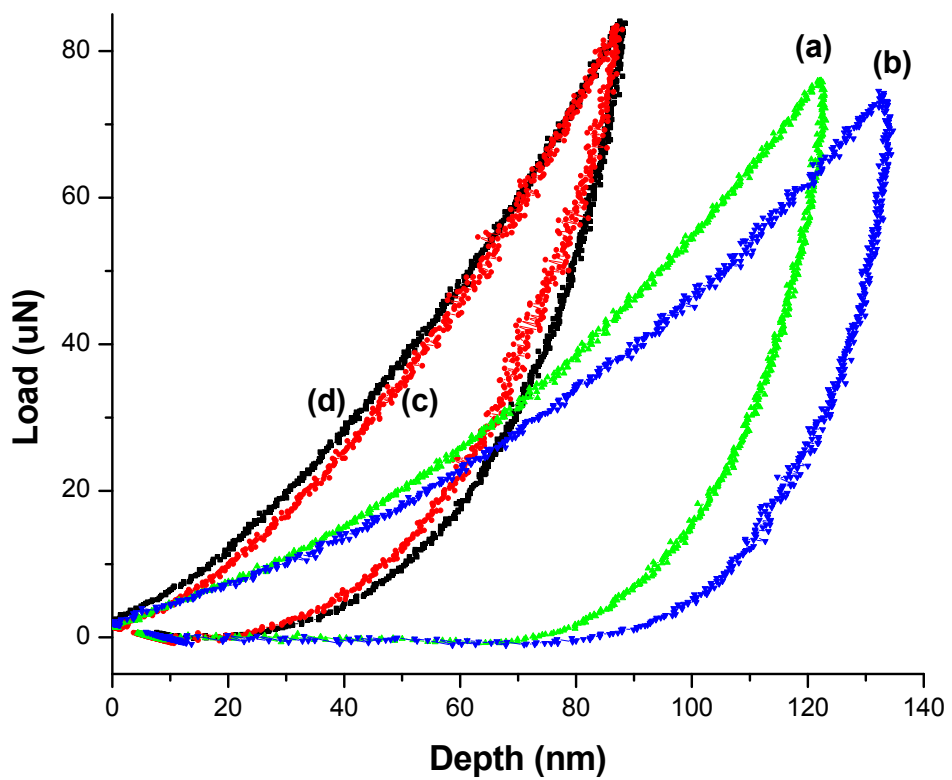
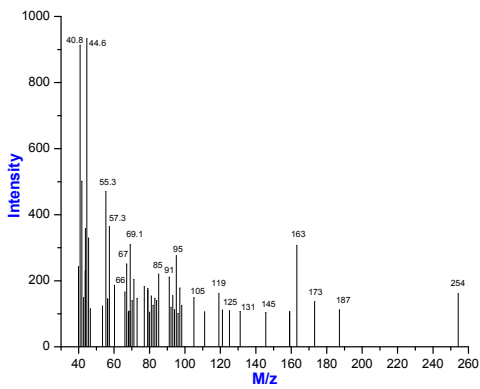


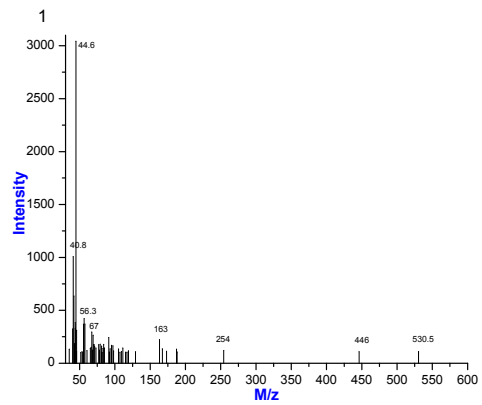
Figure 4.3.3. Nanoindentation for polymers e-beam irradiated at  $2000 \mu\text{C}/\text{cm}^2$  dose

(a) control sample (b) 1 keV,  $100^\circ\text{C}$  (c) 5 keV,  $100^\circ\text{C}$  (d) 10 keV,  $100^\circ\text{C}$ .

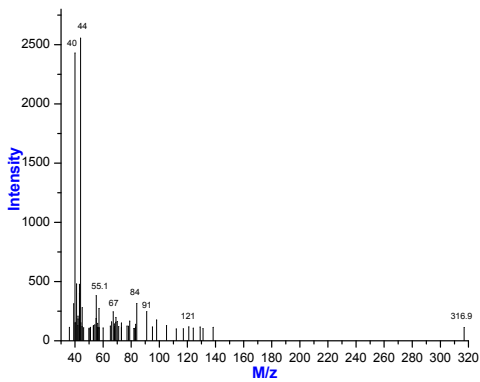
the gaseous products vaporized at 350°C and 400°C are shown in Figures 4.3.4 and 4.3.5, respectively. The decomposition products are primary fragments from the polymer. Table 4.3.1 shows the most probable species to result from the fragmentation of the BuPNB-TESPNB polymer. The triethoxysilane side group (TES) contributes peaks at 163, 228, 254, 530, 647, and 662 m/z. The norbornene monomer is observed at 93 m/z and cyclopentadiene, which is generated by ethylene elimination from norbornene, is observed at 66 m/z [54]. Fig. 4.3.4 also shows higher molecular weight oligomers: trimers and tetramers of norbornene including the TES group, at 350°C for the 1 keV e-beam exposure. This data supports the indentation results where the 1 keV e-beam exposure results in a higher level of backbone scission resulting in lower molecular weight products. Cross-linking of the functionalized norbornene can occur through the reaction of siloxane groups to form Si-O-Si bonds [55]. If functionalized polynorbornene was crosslinked through the siloxane groups, then the Si-O-Si bonds should be stable to a temperature in excess of 400°C. The TES related peaks (163, 228, 254, 530, 647, 662) included the fragments of TES were only found in the control and 1 keV exposure films (see Figure 4.3.4 and 4.3.5) indicating that these two samples were not cross-linked through the siloxane groups. In contrast, the TES related peaks were not detected until 420°C in the 5 keV and 10 keV e-beam samples, indicating that the siloxane



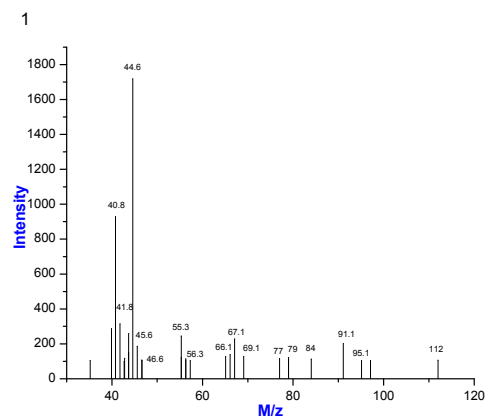
a) control sample



b) 1keV exposure

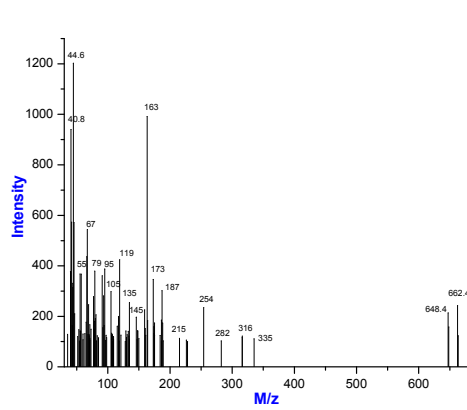


c) 5keV exposure

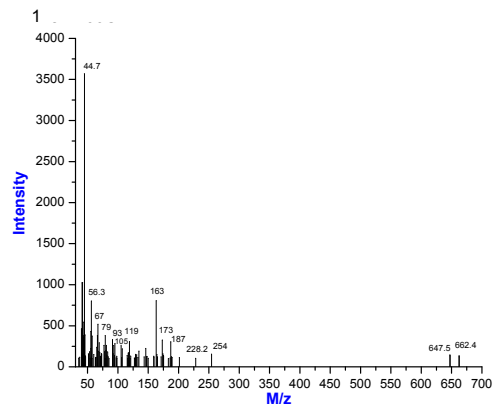


d) 10keV exposure

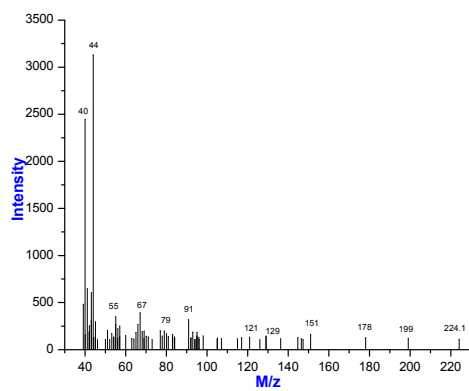
Figure 4.3.4 Pyrolyzer-MS spectra at 350°C a) control sample, b) 1 keV, 2000  $\mu\text{C}/\text{cm}^2$ , 100°C, c) 5 keV, 2000  $\mu\text{C}/\text{cm}^2$ , 100°C, d) 10 keV, 2000  $\mu\text{C}/\text{cm}^2$ , 100°C.



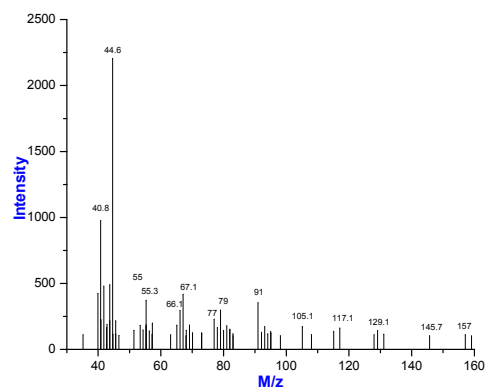
a) control sample



b) 1keV exposure



c) 5keV exposure

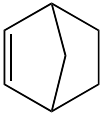

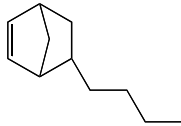
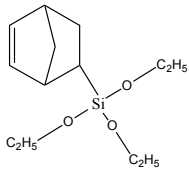
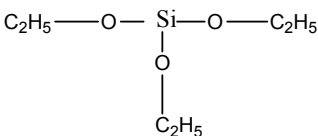
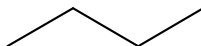
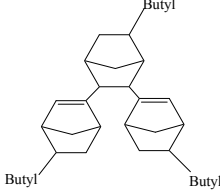
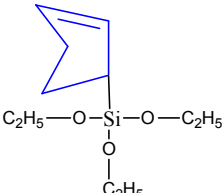
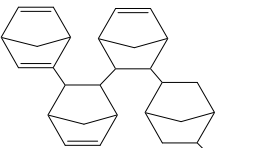
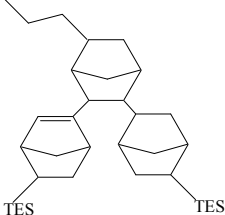
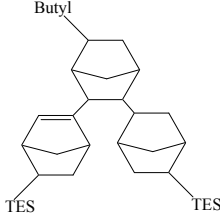


d) 10keV exposure

Figure 4.3.5 Pyrolyzer-MS spectra at 400°C a) control sample, b) 1 keV, 2000  $\mu\text{C}/\text{cm}^2$ , 100°C, c) 5 keV, 2000  $\mu\text{C}/\text{cm}^2$ , 100°C, d) 10 keV, 2000  $\mu\text{C}/\text{cm}^2$ , 100°C.

Table 4.3.1 The most probable peak identifications for the gas byproducts of

BuPNB-TESPNB.

<p>Norbornene C<sub>7</sub>H<sub>9</sub>, 93 Norbornane C<sub>7</sub>H<sub>11</sub>, 95</p>		<p>Cyclopentadiene C<sub>5</sub>H<sub>6</sub>, 66</p>	
<p>Butyl norbornene (BuNB) C<sub>11</sub>H<sub>18</sub>, 150</p>		<p>Triethoxy silyl norbornene (TESNB) C<sub>13</sub>H<sub>22</sub>O<sub>3</sub>Si, 254</p>	
<p>Triethoxy silane(TES) C<sub>6</sub>H<sub>15</sub>O<sub>3</sub>Si, 163</p>		<p>Fragments of TES</p>	<p>79,91,105,119,135,145</p>
<p>Butyl C<sub>4</sub>H<sub>9</sub>, 57</p>		<p>Trimer of BuNB C<sub>33</sub>H<sub>50</sub>, 446</p>	
<p>C<sub>11</sub>H<sub>20</sub>O<sub>3</sub>Si, 228</p>		<p>Tetramer of norbornene including TES, C<sub>34</sub>H<sub>46</sub>O<sub>3</sub>Si, 530</p>	
<p>C<sub>21</sub>H<sub>25</sub>(C<sub>3</sub>H<sub>7</sub>) (C<sub>6</sub>H<sub>15</sub>O<sub>3</sub>Si)<sub>2</sub> 647</p>		<p>C<sub>21</sub>H<sub>26</sub>(C<sub>4</sub>H<sub>9</sub>) (C<sub>6</sub>H<sub>15</sub>O<sub>3</sub>Si)<sub>2</sub> 662</p>	

was reacted in those samples. These MS results in combination with the mechanical property data indicate that scission of the polymer backbone at 1 keV exposure makes the films softer than the control films. Cross-linking of the 5 keV and 10 keV hardens the polymer films.

#### 4.3.2 The effect of electron dose on the properties of polymer thin films

Dynamic TGA and nanoindentation results for 2000  $\mu\text{C}/\text{cm}^2$ , 1000  $\mu\text{C}/\text{cm}^2$ , and 500  $\mu\text{C}/\text{cm}^2$  at 5 keV electron energy are shown in Figures 4.3.6 and 4.3.7, respectively. The chamber temperature during exposure was 50°C, and nitrogen was used as the process gas. As seen in Figure 4.3.6, the weight loss increased from 5% at 500  $\mu\text{C}/\text{cm}^2$  dose to 13% at 2000  $\mu\text{C}/\text{cm}^2$ , compared to the control sample which had 1% weight loss. Hence, as the electron dose was increased, the thermal stability of the polymer at 300°C decreased. An increase in the electron dose increased the hardness of the polymer, as shown in Figure 4.3.7 due to added cross linking.

#### 4.3.3 The structure change due to electron beam irradiation

FTIR was used to investigate the structural variation of the polymer films after e-beam exposure. Figure 4.3.8 shows the FTIR spectra for the e-beam irradiated

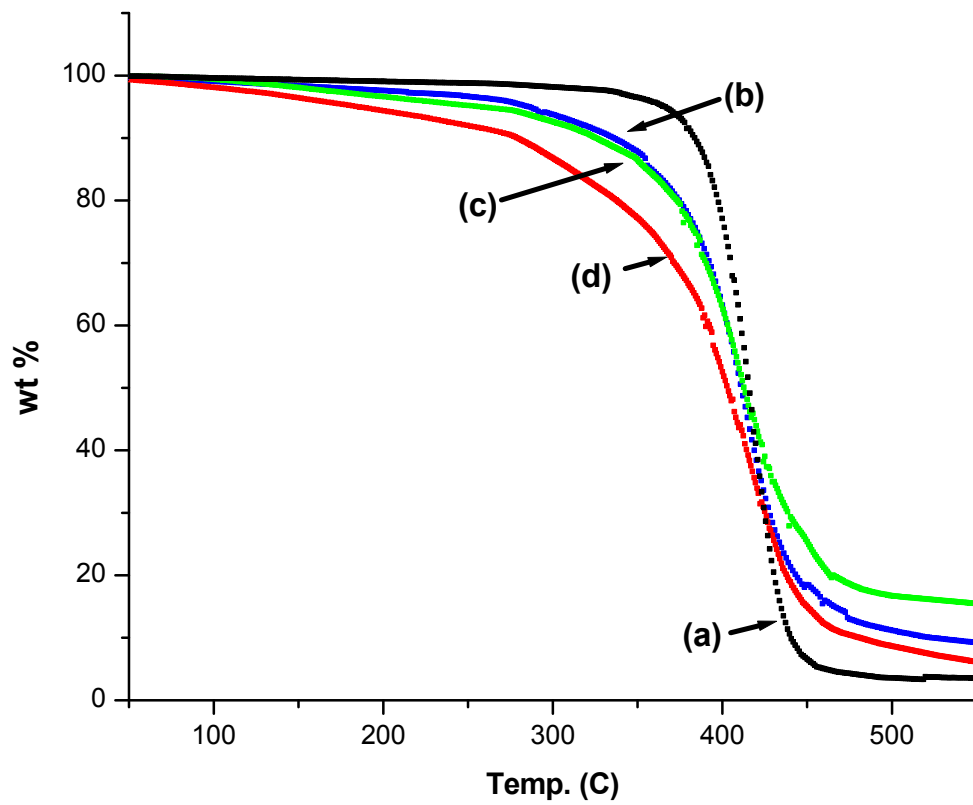


Figure 4.3.6 Dynamic TGA of polymer films irradiated at 5 keV energy: (a) control sample, (b)  $500 \mu\text{C}/\text{cm}^2$ ,  $50^\circ\text{C}$ , (c)  $1000 \mu\text{C}/\text{cm}^2$ ,  $50^\circ\text{C}$ , and (d)  $2000 \mu\text{C}/\text{cm}^2$ ,  $50^\circ\text{C}$ .

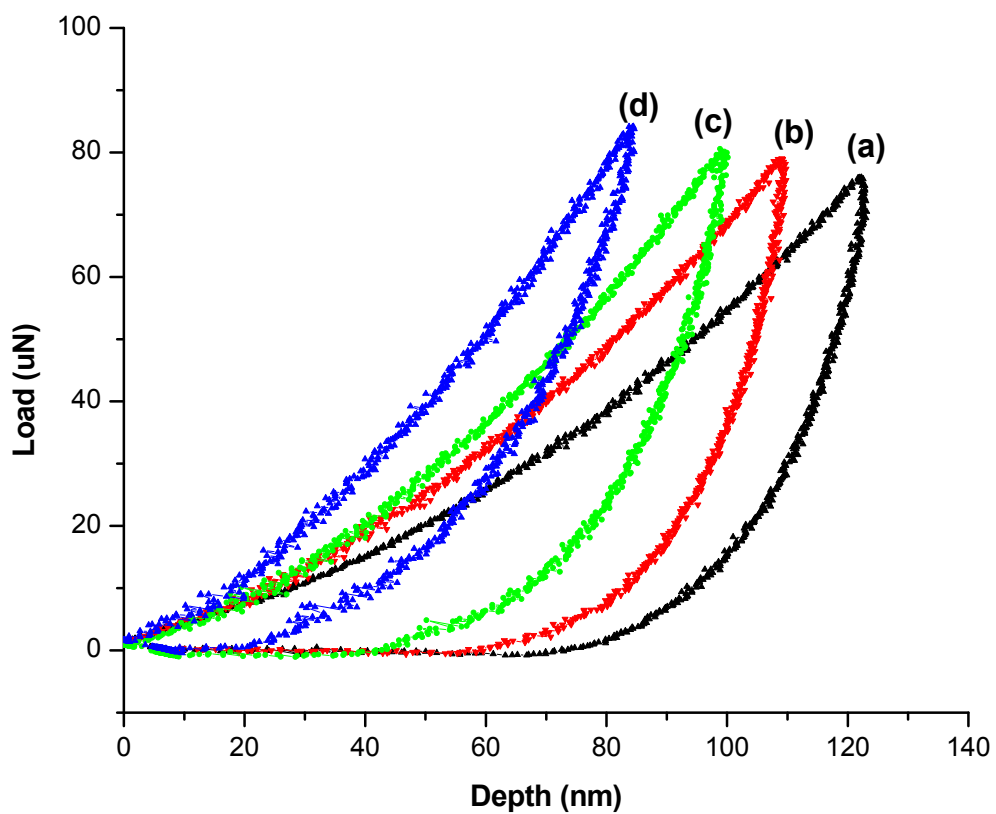


Figure 4.3.7 Nanoindentation of polymer films irradiated at 5 keV electron energy:

- (a) control sample, (b) 500  $\mu\text{C}/\text{cm}^2$ , 50°C, (c) 1000  $\mu\text{C}/\text{cm}^2$ , 50°C, and  
(d) 2000  $\mu\text{C}/\text{cm}^2$ , 50°C.



polymers. Several of the significant peaks are identified: CH<sub>3</sub>/CH<sub>2</sub> stretching (2830-2960cm<sup>-1</sup>), carbonyl group (1725-1710cm<sup>-1</sup>), CH<sub>3</sub>/CH<sub>2</sub> bending (1350-1450cm<sup>-1</sup>), and triethoxysilane (1166, 1105, 1080, 955cm<sup>-1</sup>). The films exposed at 5 keV and 10 keV had smaller peak heights for the CH<sub>3</sub>/CH<sub>2</sub> stretching, broadening of the CH<sub>3</sub>/CH<sub>2</sub> bending and triethoxysilane, and increase in the carbonyl band (1720cm<sup>-1</sup>). The 1 keV e-beam sample was nearly the same spectra as the control sample except for the carbonyl band at 1720cm<sup>-1</sup>. The height of the carbonyl peak for the 1 keV sample was smaller than the peak for the 5 keV and 10 keV samples. The oxidation of an organic polymer generally proceeds through the formation of free radicals that can react with oxygen to form peroxides or hydroperoxides that can react with other radicals. The oxidation of the irradiated films resulting in formation of the carbonyl structure is a result of the e-beam induced bond-breaking and quenching with oxygen following exposure. Oxidation of polynorbornene thin films results in yellowing of the colorless films. The oxidation of polynorbornene also results in a decrease in the CH<sub>3</sub>/CH<sub>2</sub> stretching (2830-2960cm<sup>-1</sup>) peaks and the appearance of Si-OH at 3600 to 3200 cm<sup>-1</sup> and carbonyl at 1725 and 1710cm<sup>-1</sup> [55]. After e-beam exposure, the films also yellowed. The oxidation mechanism of functionalized polynorbornene has been previously discussed [55]. The carbonyls and Si-OH groups shown in Figure 4.3.8 can result from a free radical mechanism, created

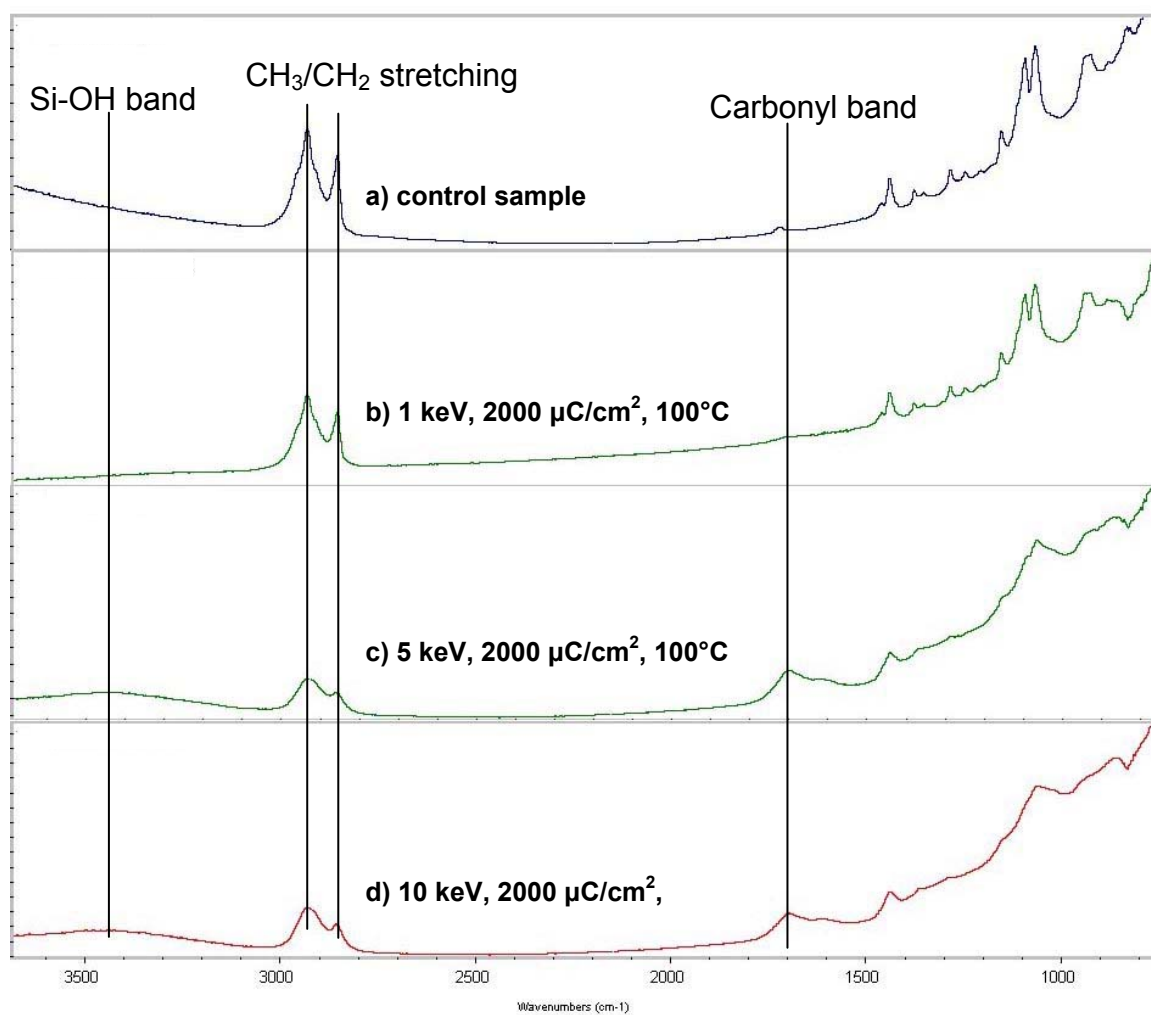


Figure 4.3.8 FTIR spectra for (a) control sample (b) 1 keV, 2000  $\mu\text{C}/\text{cm}^2$ , 50°C (c) 5 keV, 2000  $\mu\text{C}/\text{cm}^2$ , 100°C and (d) 10 keV, 2000  $\mu\text{C}/\text{cm}^2$ , 100°C.

during e-beam irradiation.

The formation of free radicals is a result of e-beam exposure. Table 4.3.2 shows the ratio of various FTIR peaks to the C-H stretching peak. As shown in Table 4.3.2, the ratio of the area of the carbonyl peak increased with e-beam dose and electron energy. The increase in area of the carbonyl peak corresponds to a higher level of oxidation of the polymer. In addition, the thermal stability of the polymer was degraded (Fig. 4.3.2 and 4.3.6) at high electron energy and dose. The hardness of the films was enhanced in Figure 4.3.3 and 4.3.7.

#### 4.3.4 The aging effect

In Table 4.3.2, the ratios of OH stretching, carbonyl and triethoxysilane peaks to the C-H stretching at right after exposure and after 2 month are shown. The carbonyl and Si-OH peaks are compared to the area of the CH<sub>3</sub>/CH<sub>2</sub> stretching peak as a function of time following the e-beam irradiation. The relative area of the carbonyl band dramatically increases with time, while the relative area of the Si-OH peak decreases with time. From the change in the FTIR peaks in Table 4.3.2, it can be concluded that post e-beam exposure results in continued air-oxidation of the polymer over time, where carbon radicals or other species are oxidized to a carbonyl and Si-OH is transformed to other forms. The TGA for an e-beam exposed polymer

Table 4.3.2. The area ratio of major FTIR spectra peaks to CH stretching peak.

Electron beam		CH stretching	carbonyl	triethoxysilane
Control sample	Right after exposing	1.0	-	0.27
	After 2 month	1.0	-	0.33
1 keV, 1000 $\mu\text{C}/\text{cm}^2$ , 100°C,1mA	Right after exposing	1.0	0.05	0.28
	After 2 month	1.0	0.29	0.21
5 keV, 2000 $\mu\text{C}/\text{cm}^2$ , 100°C,1mA	Right after exposing	1.0	0.83	0.33
	After 2 month	1.0	2.87	0.23
10 keV, 1000 $\mu\text{C}/\text{cm}^2$ , 100°C,1mA	Right after exposing	1.0	0.26	0.26
	After 2 month	1.0	1.61	0.10
10 keV, 2000 $\mu\text{C}/\text{cm}^2$ , 150°C,1mA	Right after exposing	1.0	0.45	0.26
	After 2 month	1.0	2.29	0.17

films (5 keV, 500  $\mu\text{C}/\text{cm}^2$ , 50°C) was compared immediately after exposed and after 2 months, as shown in Figure 4.3.9. Films measured after 2 months following exposure exhibit a decrease in thermal stability at the low temperature. A higher percent residue was observed with time, compared to films measured immediately after exposure.

#### 4.3.5 The effect of operating gas on the properties of polymer thin films

It appears that polymer oxidation occurs during e-beam exposure in the chamber from residual air impurities, and after exposure when the polymer is held in air. To reduce the oxygen concentration in the e-beam tool and provide a reducing atmosphere during processing, a mixture of 2% hydrogen and 98% nitrogen was used as the e-beam process gas. The effects of the hydrogen treatment on the thermal and mechanical properties of the polymer are shown in Figures 4.3.10 and Figure 4.3.11. The 2% hydrogen and 98% nitrogen treatment improves the thermal stability and decreases the residue content after decomposition of the polymer at temperatures below 400°C, as shown in Fig. 4.3.10. The hardness of the copolymer thin films decreases by using a mixture of 2% hydrogen and 98% nitrogen compared with pure nitrogen, as shown in Fig. 4.3.11. Since oxidation of the polymer coincides with hardening of the films, lowering the oxygen concentration in process

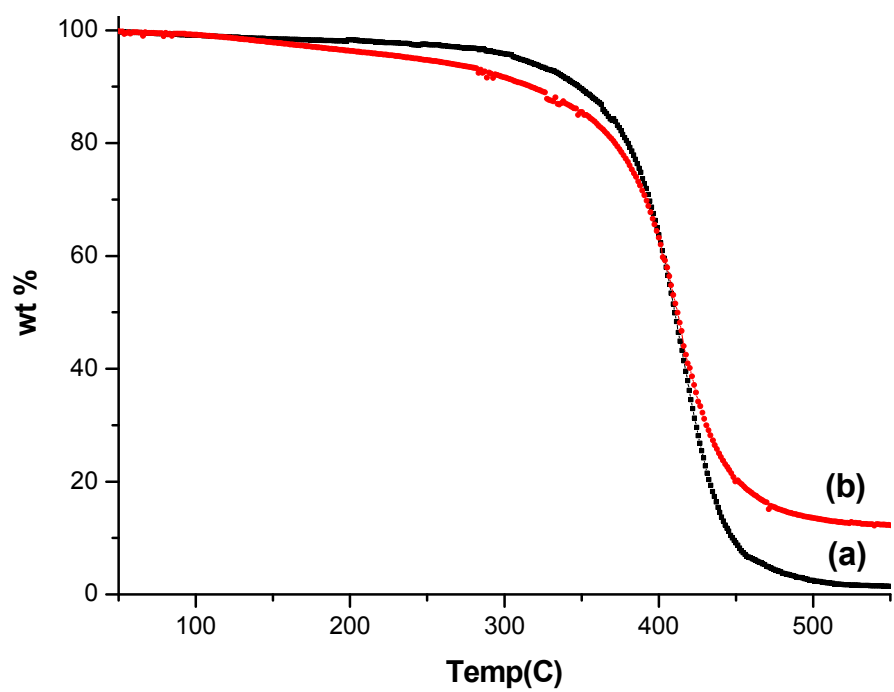


Figure 4.3.9 Dynamic TGA for a polymer exposed to 5 keV,  $500 \mu\text{C}/\text{cm}^2$ ,  $50^\circ\text{C}$ : (a) immediately after exposure and (b) after 2 month of air storage.

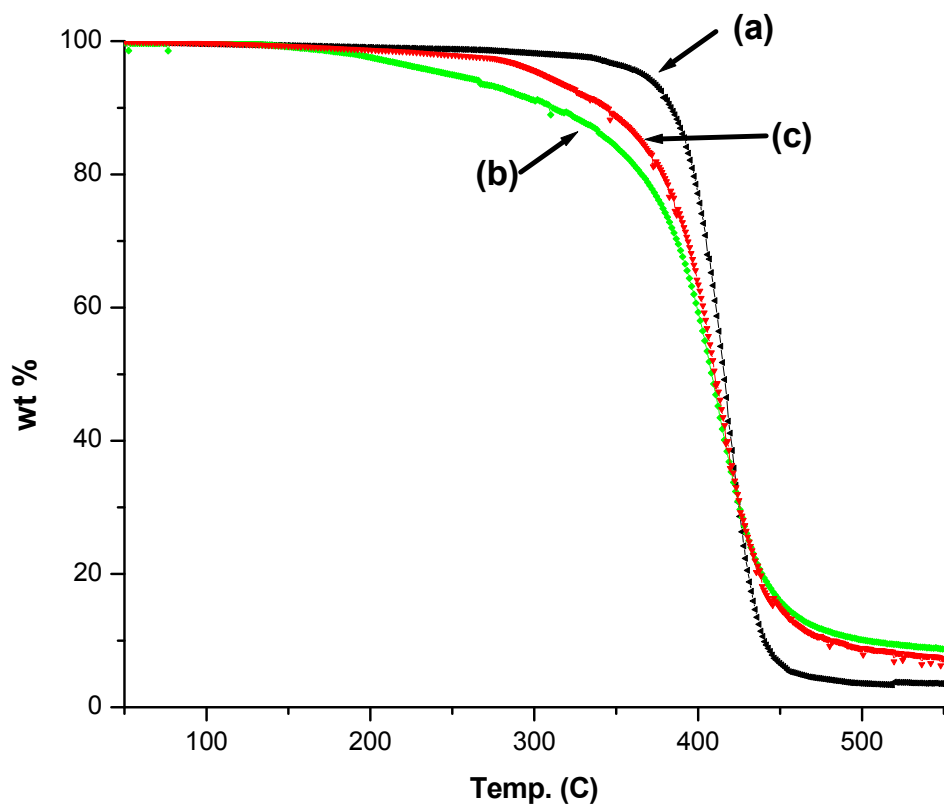


Figure 4.3.10 Dynamic TGA for polymer films e-beam exposed at 5 keV, 500  $\mu\text{C}/\text{cm}^2$ , 50°C, using different purging gas (a) control sample (b) nitrogen purged sample during exposing (c) 2% hydrogen balanced nitrogen purged sample during exposure.

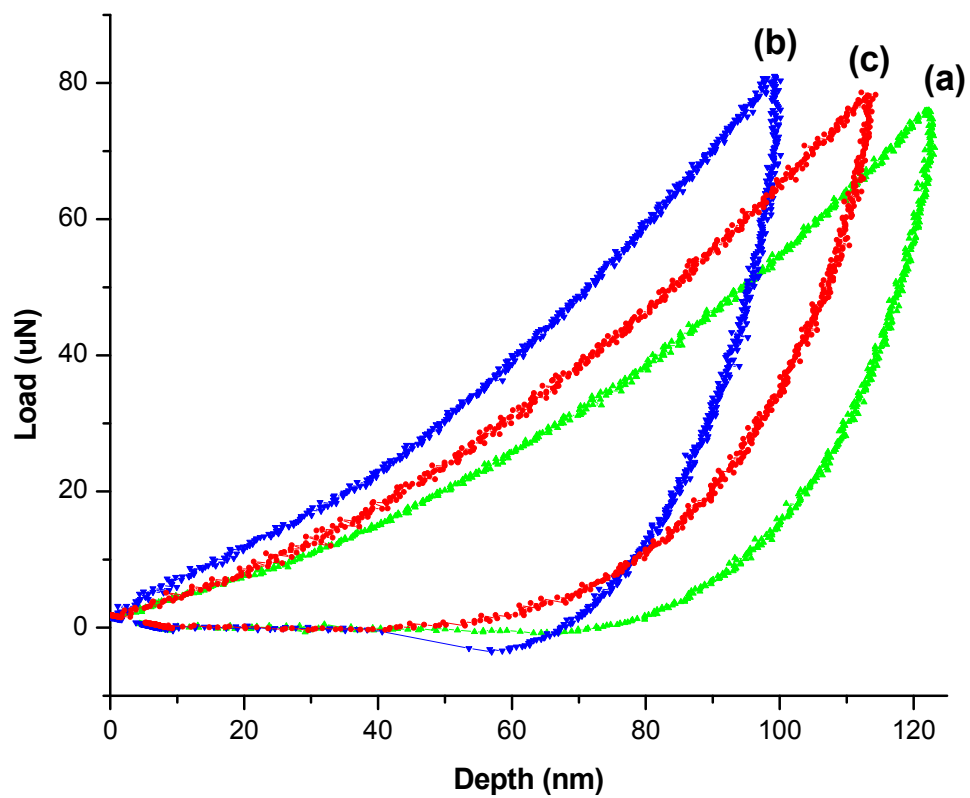


Figure 4.3.11 Nanoindentation of the polymer films exposed to 5 keV,  $500 \mu\text{C}/\text{cm}^2$ ,  $50^\circ\text{C}$  e-beam using different purging gases: (a) control sample (b) nitrogen exposure (c) 2% hydrogen and 98% nitrogen.



gas results in less oxidation and probably cross linking.

#### 4.3.6 The effect of temperature on the properties of polymer thin films

During e-beam exposure, TES and carbon-carbon polymer bonds are attacked by electron irradiation, as shown in Fig. 4.3.8. Once radicals are generated, the depropagation and transfer reactions of radicals can occur [24]. Depropagation and intramolecular transfer reactions result in products which are volatile at modest temperatures. The intermolecular transfer reaction generally results in higher molecular weight products and cross linking reactions. According to the TGA results shown in Figure 4.3.2 and 4.3.6, volatile products are observed, especially for 5 keV and 10 keV exposures. To lower the amount of volatile products evolved at 300°C, the films were heated to 300°C for 1 hour under vacuum in the e-beam chamber after e-beam exposure. The samples were brought to room temperature prior to being exposed to air. Figure 4.3.12 shows TGA results for the polymer films e-beam irradiated at 5 keV, 2000  $\mu\text{C}/\text{cm}^2$ , and 100°C in nitrogen, along with the control sample. Heating the samples under vacuum after e-beam exposure results in a decrease in the amount volatile species retained by the polymer. However, the hardness of the post e-beam heated samples decreased, as shown in Fig. 4.3.13.

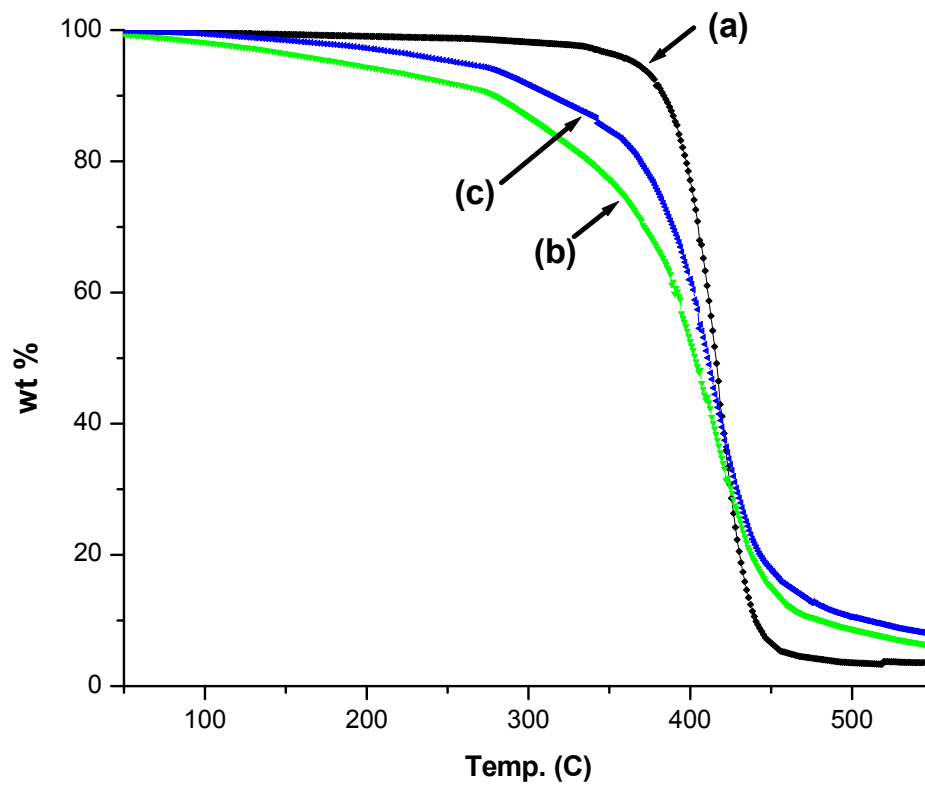


Figure 4.3.12 Dynamic TGA for the polymer e-beam exposed at 5 keV, 2000  $\mu\text{C}/\text{cm}^2$ , (a) control sample at 100°C (b) ambient temperature, and (c) heated to 300°C in the e-beam chamber after irradiation.

#### 4.4 Conclusion

Electron beam irradiation of norbornene-based polymers increases the film hardness via cross linking, but degrades the thermal properties, as measured by the amount of volatiles. Generally, when films are exposed to e-beam irradiation, scission and cross linking reactions compete. In the case of 1 keV e-beam exposure, polymer scission dominates and results in softer films than unexposed films. In contrast, 5 keV and 10 keV exposure resulted in increased hardness of the polymer films. The hardness of the polymer films increase at higher electron doses; however, the thermal stability decreases resulting in higher residue content. At high e-beam energy and dose, cross linking dominates. As a result, the hardness of the films is enhanced. The higher energy e-beam exposures resulted in a reduction of the CH<sub>3</sub>/CH<sub>2</sub> stretching, the broadening of the CH<sub>3</sub>/CH<sub>2</sub> and TES bending. The appearance of the carbonyl band at 1720cm<sup>-1</sup> was the result of post-exposure oxidation. To reduce the oxidation of the polymer after e-beam exposure, the films were exposed to 2% hydrogen and 98% nitrogen gas mixture and heated under vacuum prior to air exposure. These treatments resulted in an enhancement in thermal properties.

In conclusion, the results in this study show that polymer thin films can be hardened by e-beam exposure, and e-beam exposure can be applied for the

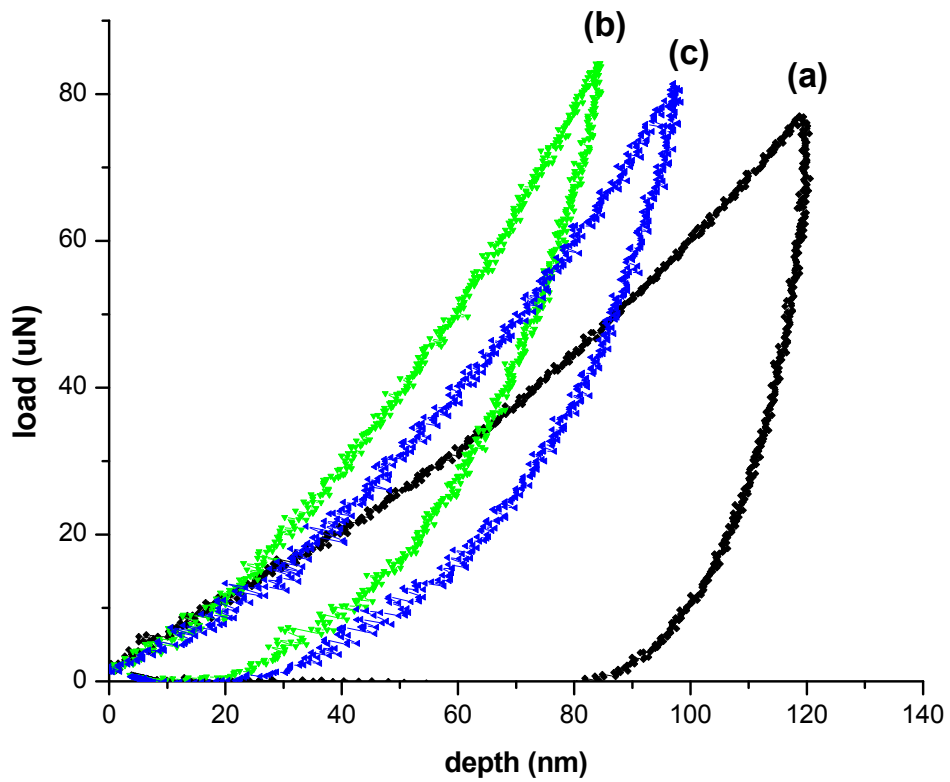


Figure 4.3.13 Nanoindentation of polymers exposed to 5 keV,  $2000 \mu\text{C}/\text{cm}^2$ : (a) control sample at  $100^\circ\text{C}$ , (b) ambient temperature, and (c) heated to  $300^\circ\text{C}$  prior to air exposure.

enhancement of the hardness of polymer based dielectric materials in the interconnect of semiconductor devices.

## **CHAPTER 5: IMPROVEMENT IN THERMALLY DECOMPOSABLE TEMPLATE MATERIAL FOR IC AIR-GAP STRUCTURES**

### **5.1 Background**

As the minimum feature size in integrated circuits (ICs) decreases, the number of metal layers increases and their pitch decreases. This increases the resistance-capacitance (RC) time constant, cross talk, and energy dissipation. Thus, the International Technology Roadmap for Semiconductors (ITRS) calls for a decrease in capacitance by lowering the dielectric constant ( $k$ ) of the metal insulator [1]. Among the low- $k$  options, the incorporation of air, in the form of air-gaps, is the lowest dielectric constant available. Air-gaps are most valuable when integrated as the intra-metal dielectric (IMD) material of local interconnects. Air-gaps have been fabricated by selective plasma deposition where a cavity is intentionally produced during deposition [20,21] or by removing one of the materials in the build-up process once the metal-insulator stack has been fabricated [16,18,19]. The selective removal of a place-holder material can be achieved by thermal decomposition of sacrificial polymer [16,18], or by wet etching [19]. In this study, an improved thermally decomposable sacrificial polymer, used as a placeholder to fabricate air-gaps in the IMD layer, was investigated.

The fabrication process flow for the integration of air-gaps using a thermally decomposable polymer as a place holder is shown in Figure 5.1.1. The sacrificial polymer is spin-coated on the substrate followed by the deposition of SiO<sub>2</sub> which serves as the hard mask and chemical mechanical polishing (CMP) stop-layer. Photo resist is used to transfer the pattern to the SiO<sub>2</sub> and the sacrificial polymer is dry-etched. The next steps include the deposition of metal barrier and Cu seed layer, and the electroplating of Cu. The excess Cu is removed by chemical mechanical polishing (CMP), and the capping layer is deposited on top of Cu lines. After deposition of the encapsulating material, the sacrificial polymer between Cu lines is removed by thermal decomposition resulting in the formation of a cavity (i.e. air-gap). The gaseous byproducts in the cavity between metal conductors permeate through the overcoat material at the polymer decomposition temperature, and the pressure in the cavity comes into equilibrium with the ambient atmosphere. For the better electrical performance, high aspect ratio structures of the interconnects are necessary, making the integrity of sacrificial polymers structures critically important. In addition, the sacrificial polymer must be thermally stable during plasma enhanced chemical vapor deposition (PECVD) of the overcoat material. Residue left from the thermal decomposition of the sacrificial polymer should be minimized as it increases the effective dielectric constant of the air-gap. It is also important that the air-gap

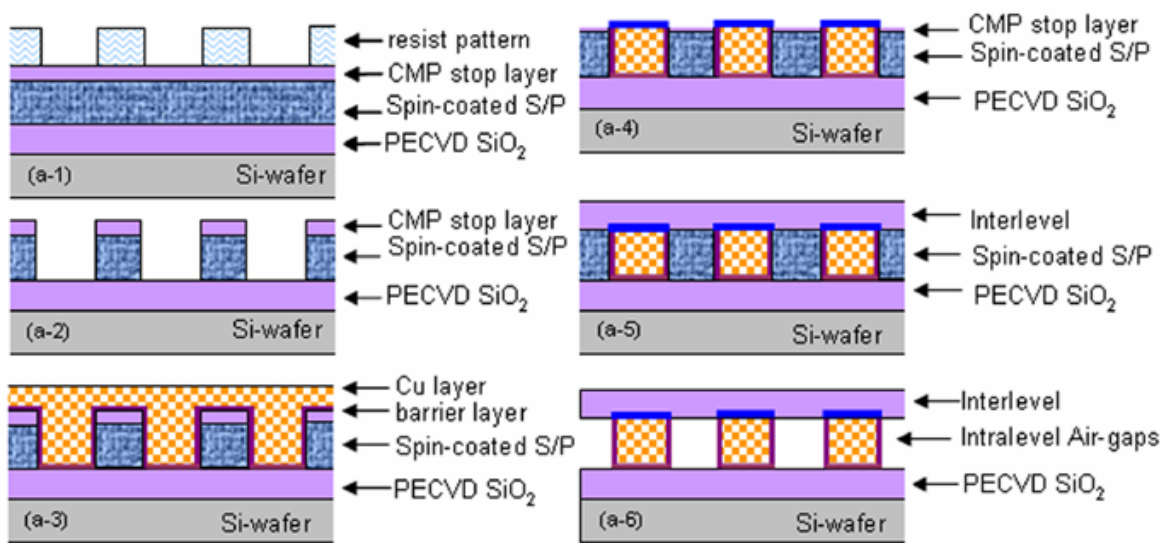


Figure 5.1.1 The schematic diagram of the fabrication process of the single layer Cu/air-gap interconnect structure.



surface is hydrophobic, so that moisture is not absorbed in the cavity. The presence of moisture increases the dielectric constant and may facilitate corrosion of the metal. Therefore, the thermal, mechanical, and chemical properties of sacrificial polymer and its decomposition residue are critical to the performance and reliability of final copper/air-gaps interconnect structures.

Norbornene-based (NB) thermally decomposable polymers (Unity4011<sup>TM</sup>, Promerus LLC.) have been used as sacrificial placeholders to fabricate air-gaps in IMD layers [16,25]. However, in the fabrication processes of air-gaps using sacrificial polymers and dual damascene processes, high aspect ratio lines and anisotropic etching of sacrificial polymer are required, and sacrificial polymer must withstand CMP process as well. Thus, harder sacrificial polymers are of interest for improved process yield. In a previous study [33], the thin films of norbornene-based sacrificial polymer were exposed to electron beam in order to make them harder. However, after exposure of the sacrificial polymer films to electron beam, the thermal properties of the films degraded (see Chapter 4). In this portion of the study, a tetracyclododecene-based (TD) sacrificial polymer (Unity4131<sup>TM</sup>, Promerus LLC), which has a more rigid molecular structure than NB-based sacrificial polymer (Figure 1.3.1) was investigated for use as a sacrificial polymer in the formation of air-gaps.

NB-based and TD-based polymers are both cyclic olefin polymers. It is known that cyclic olefin copolymers have high glass transition temperature, optical clarity, low shrinkage, low moisture absorption, and low birefringence [56,57]. Due to the more rigid molecular structure of the TD-based polymer versus the NB-based polymer, it is expected that the TD-based sacrificial polymer is harder and would lead to improved process repeatability. Hence, the thermal and mechanical properties (hardness) of TD-based sacrificial polymer were compared with those of NB-based sacrificial polymer using dynamic thermal gravimetric analysis (TGA) and nanoindentation. In addition, in order to investigate the effect of the hardness of the polymers on the process reliability, 50 nm lines of both kinds of polymer were fabricated using electron beam lithography and reactive ion etching (RIE). The linearity of the lines as well as the chemical properties of the residue was evaluated.

## **5.2 Experimental**

### **5.2.1 Preparation of thin films and decomposition residues of sacrificial polymers**

Both TD and NB-based sacrificial polymers were provided by Promerus LLC (Brecksville, OH). For the thin film samples, sacrificial polymers were spin-coated on the Si-wafer and soft-baked at 110°C for 5 min on the hot-plate. After the soft-

bake step, the polymer films were hard-baked at 300 °C for 1 hr in the furnace to remove the residual solvent and volatile elements. For the analysis of thermal decomposition residues of sacrificial polymers, hard-baked thin films were thermally decomposed in the furnace at 450°C for 2 hr with the ramping of 2°C/min. Before increasing the temperature, the furnace was purged with nitrogen gas of 4 L/min for 30 min to remove the residual oxygen, and during the heating cycle, the furnace was purged with nitrogen gas of 2 L/min was purged. In the experiment to determine the effect of purging gas on the thickness of decomposition residues, the three different purging gas conditions were considered: Condition A (2 L/min N<sub>2</sub>, normal purging condition); Condition B (a mixture of 1.5 L/min N<sub>2</sub> and 0.5 L/min H<sub>2</sub>, adding hydrogen); and Condition C (4 L/min N<sub>2</sub>, doubling nitrogen flow rate). Oxygen concentrations for each purging condition were measured using Series 3000 Trace Oxygen Analyzer (ALPHA OMEGA Instrument Corp., Cumberland, RI, USA).

### 5.2.2 Nanoindentation

The hardness of thin films of both sacrificial polymers was measured using the nanoindenter TriboIndenter (Hysitron Inc. Minneapolis, MN). The indentation system was enclosed in an acoustic housing and located on an anti-vibration table.

For indentation, the Z-axis resolution was 0.04 nm and a three sided Berkovich tip was used. The average radius of curvature for a Berkovich tip was typically between 100 nm and 200 nm. To exclude the substrate effect, the maximum force was chosen so as to indent less than 10% of the film thickness [44].

### 5.2.3 Fabrication of sacrificial polymer lines and image processing

The effect of the hardness of sacrificial polymers on the process repeatability was evaluated by scanning electron microscopy (SEM) image analysis of the 50 nm lines of sacrificial polymers. In the 2006 updated version of the ITRS [1], metal 1 wiring pitch is anticipated to be 104 nm in 2009 and 90 nm in 2010. In addition, the aspect ratio of metal 1 wire is 1.8 in 2009 and 2010. In order to match this design rule, sacrificial polymer lines with a 50 nm in width and a 50 nm space between the sacrificial polymer lines, and an aspect ratio of the polymer lines of 1.7:1 (H:W) were fabricated. The fabrication schematic for the 50nm lines of sacrificial polymers is shown in Figure 5.2.1. SiO<sub>2</sub> (5 μm thickness) was deposited using PECVD, and the sacrificial polymers were spin-coated. Then the films were soft-baked at 110 °C for 5min and hard-baked at 300 °C for 1 hr in the furnace. After hard-baking, the final thickness of thin films of sacrificial polymer was 85 nm. 30 nm of PECVD SiO<sub>2</sub> were deposited as a hard mask on top of hard-baked thin films of sacrificial polymers.

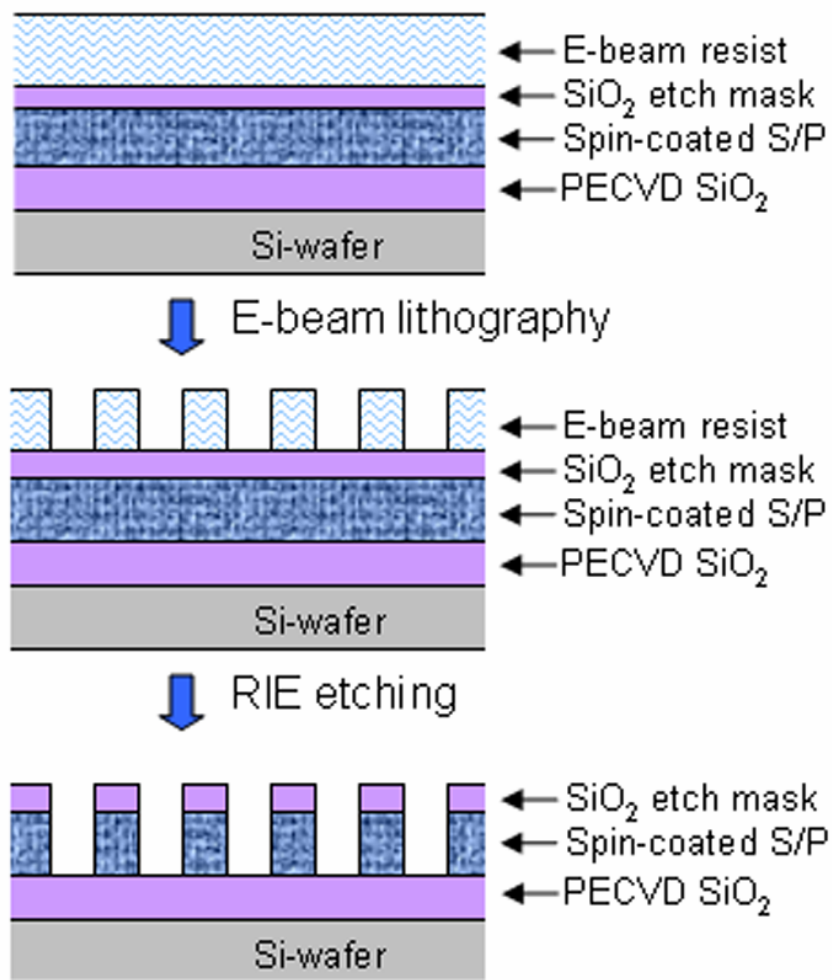


Figure 5.2.1 The fabrication processes of sacrificial polymer lines, 50nm in width

and 85 nm in height.

Polymethyl-metacrylate (PMMA) positive tone electron-beam resist was spin-coated on SiO<sub>2</sub> hard mask, and the thickness of PMMA was 80 nm. PMMA patterns of 50 nm in width and 4 mm in length were fabricated using a JEOL JBX-9300FS electron-beam lithography system. In the electron-beam lithography system, the accelerating voltage of the electron beam was 100 kV, and the spot size was 4 nm. The beam current was 2 nA, and the dose of electron was 450  $\mu\text{C}/\text{cm}^2$ . The developing time for PMMA patterns was 35 sec using MIBK: IPA solution in a 1:1 volume ratio. After developing, PMMA patterns were transferred to the SiO<sub>2</sub> hard mask and the sacrificial polymer layer by reactive ion etching (RIE). In order to etch SiO<sub>2</sub> hard mask, the RIE operating gas was the mixture of 45 sccm CHF<sub>3</sub> and 5 sccm O<sub>2</sub>, and the RF power was 200W. In addition, the RIE operating gas for the sacrificial polymers was 45 sccm O<sub>2</sub> and 0.5 sccm CHF<sub>3</sub>, and two different radio frequency (RF) powers, (i.e. 300W and 400W), were considered in order to evaluate the effect of RF power on the linearity of polymer lines. After making the sacrificial polymer lines, 25 top view SEM pictures were taken for both TD-based and NB-based polymers. The magnification of SEM images was fixed at 20k and the total length of sacrificial polymer lines considered in the evaluation of the linearity of the lines was 3981.25  $\mu\text{m}$  for each sacrificial polymer. To quantify the linearity of the sacrificial polymer lines, SEM pictures were transformed to the binary images. In a binary image, the

number of pixels was  $650 \times 1024$  (row $\times$ column), and the pixel position and width of a sacrificial polymer line at each row were determined using the difference in contrast between the polymer lines (the contrast is 1), and the space (the contrast is 0). Using the information about the pixel position of a polymer line in the binary image, the center line position of a polymer line was calculated. The calculated center line of a polymer line reflected the actual shape of the polymer line. An ideal straight center line was determined by connecting the center of the first row and the last row (650<sup>th</sup> row) in a polymer line. A difference between the calculated center line and ideal straight center line meant the degree of distortion of a polymer line. Thus, the absolute values of the difference were taken for the evaluation of the linearity of polymer lines.

#### 5.2.4 Thermo-gravimetric analysis

The thermal and decomposition properties of the sacrificial polymers were investigated using dynamic thermal gravimetric analysis (TGA) which was performed using a Seiko Instruments Inc. 320 thermogravimetric differential thermal analyzer (Haake Instrument, Paramus, NJ). The sacrificial polymer films were scratched from the wafer surface and placed in a TGA sample pan. In the TGA experiment, before increasing the temperature, the nitrogen gas was purged for 30 min to remove the residual oxygen in the furnace and the film samples were heated

at 2 °C/min from room temperature to 550 °C. The change in sample weight was recorded as a function of time and temperature.

#### 5.2.5 X-ray photoelectron spectroscopy analysis

The thickness and composition of decomposition residues of TD-based sacrificial polymers were investigated using x-ray photoelectron spectroscopy (XPS) and depth profiling. XPS measurements were carried out with a Physical Electronics model 1600 XPS system using an aluminum *Ka* source and toroidal monochromator. All analyses were setup with a 0.8 mm spot size and 45° take-off angle. The base pressure was less than 5E-9 Torr. Ar-ion sputtering was used for depth profiling of the surface composition. Even though depth profiling does not give the accurate absolute thickness, the rough thickness of the thin films can be estimated and compared with each other. The Ar-ion sputtering rate was calibrated by depth profiling of a known thickness of sacrificial polymer layer, and the calibrated etch rate was 2.9 nm/min. It was assumed that the sputter etch rate for a sacrificial polymer layer was the same for decomposition residue, because carbon was the major element in both materials. For the XPS experiment, Al layer of 250 nm was deposited on a Si-wafer using DC sputter and then sacrificial polymers were spin-coated. Spin-coated thin films of sacrificial polymers were soft-baked at 110 °C for 5min on the hot-plate and then



hard-baked at 300 °C for 1 hr in the furnace to remove the residual solvent and volatile elements. For reference purposes, a bare aluminum layer on a Si-wafer without the sacrificial polymer layer was heat treated and depth-profiled. For the decomposed TD-based sacrificial polymer samples, aluminum was used as an end-point indicator of the layer of decomposition residues during the depth profiling.

The elemental mapping images of decomposition residues with different purging gas conditions were taken using time-of-flight secondary ion mass spectroscopy (TOF-SIMS, CAMECA ION-TOF IV), and the mapping area was 70  $\mu\text{m}$   $\times$  70  $\mu\text{m}$ . A Gallium ion gun with the ion energy of 1.5 keV was used.

#### 5.2.6 Contact angle measurement

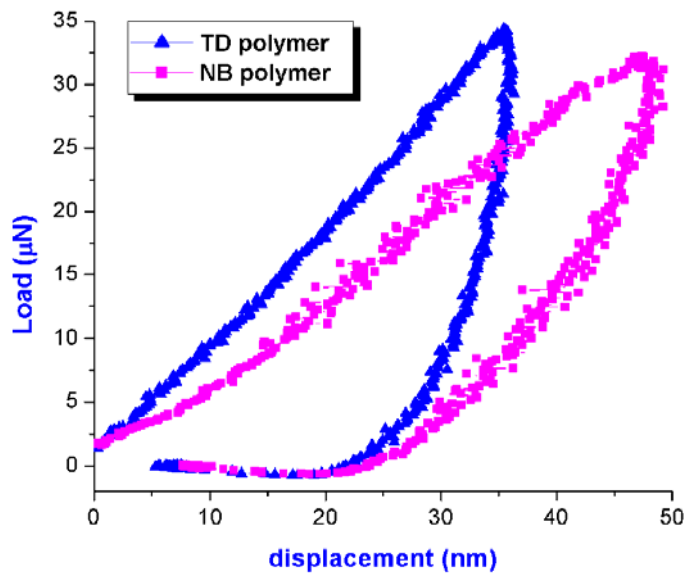
The hydrophobicity of the sacrificial polymer thin films and decomposition residues was evaluated by measuring the contact angle of a water drop on the surface of the samples using a VGA 2500XE (Video Contact Angle System, AST Product Inc., Billerica, MA). The measurements were repeated ten times for each sample and the contact angles were averaged.

### 5.3 Results

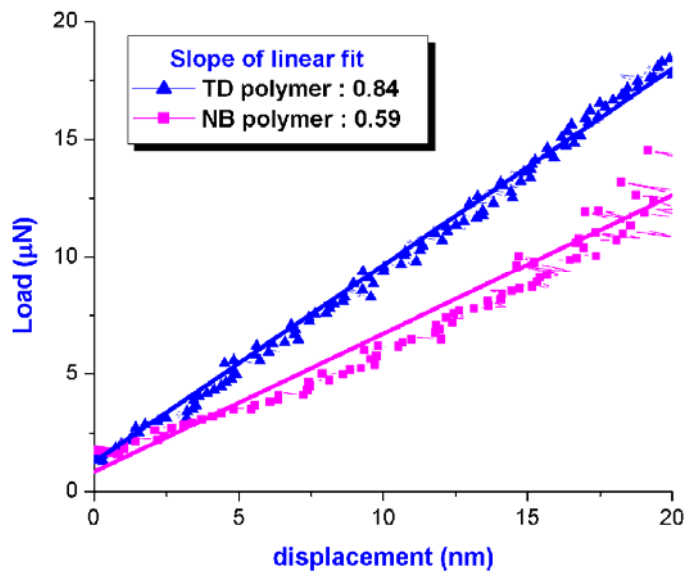
#### 5.3.1 The qualitative comparison of hardness by the nanoindentation

The hardnesses of thin films of TD-based and NB-based polymers were measured using nanoindentation and are compared in Figure 5.3.1. The maximum load was chosen in order to indent less than 10% of the thickness of thin films so that substrate effects were excluded [44]. Figure 5.3.1-(a) is the full range of the indentation and Figure 5.3.1-(b) is the initial part of the indentation force deflection curve. In Figure 5.3.1-(a), at the same load, the NB-based sacrificial polymer was more deeply indented than the TD-based polymer. For instance, at the load of 20  $\mu\text{N}$ , the indentation depths of TD-based and NB-based sacrificial polymers were 21.6 nm and 29.5 nm, respectively. In addition, the hardness of the polymers can be qualitatively compared using the slope of the initial part of the indentation curve. In Figure 5.3.1-(b), the slopes of the initial indentation of TD-based and NB-based polymer were 0.84 and 0.59, respectively. Smaller indentation depth and larger slope of the TD-based sacrificial polymer compared with the NB-based sacrificial polymer indicate that the TD-based sacrificial polymer is harder than NB-based sacrificial polymer. For the quantitative analysis, the calculation procedures developed by Oliver and Pharr [53,58] were used to calculate the hardness. The contact stiffness was calculated by fitting the unloading data between 20% and 95% to the power-law relationship in Equation (5.1) along with Equation (5.2).

$$P_I = \alpha (h - h_f)^m \quad (5.1)$$



(a) The full range of the indentation



(b) The initial part of the indentation

Figure 5.3.1 The load-displacement curves of thin films of TD-based and NB-based sacrificial polymers using a nanoindenter.

$$S = \frac{dP_I}{dh} \quad (5.2)$$

where  $P$  is the indentation load ( $\mu\text{N}$ ),  $h$  is the indenter displacement (nm),  $h_f$  is the final indentation depth (nm),  $\alpha$  and  $m$  are fitting parameters, and  $S$  is the contact stiffness ( $\mu\text{N}/\text{nm}$ ). Then, the contact stiffness was used to calculate the hardness ( $H$ ) by means of Equation 5.3 and 5.4.

$$h_c = h_{\max} - 0.75 \frac{P_{\max}}{S} \quad (5.3)$$

$$H = \frac{P_{\max}}{A(h_c)} \quad (5.4)$$

Where  $h_c$  is the contact depth (nm),  $h_{\max}$  is the maximum indentation depth (nm),  $P_{\max}$  is the maximum load ( $\mu\text{N}$ ), and  $A(h_c)$  is the indentation contact area ( $\text{nm}^2$ ), which is a function of depth. For a pyramidal geometry tip (Berkovich), the relationship between the indentation contact area and the contact depth is given by Equation (5.5).

$$A(h_c) = 24.5h_c^2 \quad (5.5)$$

The calculated hardness ( $H$ ), contact stiffness ( $S$ ), and the maximum indentation depth are summarized in Table 5.3.1. The calculated hardnesses of the thin films of TD-based and NB-based polymers were 1.3 GPa and 0.8 GPa, respectively.

Table 5.3.1 The nanoindentation results for thin films of TD-based and NB-based sacrificial polymers.

	TD-based polymer	NB-based polymer
Hardness (GPa)	1.3	0.8
contact stiffness ( $\mu\text{N}/\text{nm}$ )	6.5	2.5
maximum indentation depth (nm)	35.7	49.2

### 5.3.2 The effect of hardness on the process reliability of the sacrificial polymers

The effect of hardness on the process repeatability of TD-based and NB-based sacrificial polymers was investigated by fabricating 50 nm polymer lines and performing image processing for the evaluation of the linearity of the polymer lines. Figure 5.3.2 shows the top view of sacrificial polymer lines, the calculated center line and the ideal straight center line. For the evaluation of the linearity of polymer lines, the absolute values of the difference between the calculated center line and the ideal straight center line were calculated, because the difference corresponds to the degree of distortion of a polymer line. For instance, if a polymer line is straight, the ideal straight center line is the same as the calculated center line, and the absolute difference should be zero. In this way, the linearity of lines for both TD-based and NB-based sacrificial polymers could be quantified, and the average value and

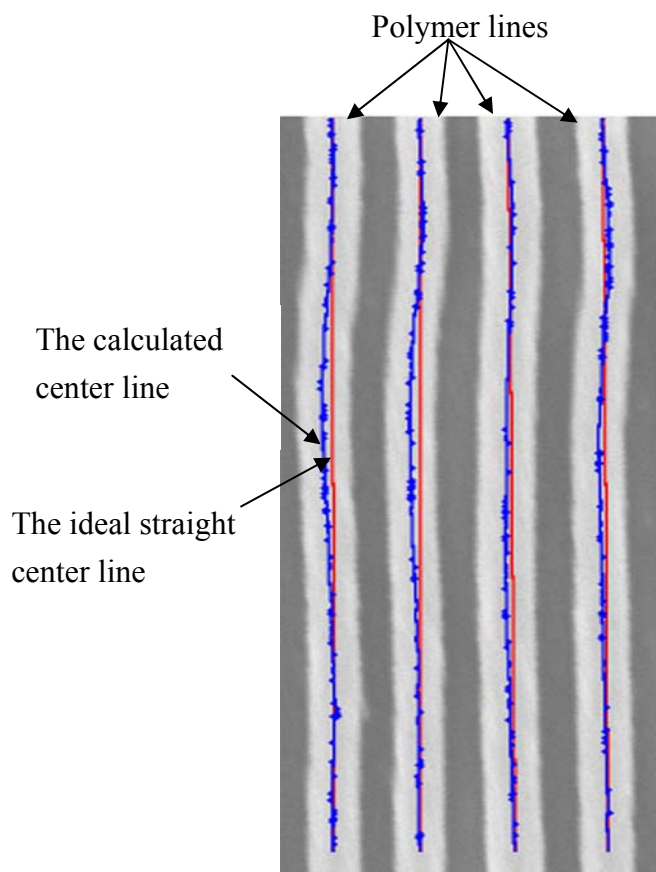
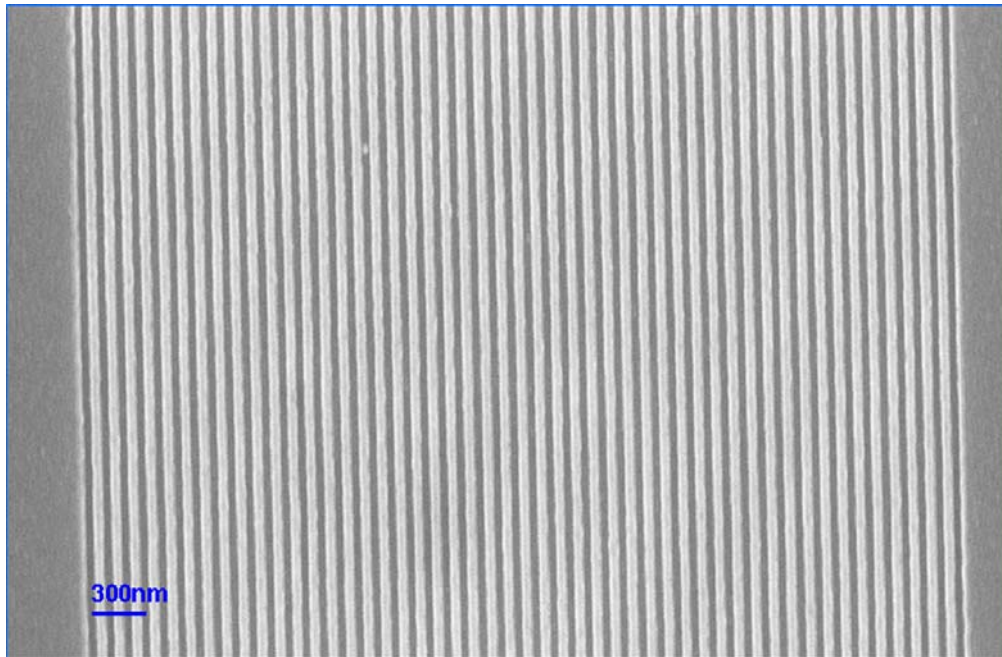


Figure 5.3.2. A sample image to determine the ideal straight center lines and the calculated center lines reflecting the actual shapes of polymer lines, NB-based sacrificial polymer, RF power = 300W.

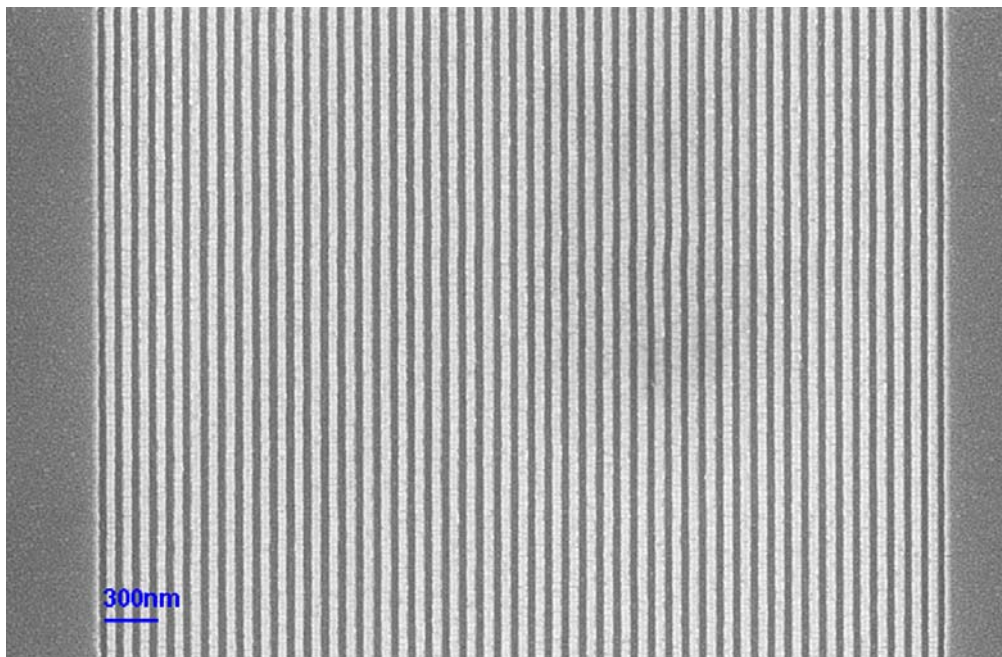
standard deviation of the absolute difference between the calculated center line and ideal straight center line were calculated.

The patterns of SiO<sub>2</sub> hard mask formed by RIE above the TD-based and NB-based polymer layers are shown in Figure 5.3.3. Two different RIE power levels (300 W and 400 W) were used to transfer the SiO<sub>2</sub> patterns to the TD-based and NB-based polymers, as shown in Figure 5.3.4. Two different magnifications of SEM images for each polymer are shown in Figure 5.3.4 in order to show the difference of the line shapes between two polymers. On the right side of Figure 5.3.4, a higher magnification SEM image shows that the NB-based polymer lines were not as straight as the TD-based polymer lines. In the dual damascene processes, anisotropic polymer etch profiles with high aspect ratio are critical. Deformation of the polymer would result in distortion of the metal line. At higher RF power, the softer polymer distorts due to the temperature rise during etching as shown in Figure 5.3.4-(b).

In order to quantify the linearity of each polymer line, 25 plan view SEM images were taken and processed for each polymer. The average distortion of the lines in a pixel (5 nm × 5 nm) and the standard deviation were summarized in Table 5.3.2. At 300 W RF power, the average distortion of 50 nm TD and NB lines was 1.6 nm and 4.0 nm, respectively. At 400 W RF power, the distortion was 1.6 nm and 3.4 nm for TD and NB lines, respectively. Overall, from the nanoindentation and



(a) SiO<sub>2</sub> patterns on top of TD-based polymer layer

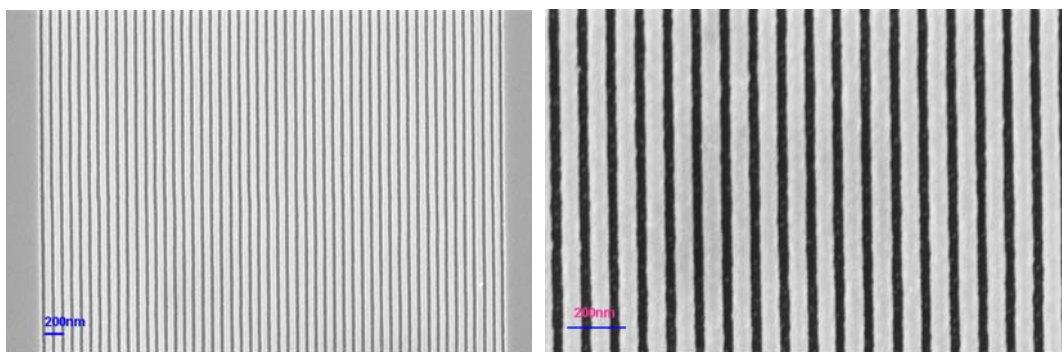


(b) SiO<sub>2</sub> patterns on top of NB-based polymer layer

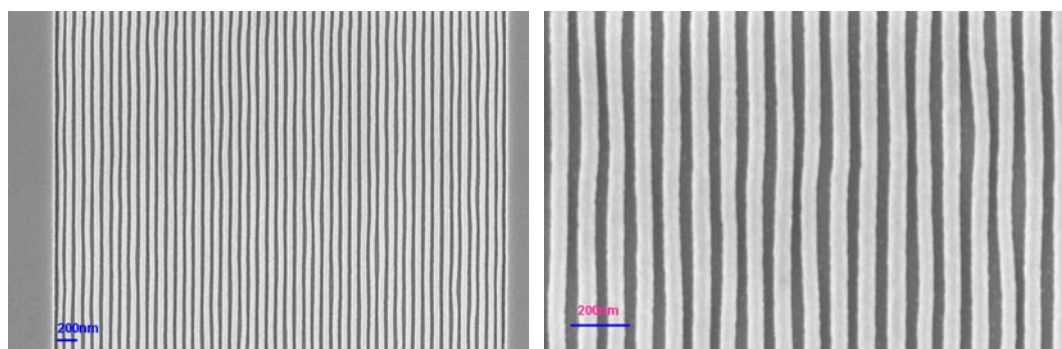
Figure 5.3.3. Top view scanning electron microscopic images of the patterns of SiO<sub>2</sub>

hard mask on top of hard-baked sacrificial polymer layers.





(a) TD-based sacrificial polymer



(b) NB-based sacrificial polymer

Figure 5.3.4. Top view scanning electron microscopic images of the lines of TD-based and NB-based sacrificial polymers, RF power = 400 W.

Table 5.3.2. The summary of SEM image processing for the evaluation of the linearity of TD-based and NB-based sacrificial polymer lines.

	NB polymer, RF=300W	TD polymer, RF=300W	NB polymer, RF=400W	TD polymer, RF=400W
average distortion per one pixel (5nm×5nm)	4.0 nm	1.6 nm	3.4 nm	1.6 nm
Standard deviation	3.9 nm	2.4 nm	3.5 nm	2.4 nm

process reliability study, it could be concluded that the harder TD-based sacrificial polymer has better process reliable than the softer NB-based sacrificial polymer.

### 5.3.3 Thermal properties of sacrificial polymer thin films

Dynamic TGA analysis for the TD and NB polymers is shown in Figure 5.3.5.

TGA spectrum of TD-based polymer is essentially the same as that for the NB polymer. Both TD-based and NB-based polymers were thermally stable up to 300°C (e.g., the temperatures for 5 weight % loss were 353°C for TD-based polymer and 357°C for NB-based polymer). The temperature range for weight loss between 5% loss and 95% was from 353°C to 445°C for TD and from 357°C to 441°C for NB. The decomposition residue at 550°C for TD and NB were 0.33 weight % and 0.70 weight %, respectively. From the dynamic TGA analysis, it was concluded that TD-based material has similar thermal properties to NB.

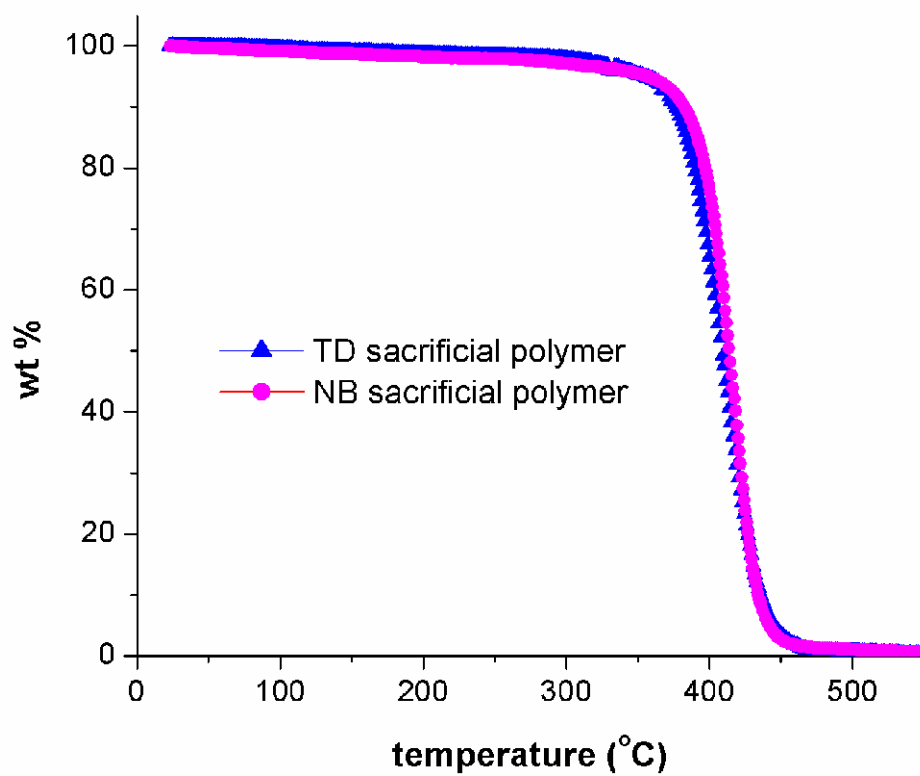
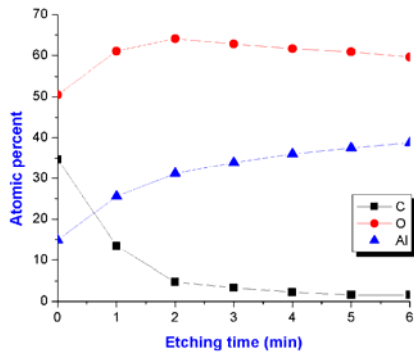


Figure 5.3.5. Dynamic TGA of TD-based and NB-based sacrificial polymers.

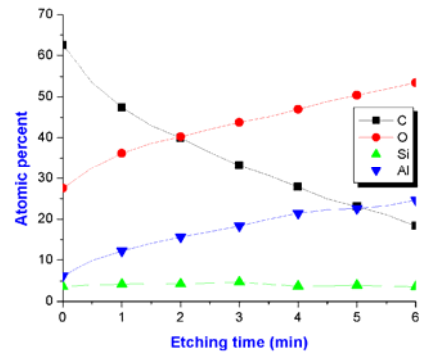
#### 5.3.4 Characterization of decomposition residues of sacrificial polymers

The dynamic TGA analysis shows that the amount of residue after decomposition was insignificant. For comparison, XPS depth profiling using Ar-ion gun was used to evaluate the thickness and composition of the decomposition products. The XPS depth profiling to the decomposition residues was performed after decomposition of a 300 nm thick film of TD-based polymer when the chamber was purged to different purity levels and summarized in Figure 5.3.6.

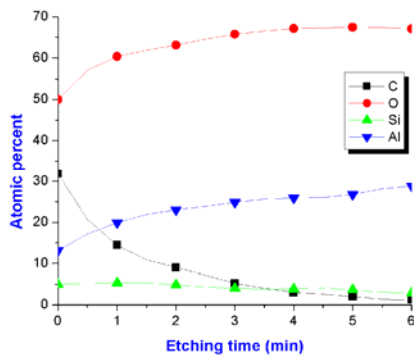
Figure 5.3.6-(a) is the depth profiling of a bare Al layer on a silicon wafer which experienced the same heating profile as decomposition of TD-based polymer. In the depth profiles, the crossover between carbon and aluminum elements represented the interface between the residue and substrate onto which the polymer was deposited. In case of bare Al, the detected carbon layer was formed by atmospheric carbon, and the crossover occurred at 0.7 min etching time. In case of TD decomposition residues with purging condition A, condition B and condition C, the crossover points were 5 min, 0.75 min, and 1 min, respectively. The residue was similar to atmospheric carbon thicknesses except for the case of the purging condition A. According to the previous studies [33,55], a higher oxygen content results in thicker residue films as observed here. The measured oxygen content with the purging condition A was 55 ppm, and it decreased to 19.6 ppm when hydrogen



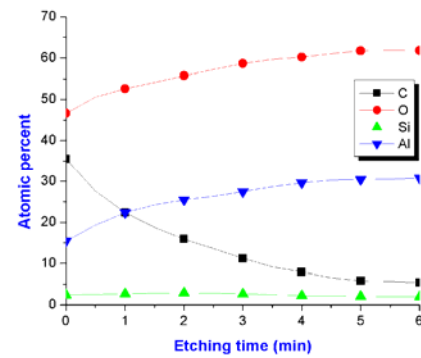
(a) heat treated bare Al



(b) purging condition A



(c) purging condition B



(d) purging condition C

Figure 5.3.6. XPS Depth profiling of the decomposition residues of TD-based sacrificial polymer with different purging conditions during the thermal decomposition: (a) bare Al on Si-wafer, (b) purging condition A, (c) purging condition B, (d) purging condition C.

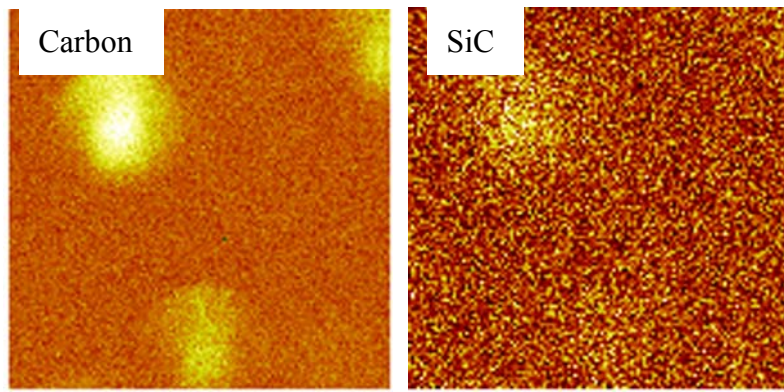
was added in the purging gas (condition B). In addition, the estimated oxygen concentration of purging condition C was 21.7 ppm. Hydrogen acts as a reducing agent and decreases the oxygen concentration in the furnace, resulting in the thinner residue films. In addition, an increase of nitrogen flow rate from the purging condition A to the condition C decreases the oxygen concentration reducing amount of residues.

The measured sputter etch rate of sacrificial polymer was 2.9 nm/min. The sputter etch rate of an element is determined by sputtering yield which is the mean number of atoms removed in any state per incident particle [59,60]. Furthermore, the sputtering yield depends on the energy and the mass of the incoming projectiles and the target atoms, and the angle of incidence of the projectiles. With the given energy and angle of the incident Ar-ion beam, the sputtering yield depends on the mass ratio of the target atoms to the incident ion beam. The major element in the sacrificial polymer is carbon, while the major elements in the decomposition residues and contaminated layer are carbon and oxygen. The mass ratios of carbon and oxygen to the incident projectile (argon) are 0.3 and 0.4, respectively, and are close to each other compared to that of aluminum or silicon, indicating that the sputtering yield and etch rate of carbon are similar to those of oxygen. Therefore, it could be assumed that the sputter etch rate of the decomposition residues and

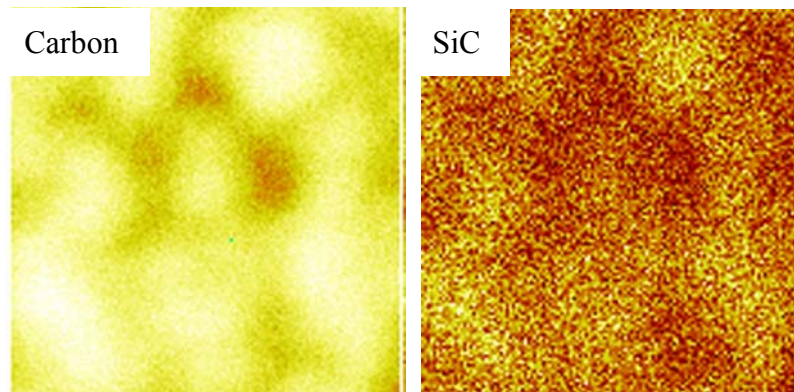
contaminated layer are the same as that of the sacrificial polymer. The crossover at 0.7 min etching time of bare Al in the depth profile indicates that the estimated thickness of carbon layer contaminated from the atmosphere was 2.0 nm.

Based on an etch rate of 2.9 nm/min using known thickness of sacrificial polymer as a calibration standard, the estimated thickness of residues was 14.5 nm for purging condition A, 2.1 nm for purging condition B, and 2.9 nm for purging condition C. In the case of purging condition A, even though the estimated thickness of residue was 14.5 nm, Al was detected at the zero etching time (Figure 5.3.6-(b)), indicating the residue was not homogeneous layer. This was confirmed by obtaining SIMS elemental maps of the decomposition residues as shown in Figure 5.3.7. The carbon and Si elemental images are a due to polymer residues. The silicon was part of the silyl ether side group in the polymer, used for adhesion.

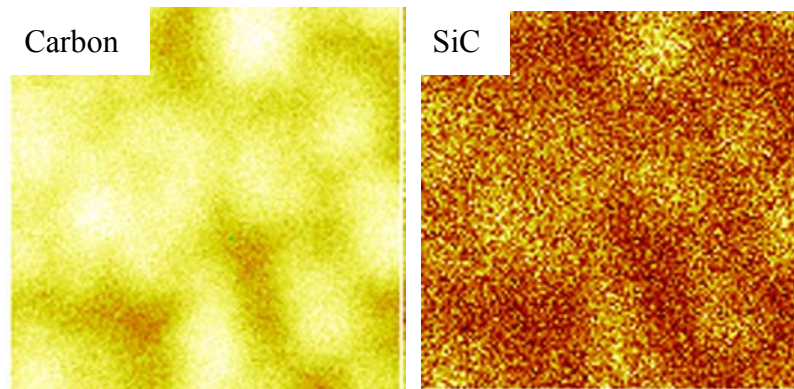
The atomic compositions of TD thin films and decomposition residues are summarized in Table 5.3.3 along with the atomic composition after 3 min Ar-ion sputter etching. The TD polymer was hard-baked at 300°C for 1 hour. On the bare Al, the carbon was resulted from contamination from the atmosphere. The residual oxygen and silicon were from the silyl ether adhesion groups on the polymer. After 3 min Ar-ion sputter etching, the carbon contents of the residues were 5.3 at.% and 11.2 at.% for purging conditions B and C, respectively. They were comparable to



(a) purging condition A



(b) purging condition B



(c) purging condition C

Figure 5.3.7. TOF-SIMS carbon and SiC elemental mapping images of decomposition residues of TD-based sacrificial polymer: (a) purging condition A, (b) purging condition B, (c) purging condition C.



Table 5.3.3. The atomic composition of thin films and decomposition residues of TD-based sacrificial polymer.

		Carbon	Oxygen	Silicon	Aluminum
bare Al	as-received	34.7	50.5		14.8
	after 3 min etching	3.4	62.8		33.9
Hard-baked thin films of TD polymer	as-received	95.5	3.9	0.7	
	after 3 min etching	94.6	4.9	0.5	
Decomposed TD, purging condition A	as-received	62.5	27.5	3.7	6.3
	after 3 min etching	33.2	43.8	4.8	18.3
Decomposed TD, purging condition B	as-received	31.8	50.0	5.1	13.1
	after 3 min etching	5.3	65.8	4.1	24.9
Decomposed TD, Purging condition C	as-received	35.5	46.7	2.4	15.4
	after 3 min etching	11.2	58.7	2.7	27.4

the carbon content of bare Al (3.4 at.%) after 3 min Ar-ion sputter etching, indicating a thin residue layer. However, the carbon content in case of purging condition A was 33.2 at.%, indicating a thicker residue layer.

### 5.3.5 Hydrophobicity of the surface of thin films and decomposition residues

The hydrophobicity of the residue surface after decomposition is critical because moisture would increase the dielectric constant and could lead to corrosion. The hydrophobicity was investigated by measuring the contact angle of a water drop as shown in Table 5.3.4. The polymer samples were hard-baked at 300°C for 1 hr and thermally decomposed under different purging conditions. The contact angles for the polymer films and their residues were larger than those of the base aluminum

Table 5.3.4. The summary of the contact angle measurements of the polymer films itself and decomposition residues of TD-based and NB-based sacrificial polymers with the variation of the purging gases and the initial thickness of polymer thin films.

	hard baked thin films	Decomposed, purging condition A	Decomposed, purging condition B	Decomposed, purging condition C
bare Al	71.6	39.2	54.2	46.0
<b>TD polymer (300 nm)</b>	95.7	91.9	87.5	85.2
<b>TD polymer (1.2 μm)</b>	95.1	85.0	87.8	86.9
<b>NB polymer (400nm)</b>	100.8	83.8	84.4	
<b>NB polymer (4.5μm)</b>	98.5	99.8	89.3	

films, as shown in Table 5.3.4. Two polymer thicknesses were used in the experiments in order to investigate the effect of the initial thickness on the hydrophobicity of the surface after decomposition. As shown in Table 5.3.4, there was no clear difference in contact angle between the thin and thick films for both TD-based and NB-based polymers. In addition, the different purging gas conditions had no effect on the hydrophobicity of the residue surfaces. The large carbon content in the residue resulted in a hydrophobic surface with the large contact angle.

## 5.4 Conclusion

Nanoindentation experiments have shown that the TD-based polymer was harder than the NB-based polymer. The effect of hardness on the process repeatability was investigated by fabricating 50 nm polymer lines and performing image processing for evaluation of linearity of both polymer lines. From this quantitative analysis, it was shown that the harder TD polymer had better process repeatability than the softer NB polymer. From the dynamic TGA analysis, the TD-based polymer had similar thermal properties to the NB polymer. Both TD and NB polymers were thermally stable up to 300°C, and the decomposition residues were less than 1% of the initial polymer thickness. The surfaces of polymer films and their residues were hydrophobic.

## **CHAPTER 6: FABRICATION AND CHARACTERIZATION OF ULTRA LOW-K CU/AIR-GAP AND EXTENDED CU/AIR-GAP STRUCTURES USING HIGH MODULUS SACRIFICIAL POLYMER**

### **6.1 Background**

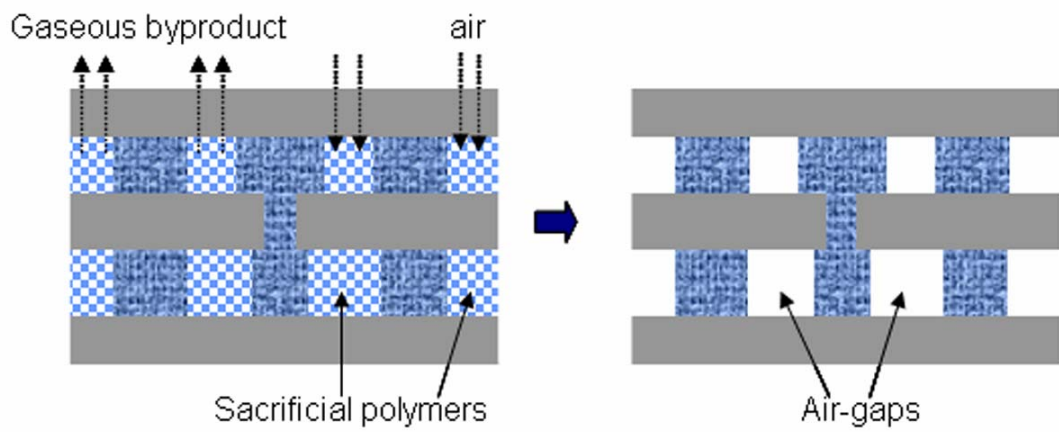
The performance of semiconductor devices has improved due to scaling of transistor parameters [1]. However, with the shrinkage of the minimum feature size, the interconnect structure has become multi-layered, complex and smaller in size. Thus, the performance of interconnect has deteriorated and the interconnect challenges such as resistance-capacitance (RC) delay, crosstalk noise and power dissipation have become the barriers to the progress of the performance of semiconductor devices.

Integrated circuit (IC) interconnects are composed of multi-level metal lines to transport signals and power, and dielectric materials to insulate adjacent metal lines. The performance of the interconnect is determined by the properties of the metal, dielectric materials, and their geometry. The interconnect geometry is a function of the design rules. The dual damascene Cu metallization process, as developed by IBM in 1997 [8] has clear advantages over Al metallization due to the advantages of lower resistance, higher allowed current density, and the increased scalability [8-10] of the process. Numerous low dielectric constant (low-k) materials, including

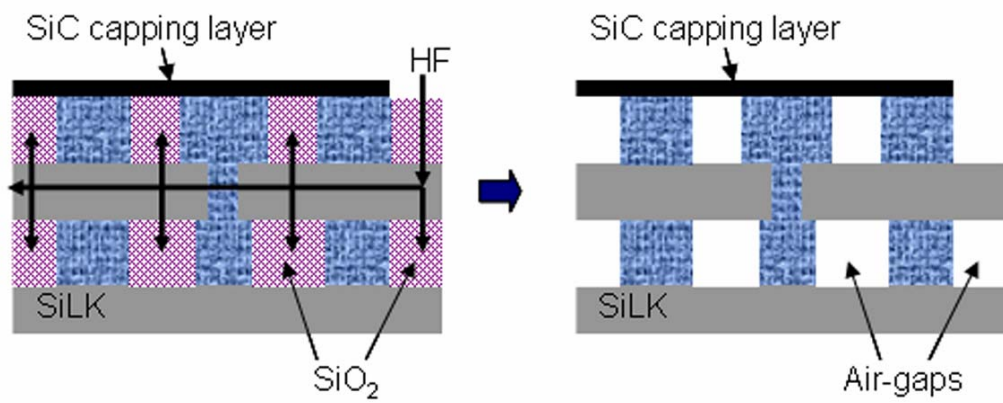
fluorine doped silicon dioxide (F-SiO<sub>2</sub>), polymers, spin-on-glasses, foams [13], plasma enhanced chemical vapor deposition (PECVD) SiOC [14], PECVD SiCOH [15], and air-gaps [16-21] have been developed for decreasing the interconnect capacitance and integration into a Damascene process flow. The incorporation of air, in the form of air-gaps, is the lowest dielectric constant available.

The concept of air-gap integration as an intra-metal dielectric material was first introduced by R.H. Havemann et al. (Texas Instrument Inc.), in 1995 [26] using the removal of a spin-coated disposable solid material (e.g. photoresist) in between metal lines. The metal lines were formed by wet etching and the disposable solid material was spin coated. A porous oxide layer was then deposited, and the disposable solid material was removed by wet etching or oxidation (using oxygen from the air) through the porous material, resulting in the formation of an air-gap between the metal lines, one layer at a time. The metallization-first process is generally not preferred over the dielectric-first process because it is easier to fill high aspect ratio voids (height-to-width) with metal than to fill voids with dielectric. Thus, numerous methods to integrate air-gaps into a dual damascene process were developed and are categorized into three approaches, as shown in Figure 6.1.1 and Table 6.1.1.

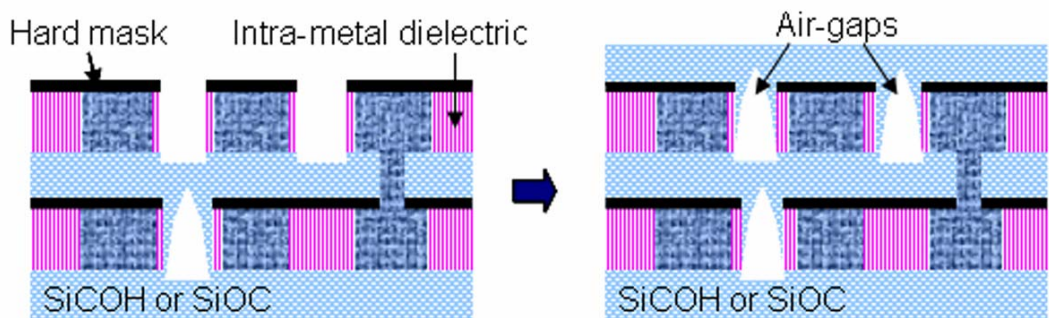
The first approach is to use a thermally decomposable sacrificial polymer as a



(a) Thermal decomposition of the sacrificial polymers [16-18]



(b) Wet etching of the  $\text{SiO}_2$  intra-metal dielectric [19]



(c) Etch back of the intra-metal dielectric and non-conformal deposition of the inter-layer dielectric [20,21]

Figure 6.1.1 The three different integration approaches of dual damascene air-gaps.

Table 6.1.1 The summary of the different approaches for the integration of air-gaps in terms of the number of lithography and additional process steps compared to the conventional dual damascene process.

Air-gap integration approach	Company	Number of lithography	Number of additional steps compared to dual damascene
Thermal decomposition of sacrificial polymer	GeorgiaTech [16,17]	2	3
	NXP Semiconductors and DOW [18]	2	0
Removal of sacrificial materials by wet etching	STMicroelectronics, CEA, LTM/CNRS, NXP Semiconductors [19]	3	4
Non-conformal deposition of inter-layer dielectric	Matsushita, Panasonic, Renesas Tech. [20]	3	4~6
	IBM [21]	3	8

temporary placeholder in between metal lines as shown in Figure 6.1.1a. After finishing a chemical mechanical polishing (CMP) step of the dual damascene process, a second inter-layer dielectric is deposited which encapsulates the temporary trench patterns of the sacrificial material. Then, the sacrificial polymer is thermally decomposed and the gaseous byproducts diffuse out through the second inter-level dielectric layer, while air diffuses in, forming an air-cavity. Two lithography steps are needed for via and trench patterning, and three additional steps (spin-coating, etching, and decomposition of sacrificial polymers) were used in comparison to the traditional dual damascene processes [16,17]. Daamen et al. used a spin-on thermally degradable polymer and an embedded via-first dual damascene air-gap process [18]. There are two lithography steps (via and trench patterning) and no additional process steps are needed compared to the dual damascene structure due to the embedded via-first process.

The second approach is the removal of the sacrificial material by wet etching, as disclosed by Gosset et al. [19] and shown in Figure 6.1.1b. After finishing a CMP step of a dual damascene process and deposition of a SiC capping layer, an additional lithography step is used to open an etching solution pathway in the SiC capping layer. A sacrificial layer of well-known SiO<sub>2</sub> between the Cu lines is dissolved using hydrofluoric acid introduced through the etching solution pathway,



leaving air-cavities in the intra-metal dielectric regions. The organic dielectric SiLK (Dow Chemical) as an inter-layer dielectric is not dissolved in the hydrofluoric acid, leaving it intact as the overcoat dielectric. Three lithography steps are needed for via, trench, and SiC etching (creating the hydrofluoric acid pathway). Four additional process steps are needed compared to the dual damascene process, including lithography and etching of the SiC capping layer to open the hydrofluoric acid pathway.

The formation of air-gaps during non-conformal CVD deposition of the inter-layer dielectric material is the third approach [20,21]. After finishing a CMP step of a dual damascene process and deposition of a hard mask, an additional lithography step is used to etch back the intra-metal dielectric material in a desired region where air-gaps are formed. The air-cavities are created during the non-conformal CVD deposition of the inter-level dielectric which pinches off the top portion of the dielectric layer [34,36] as shown in Figure 6.1.1c. Three lithography steps are needed for via, trench, and selective etch-back of the intra-metal dielectric. Four additional process steps are needed compared to the dual damascene process, including selective etching of the intra-metal dielectric and chemical mechanical polishing of the upper inter-level dielectric layer. Recently, a manufacturing-worthy dual damascene air-gap processes using non-conformal deposition of the SiCOH

inter-layer dielectric material has been disclosed by IBM [21]. In this approach, the SiCOH dielectric was used as the intra-metal and inter-layer dielectric materials in the dual damascene process to fully take the advantages of low dielectric constant of SiCOH. Following the dual damascene process, an additional lithography step was used to etch back the SiCOH intra-metal dielectric material in order to incorporate air-cavities in the desired areas. After the etch-back of the SiCOH intra-metal dielectric, SiCOH as a top inter-layer dielectric is non-conformally deposited, forming air-gaps in-between the metal lines. In this approach, three lithography steps are used and eight additional process steps are needed compared to the dual damascene process. The additional process steps include a lithography for the etch back of SiCOH dielectric in between the Cu lines and hard mask in the desired interconnect regions, and the deposition and CMP step of the top SiCOH inter-layer dielectric.

In this study, a single layer Cu/air-gap structure using a thermally decomposable sacrificial polymer placeholder is investigated. The study also includes extending the air-gap into the inter-layer dielectric region, further lowering the effective dielectric constant. The effect of moisture uptake on the Cu/air-gap structure is also studied.

## **6.2 Fabrication of the single layer Cu/air-gaps and extended Cu/air-gaps**

### **interconnect structures using the lift-off metallization technique**

#### 6.2.1 Fabrication of Cu/air-gaps interconnect structures

Air-gap structures and structures extending the air cavity into the inter-layer dielectric were fabricated, as shown in Figure 6.2.1 and 6.2.2. The purpose of the fabrication is to demonstrate the ability to fabricate the air-gaps and extended air-gaps using the high modulus tetracyclododecene (TD)-based sacrificial polymer and experimentally verify the advantage of integration of air-gap and extended air-gap into an intra-metal dielectric region on the interconnect capacitance. Thus, a lift-off Cu metallization process was used in all the processes. The patterns of polymethylmetacrylate (PMMA) positive tone electron-beam resist were developed using a methyl isobutyl ketone and isopropyl alcohol (IPA), 1:1 volume ratio, followed by an IPA rinse for 1 min. Electron-beam exposures were performed using a JEOL JBX-9300FS electron-beam lithography system. The accelerating voltage of the electron beam was 100 kV and the spot size was 4 nm. The beam current was 2 nA and the electron dose was  $500 \mu\text{C}/\text{cm}^2$ . After developing, the height and width of PMMA patterns were 540 nm and 200 nm, respectively. A 380 nm Cu layer was deposited using a filament evaporator (PVD75, Kurt J. Lesker Company) at a deposition rate of  $2 \text{ \AA}/\text{sec}$ . During removal of the PMMA electron-beam resist in N-

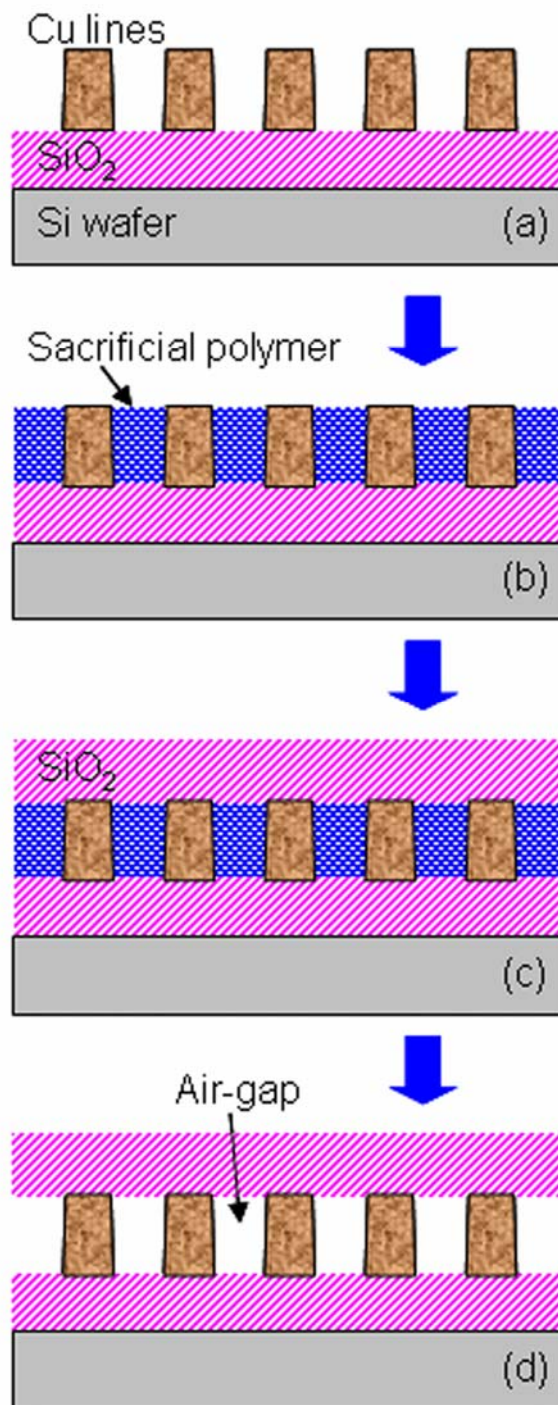


Figure 6.2.1 The fabrication processes flow for Cu/air-gaps interconnect structures using the Cu metallization first process.

methyl-2-pyrrolidone (NMP) at 70°C, the Cu lines on top of PMMA electron-beam resist patterns were also removed, with the Cu lines remaining in-between the PMMA electron-beam resist patterns as shown in Figure 6.2.1a. The Cu lines were annealed at 450 °C for 2 hr in nitrogen atmosphere. The aspect ratio of Cu lines was 1.8:1 (H:W, 380 nm in height and 210 nm in width). The integration of air-gaps with the dual damascene processes will be proposed in the discussion section.

Following Cu metallization, the tetracyclododecene-based sacrificial polymer (TD) was spin-coated and etched to remove the excess material (Figure 6.2.1b). After hard bake of the TD-based sacrificial polymer at 300°C for 1 hr in nitrogen, a PECVD SiO<sub>2</sub> dielectric layer was deposited (Figure 6.2.1c). The sacrificial polymer was thermally decomposed in the furnace resulting in the formation of air-gaps as shown in Figure 6.2.1d. Before starting the heating cycle, nitrogen gas (4 L/min) was used to purge the furnace for 30 min to remove the residual oxygen. During the heating cycle, the nitrogen flow rate was decreased to 2 L/min. During thermal decomposition, the sacrificial polymer was decomposed to form gaseous by-products. The furnace ramp rate was adjusted so that the polymer decomposition rate was 0.5 wt%/min to avoid excess pressure build-up during decomposition [24,31]. Table 6.2.1 shows the temperature profile during the thermal decomposition step. The half-pitch of the Cu/air-gap interconnect was 200 nm and the height of Cu

Table 6.2.1. The temperature profile for the decomposition of sacrificial polymer with 0.5 weight % /min.

	initial temp	final temp	time(min)	ramping rate
step 1	0	300	150	2.0
step 2	300	350	50	1.0
step 3	350	385	205	0.17
step 4	385	395	30	0.33
step 5	395	405	20	0.50
step 6	405	415	13	0.77
step 7	415	430	10	1.50
step 8	430	450	4	5.00
step 9	450	450	120	0.00

metal lines was 380 nm. For the purpose of comparison, PECVD Cu/SiO<sub>2</sub> interconnect structures were also fabricated.

### 6.2.2 Fabrication of extended Cu/air-gaps interconnect structures

The fabrication process for the extended Cu/air-gap structures is shown in Figure 6.2.2. After Cu metallization using the lift-off process (Figure 6.2.2a), the lower SiO<sub>2</sub> layer was etched by reactive ion etching (RIE) to extend air-gaps into the bottom dielectric layer as shown in Figure 6.2.2b. The Cu lines were used as a hard mask and the etched depth of SiO<sub>2</sub> was 100 nm. The TD-based polymer was spin-coated on the Cu lines, and a thin PECVD SiO<sub>2</sub> layer was deposited (Figure 6.2.2c) and used as a hard mask in the following dry etch step. The sacrificial polymer on

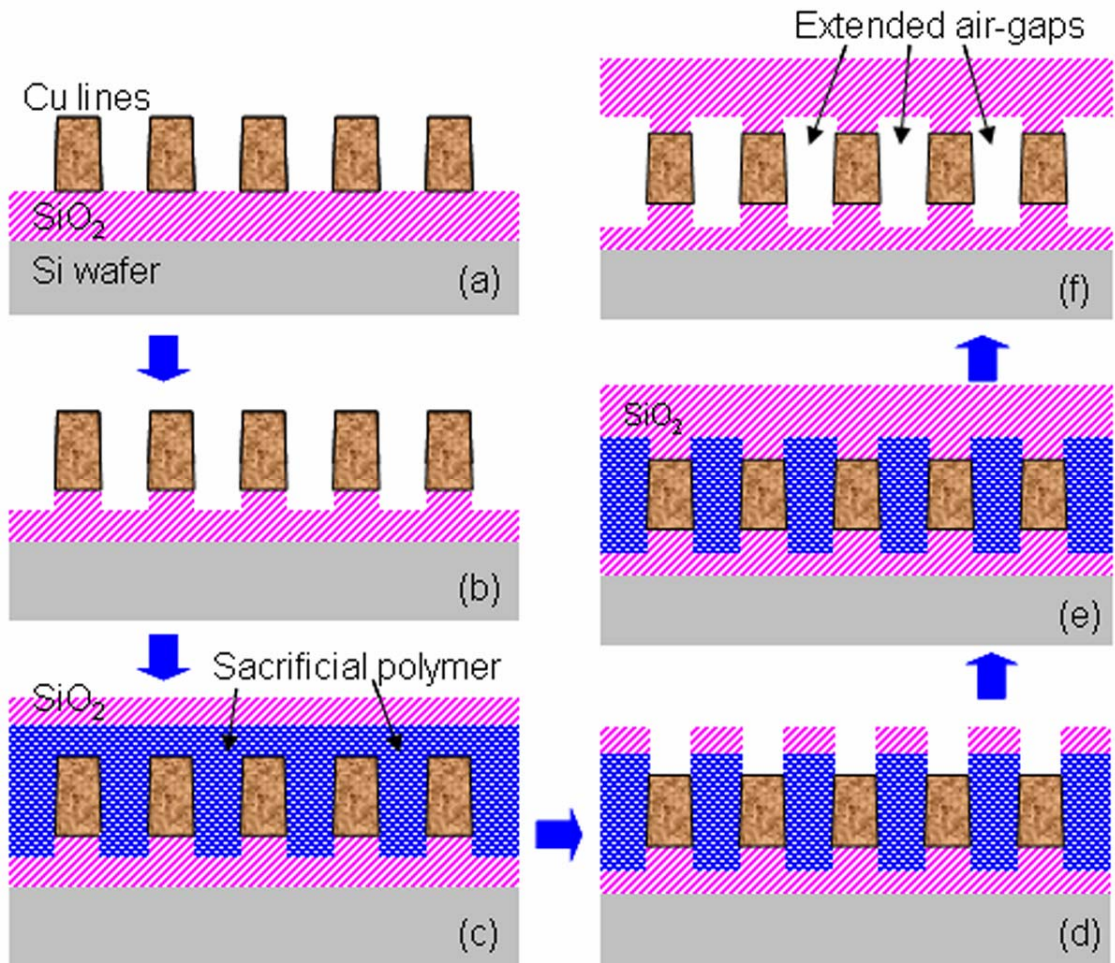


Figure 6.2.2 The fabrication processes flow for extended Cu/air-gaps interconnect structures using the Cu metallization first process.

top of the Cu lines was removed by electron-beam lithography, resulting in the extension of air-gaps into the upper SiO<sub>2</sub> layer as shown in Figure 6.2.2d. The extension of the air-gap into the upper SiO<sub>2</sub> dielectric layer was determined by the thickness of spin-coated sacrificial polymer on top of the Cu lines, which was approximately 80 nm. The next step was the deposition of the upper SiO<sub>2</sub> layer (Figure 6.2.2e) and the TD-based polymer between Cu lines was thermally decomposed as shown in Figure 6.2.2f. The decomposition process conditions were the same as those for the fabrication of Cu/air-gap structures.

## **6.3 Experiments**

### **6.3.1 Capacitance measurement of the comb structure devices**

In the fabrication of Cu/air-gap and extended Cu/air-gap structures, PECVD SiO<sub>2</sub> was used as the inter-layer dielectric. The effective dielectric constant of Cu/air-gap and extended Cu/air-gap structure were evaluated by comparing the measured capacitances to those with SiO<sub>2</sub>. The dielectric constant of PECVD SiO<sub>2</sub> was measured by making parallel plate capacitors. The area of Cu electrodes was 1400 μm × 1400 μm and the thickness of a PECVD SiO<sub>2</sub> dielectric was 1 μm. The calculated capacitance due to the fringing field was small, 0.014% so that the parallel capacitor was considered an ideal parallel capacitor and the relative



dielectric constant of PECVD SiO<sub>2</sub> was calculated by measuring a capacitance of the parallel capacitor and the equation (6.1).

$$C = \epsilon_0 \epsilon_r \cdot \frac{A}{d} \quad (6.1)$$

where  $C$  is the capacitance,  $\epsilon_0$  is the permittivity of free space,  $\epsilon_r$  is the relative dielectric constant,  $A$  is the electrode area, and  $d$  is the distance between two electrodes.

The comb structures of Cu/SiO<sub>2</sub>, Cu/air-gap and extended Cu/air-gap interconnects were fabricated and the capacitances of each interconnect structure were measured using a Keithley 590 CV analyzer and Cascade Microtech Alessi REL-4800 Probe Station at room temperature. The capacitance of the devices was measured at 1 MHz frequency with a voltage sweep from -1 V to 1 V.

### 6.3.2 Moisture uptake of extended Cu/air-gaps interconnect structures

The moisture uptake of the extended Cu/air-gap structures was investigated by changing the relative humidity within the probe station enclosure. In order to stabilize the relative humidity of the atmosphere inside the probe station enclosure and make the moisture uptake of the device steady-state, a comb structure device was exposed to each RH for 1 hr before the capacitance was measured. Hexamethyl disilazane (HMDS) treatment was carried out on a vacuum line to remove moisture

and make the comb structure device hydrophobic. The device was evacuated using a turbo-molecular pump for 1 hr. In addition, a separate vessel which contains HMDS was evacuated to remove the air inside the vessel so that only HMDS gas existed in the head space. After the evacuation for 1 hr, the device was exposed to HMDS vapor for 1 hour.

## **6.4 Electrostatic modeling**

### 6.4.1 Modeling geometry

The integration of air-gaps as the intra-metal dielectric and extension of the air-gap into the top and bottom inter-level dielectric layer was investigated by electrostatic modeling. Figure 6.4.1 shows the geometry modeled using ANSYS. The width and aspect ratio (H:W) of the Cu lines were fixed at 200 nm and 2.0, respectively. The modeled domain of  $10\ \mu\text{m} \times 10\ \mu\text{m}$  accounted for more than 99.5% of the electric fringing field. In the case of extended air-gap, the height of the air-gap was extended by 100 nm into the top and bottom SiO<sub>2</sub> inter-level dielectric layers.

### 6.4.2 Effect of the integration of air-gaps and extended air-gaps on the interconnect capacitance

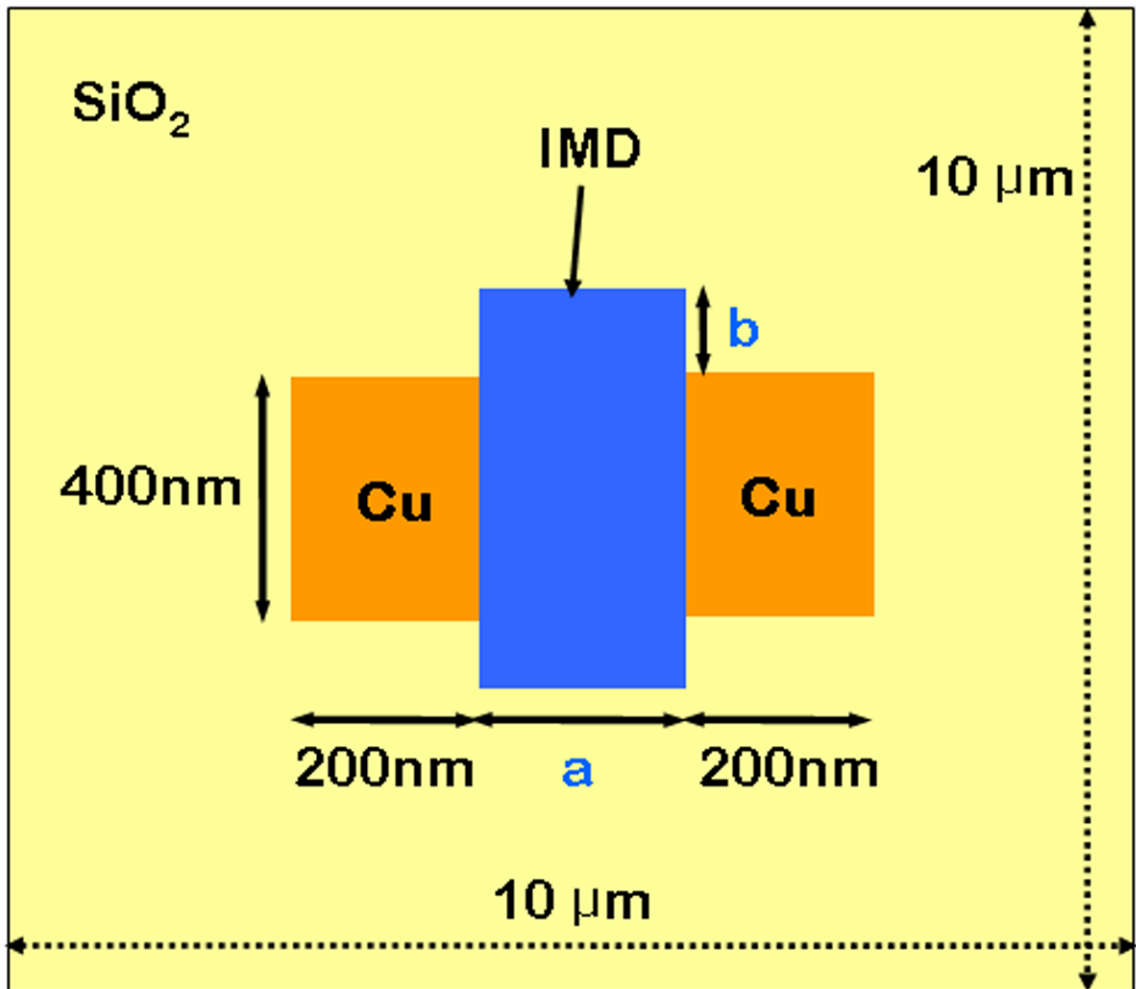
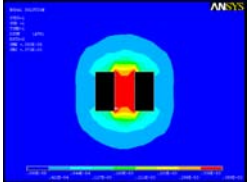
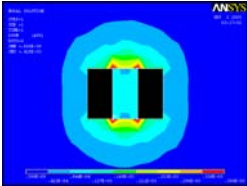
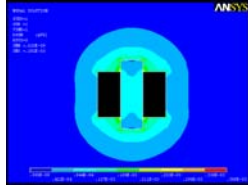


Figure 6.4.1 The modeling geometry of the interconnect.

Table 6.4.1 The summary of the electric flux density, capacitance, and  $k_{eff}$  of

homogeneous Cu/SiO<sub>2</sub>, Cu/air-gaps and extended Cu/air-gaps interconnect.

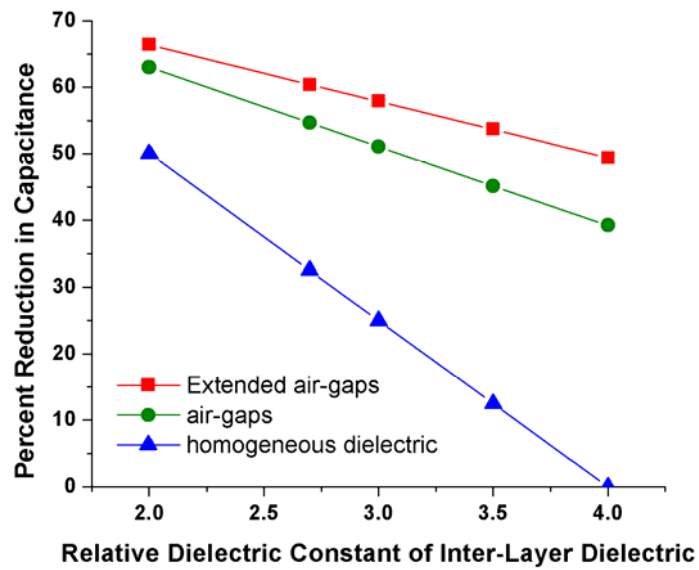
	SiO <sub>2</sub> dielectric	Air-gaps	Extended air-gaps
Electric flux density ( $D$ )			
Capacitance( $C$ )	138.2 pF/m	84.8 pF/m	69.5 pF/m
% reduction in capacitance	0 %	39 %	49 %
Effective $k$ ( $k_{eff}$ )	4.0	2.45	2.01

The contour plots of the electric flux density ( $D$ ), the capacitance per unit length, and  $k_{eff}$  of Cu/SiO<sub>2</sub>, Cu/air-gaps, and extended Cu/air-gaps interconnects are summarized in Table 6.4.1. From the comparison of the electric flux density distribution in the contour plots, it can be observed that the incorporation of an air-gaps decreases the electric flux density in the intra-metal dielectric region between the Cu lines compared to the case where SiO<sub>2</sub> is placed between the copper lines. However, the electric flux density is still high at the corners of the Cu lines due to the fringing field into the inter-layer dielectric. The effective dielectric constant can be decreased by extending the air-gap into the inter-level dielectric layer. This is shown in the extended Cu/air-gaps interconnect structure. The air-gaps and extended

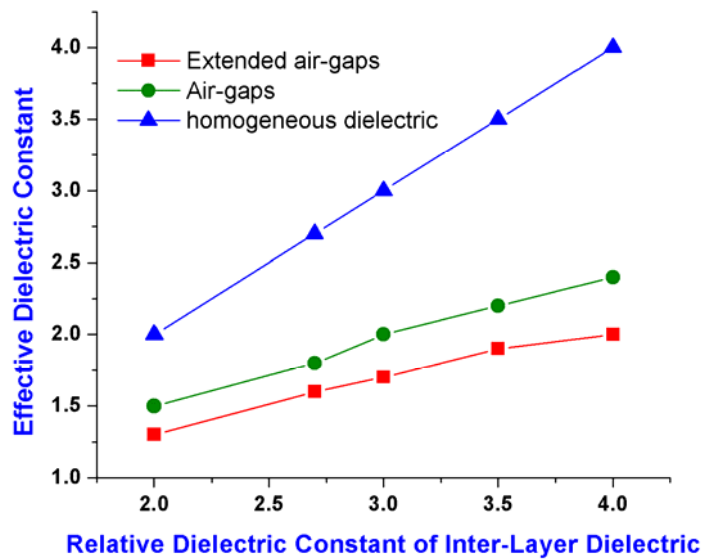
air-gaps lower capacitance by 39% and 49%, respectively, compared to SiO<sub>2</sub>. The  $k_{eff}$  of the air-gap structure was 2.45. Extending the air cavity 100 nm into the inter-layer dielectric lowered  $k_{eff}$  to 2.01.

#### 6.4.3 Effect of the dielectric constant of inter-level dielectric materials on the interconnect capacitance

In Figure 6.4.2, the effect of inter-layer dielectric constant on  $k_{eff}$  (percent reduction) is shown. The geometry for the model was the same as in Figure 6.4.1. The width and aspect ratio of the Cu lines and air-gaps were 200 nm and 2.0, respectively. In the case of an extended air-gap, the height of the air cavity was extended 100 nm into the top and bottom of the inter-layer dielectric. As the dielectric constant of the inter-layer dielectric decreased, the effective dielectric constant of the interconnect structures decreased. For example, if a low-k dielectric were used ( $\epsilon_r= 2.7$ ) instead of SiO<sub>2</sub> ( $\epsilon_r= 4.0$ ), the capacitance decreased 54.7% compared to the SiO<sub>2</sub> case (no air-gap). The effective dielectric constant decreased from 4.0 for SiO<sub>2</sub> to 1.8. In the case of an extended air-gap with a very low inter-layer dielectric ( $\epsilon_r= 2.0$ ), the  $k_{eff}$  was reduced to 1.3 which exceeds the needs of the 22 nm technology node [1].



(a) Percent reduction in capacitance

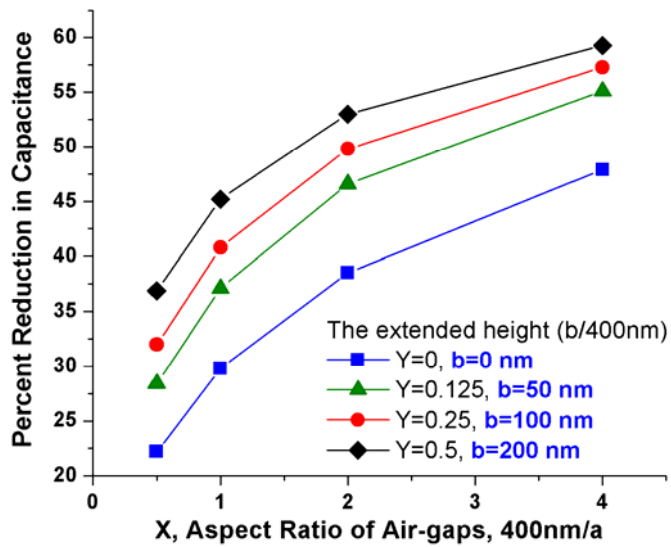


(b) Effective dielectric constant

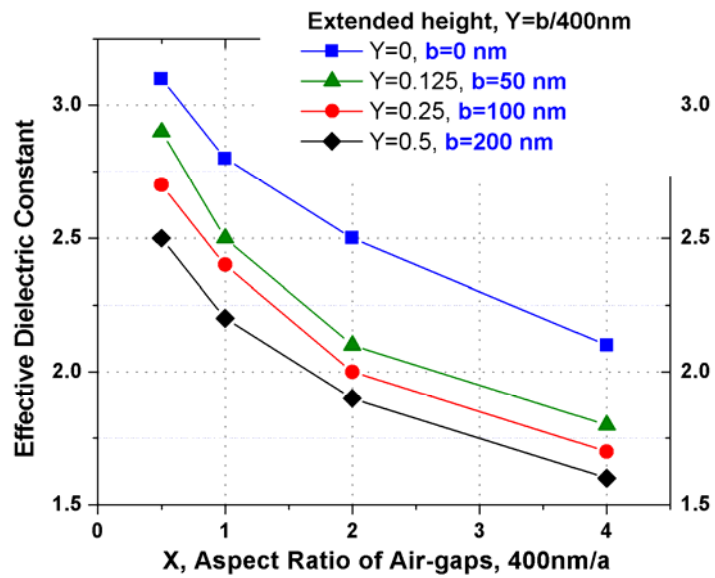
Figure 6.4.2 The effect of dielectric constants of inter-layer dielectric materials on the percent reduction in capacitance and  $k_{eff}$  (a) Percent reduction in capacitance, (b) Effective dielectric constant

#### 6.4.4 Effect of the extended height of air-gaps and the space between metal lines on the interconnect capacitance

The effect of extending the height of the air-gap and the space between metal lines (aspect ratio of the air-gap) on the interconnect capacitance and  $k_{eff}$  were evaluated, as shown in Figure 6.4.3. In Figure 6.4.1, the parameter 'a' is the width of an air-gap and the aspect ratio of dielectric area, X was defined as  $400 \text{ nm}/a$ . As X becomes larger, the space between Cu lines becomes narrower. Parameter 'b' is the extension height of an air-gap into the top and bottom inter-layer dielectric. The ratio of extension height of the air-gap to the height of Cu lines, Y was defined as  $b/400 \text{ nm}$ . That is, Y becomes larger as the air-gap extends further into the inter-layer dielectric. As the space between the copper lines decreases (X becomes larger), the effective dielectric constant decreases, as shown in Figures 6.4.3b. This is because a decrease in the space between the Cu metal lines increases the intensity of electric field ( $E$ ) and electric flux density ( $D$ ). However, the electric flux density ( $D$ ) is a function of the dielectric constant of an insulator and can be reduced by locating air-cavities in the space between the metal lines. This means that the integration of an air cavity into the intra-metal dielectric region has a greater effect with higher aspect ratio interconnect structures. Extending the air-gap into the inter-layer dielectric region reduces the fringing field, resulting in an additional reduction in the



(a) Percent reduction in capacitance



(b) Effective dielectric constant

Figure 6.4.3 The effect of the space between metal lines and extended height of air-

gaps on the percent reduction in capacitance and  $k_{eff}$  (a) Percent

reduction in capacitance, (b) Effective dielectric constant



in the capacitance and  $k_{eff}$ . The capacitance at an aspect ratio of  $X=2.0$  ( $a=200$  nm) and an extension height ratio of  $Y=0.25$  ( $b=100$  nm) is reduced by 49% compared to a  $\text{SiO}_2$  only dielectric.

## 6.5 Results

### 6.5.1 Measured effective dielectric constants of Cu/air-gaps and extended

#### Cu/air-gaps interconnect structures

The single layer Cu/air-gap and extended Cu/air-gap structures using the tetracyclododecene (TD)-based thermally decomposable sacrificial polymer as a temporary placeholder between the Cu metal lines was fabricated. Figure 6.5.1 shows a cross-sectional secondary electron microscopic (SEM) image of an extended Cu/air-gap structure. The width and aspect ratio of the Cu lines were 210 nm and 1.8, respectively. The width of the air-gaps was 190 nm and the air-gap was extended into the top and bottom PECVD  $\text{SiO}_2$  layers by 80 nm and 100 nm, respectively. The SEM image shows that the TD-based polymer was cleanly decomposed leaving an air-cavity as the intra-level dielectric, without residual solids on the side walls of the copper. An interdigitated comb structure was fabricated and the measured capacitance values of the Cu/ $\text{SiO}_2$ , Cu/air-gap, and extended Cu/air-gap structures are summarized in Table 6.5.1. The dielectric constant of PECVD

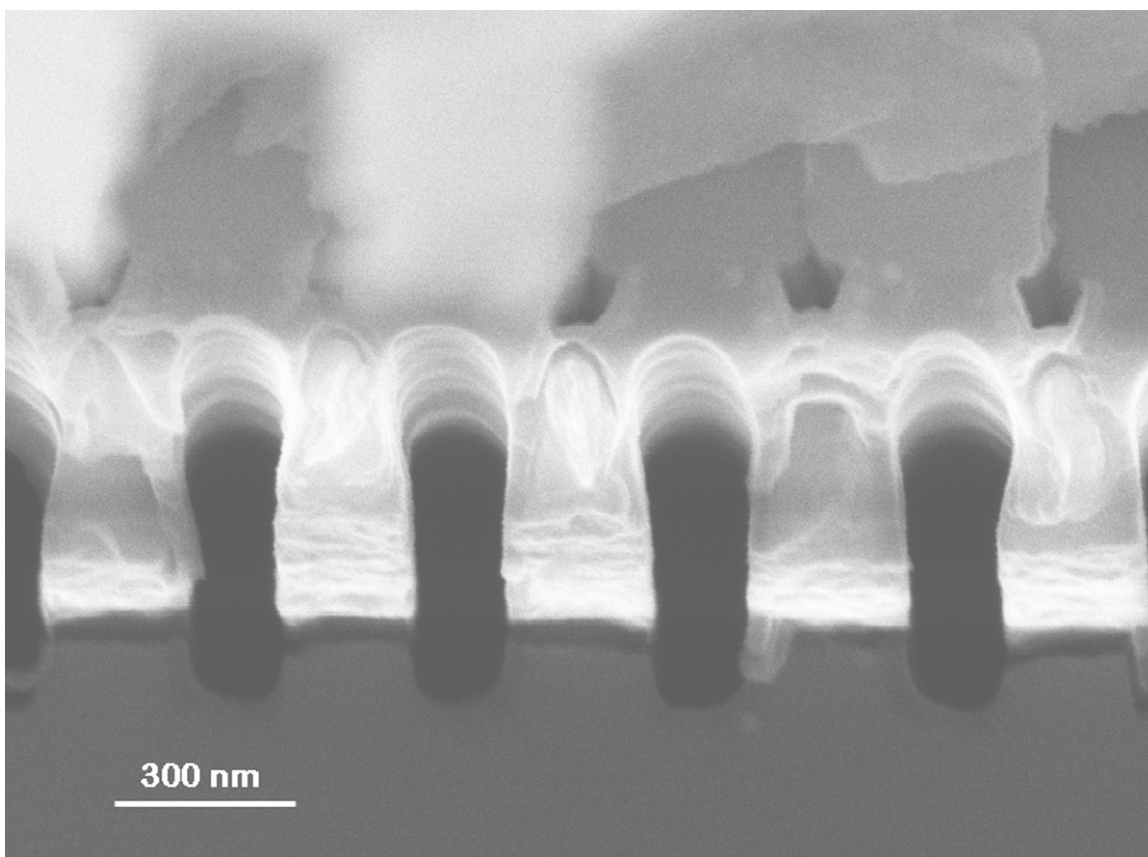
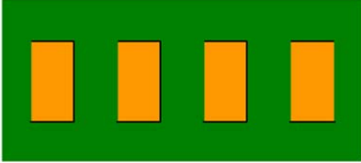
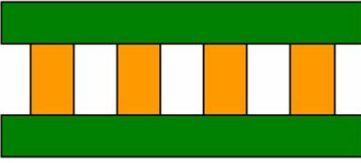
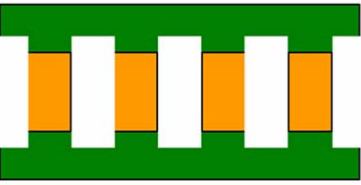


Figure 6.5.1 The cross sectional secondary electron microscopic image of extended Cu/air-gaps structure.

Table 6.5.1 The summary of the measured effective dielectric constants of the comb structure devices.

	Homogeneous Cu/SiO <sub>2</sub>	$k_{\text{eff}}=4.14$
	Cu/ air-gaps	$k_{\text{eff}}=2.42$
	Extended Cu/ air-gaps	$k_{\text{eff}}=2.17$

SiO<sub>2</sub> measured with a parallel plate capacitor was 4.14. Thus, the  $k_{eff}$  of the homogeneous SiO<sub>2</sub>/Cu interconnect was 4.14. The measured  $k_{eff}$  of Cu/air-gap and extended Cu/air-gap structures were 2.42 and 2.17, respectively. According to the 2006 ITRS [1], the required  $k_{eff}$  for a 32 nm technology node in 2013 is 2.1 to 2.4. As shown in Figure 6.4.2b, the electrostatic simulation of the dielectric constant for the low-k inter-layer dielectric material ( $\epsilon_r= 2.7$ ) instead of SiO<sub>2</sub> would lower  $k_{eff}$  below 1.9.

The thermal decomposition of the sacrificial polymer is a critical part of the air-gap formation. A multi-layered structure could have air-gaps in several layers. It is beneficial to decompose the sacrificial material at the end of build-up sequence and not after each layer. This was demonstrated in Figure 6.5.2 where a multi-layer interconnect structure with two layers of sacrificial polymer was fabricated. Both layers of sacrificial polymer were decomposed at one time. Two air-gap layers and two Cu layers are clearly shown and the sacrificial polymer in both layers was fully decomposed.

### 6.5.2 Effect of moisture uptake of extended Cu/air-gaps interconnect structures on the effective dielectric constant

The effect of moisture absorption on  $k_{eff}$  in the extended Cu/air-gap structures

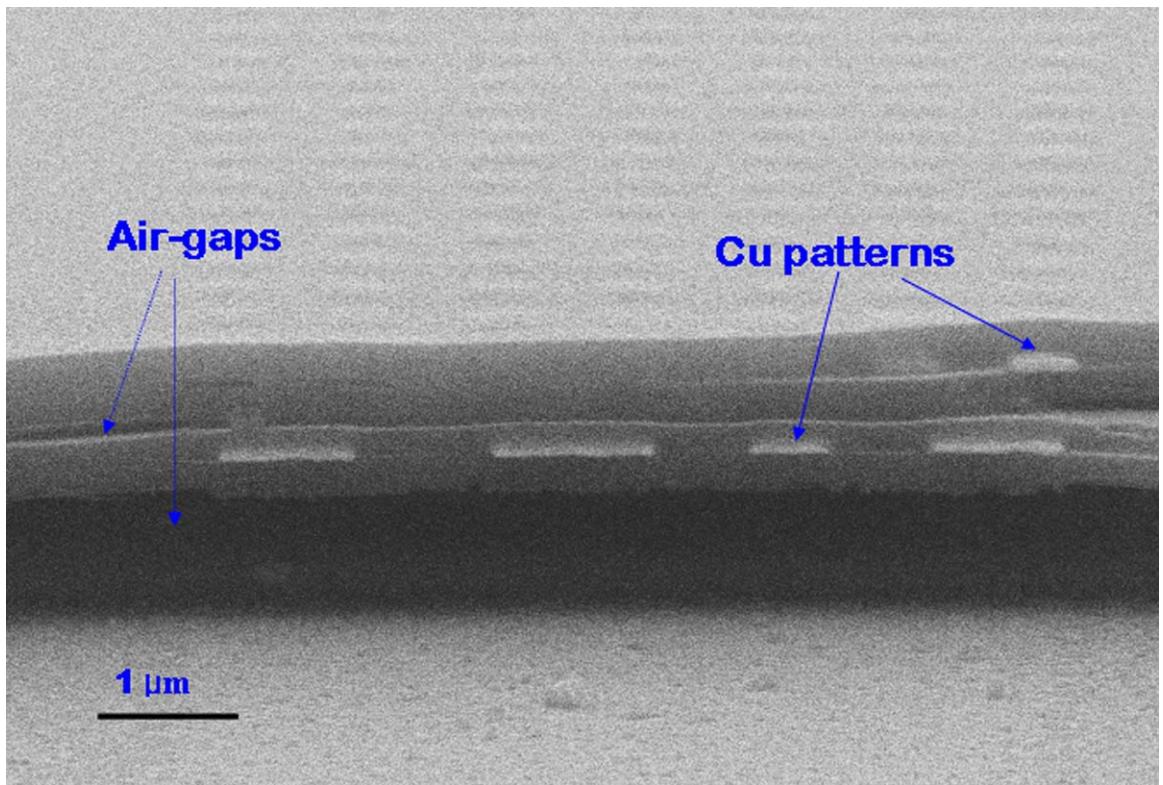


Figure 6.5.2 The cross sectional secondary electron microscopic image of multi-layer air-gaps and Cu patterns.

was studied. The results are shown in Figure 6.5.3. Increasing the relative humidity (RH) in the ambient air from 40% to 92%, at constant temperature, results in a 6.2% increase in  $k_{eff}$  (from 2.17 to 2.32) for the as-fabricated samples. According to a previous study [17], the walls of the cavity, after polymer decomposition, were hydrophobic. The inter-layer dielectric, including SiO<sub>2</sub>, are non-hermetic and allow air and moisture to permeate from the ambient.

Due to the high electric polarizability of water, the absorbed water significantly increases the effective dielectric constant and can lead to corrosion problems. In order to minimize an increase in capacitance with RH, the extended Cu/air-gap structure was made hydrophobic by reaction with hexamethyldisilazane (HMDS) vapor for 1 hr in vacuum. After exposure to the HMDS vapor, the  $k_{eff}$  of the extended Cu/air-gap structure decreased by 1.7%. When the HMDS treated sample was exposed to the highest RH,  $k_{eff}$  increased by only 0.3% above the initial condition, as shown in Fig. 6.5.4 [61,62]. During the HMDS process, surface hydroxides react with HMDS resulting in an alkyl-terminated surface which is hydrophobic. In a similar way, HMDS has been used to repair damage within porous low-k materials and terminating the surface with a trimethyl siloxane moiety [63,64]. The equivalent thickness of water responsible for the change in  $k_{eff}$  can be estimated by the electrostatic simulation. One would need 3.1 Å of water to account

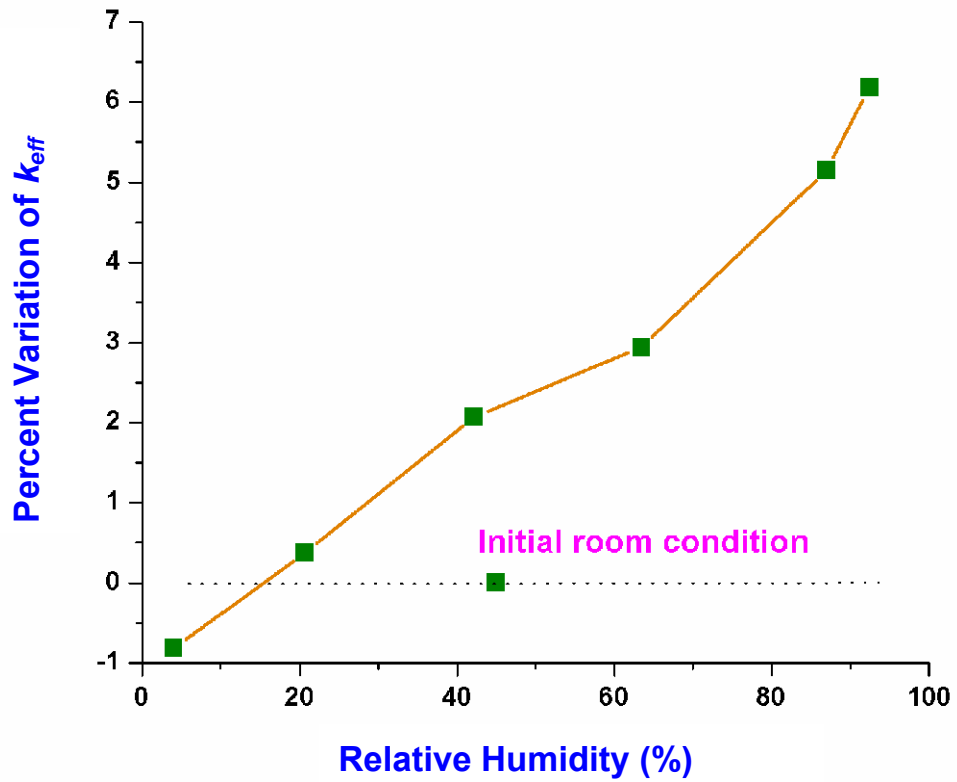


Figure 6.5.3 The effect of moisture uptake of extended Cu/air-gap interconnect structures on the  $k_{eff}$ .

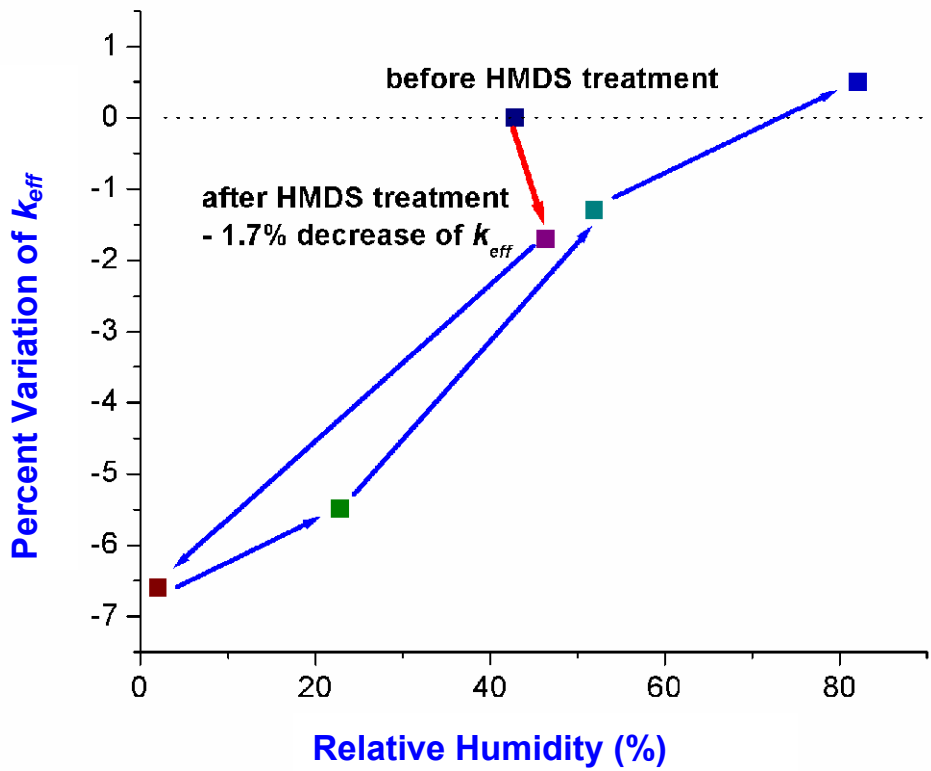


Figure 6.5.4 The effect of HMDS vapor treatment on the  $k_{eff}$  of extended Cu/air-gap interconnect structures.



accounting for a 1.7 % reduction of the  $k_{eff}$ . This is about 1.5 monolayers of water, assuming the bulk value of  $k$  for water.

## 6.6 Discussion

### 6.6.1 Dual damascene Cu/air-gap process

The insulator-first process is preferred in the Damascene fabrication process, vs. the copper-first process used here. Figure 6.6.1 shows a proposed via-first dual damascene fabrication process for Cu/air-gap structures using a thermally decomposable sacrificial polymer. After completing the lower interconnect layer (Figure 6.6.1a), an inter-layer dielectric (the via hole layer) is deposited followed by spin-coating the sacrificial polymer. A low- $k$  dielectric is preferred, such as SiCOH ( $\epsilon_r = 2.7$ ) for the inter-layer dielectric. The inorganic nature of SiCOH also provides a convenient etch-stop for the patterning of the lines (above the via-level). A thin SiO<sub>2</sub> or SiCOH hard mask is deposited on the spin-coated sacrificial polymer, and SiCOH is preferred due to its low dielectric constant vs. SiO<sub>2</sub>. This is followed by via-hole lithography and etching as shown in Figure 6.6.1b. A self-aligned capping layer such as CoWP or CuSiN on top of the lower copper lines is used as an etch stop for dry etching the inter-layer dielectric material for the via holes. After stripping the resist, a bottom anti-reflection coating (BARC) material is spin-coated

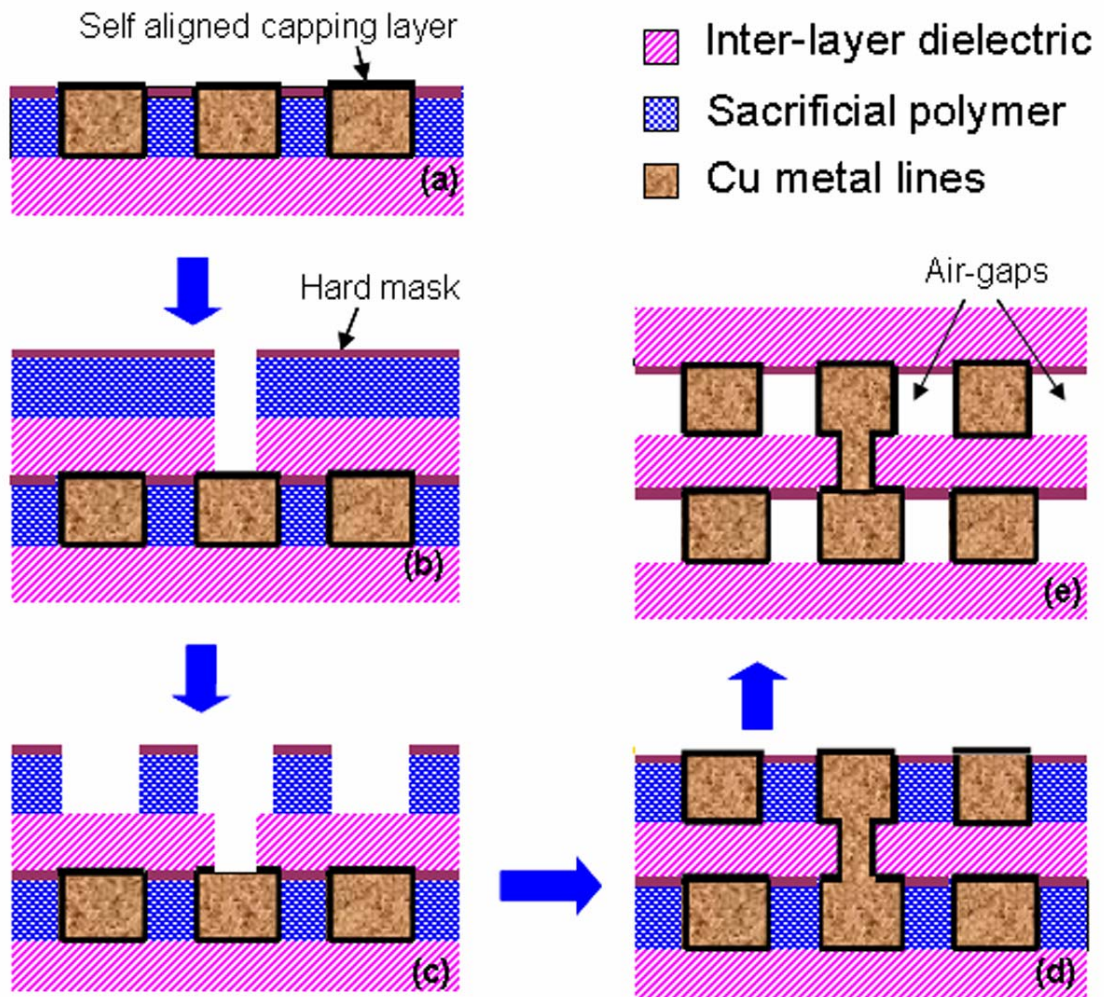


Figure 6.6.1 The proposed fabrication processes flow for Cu/air-gap interconnect structure using dual damascene processes.

to fill the via holes and protect them from the trench etch process. After trench patterning in Figure 6.6.1c, the metal barrier layer and Cu seed layer are deposited, followed by copper superfilling. The excess Cu is removed by CMP and the hard mask on top of the sacrificial polymer is used as a CMP stop-layer as shown in Figure 6.6.1d. After deposition of the self-aligned capping layer on top of the Cu lines, the last two steps are the deposition of the top inter-layer dielectric and thermal decomposition of the sacrificial polymer (Figure 6.6.1e), forming the Cu/air-gap structures. In the fabrication processes, high aspect ratio and anisotropic sacrificial polymer patterns are required. The sacrificial polymer needs survive the CMP step. Thus, a hard, sacrificial polymer is preferred. It was shown that the TD-based sacrificial polymer is harder than the norbornene based sacrificial polymer, while the thermal properties of the two materials are the same [17].

Minimizing the residual material within the air-gap is important because it can degrade  $k_{eff}$ . If a large amount of residue remains, it can increase the leakage current, capacitance, and decrease the time-dependent dielectric breakdown. According to a previous study [17], the decomposition residue of the TD-based sacrificial polymer is less than 1% of the original polymer thickness. In addition, decreasing the background oxygen concentration in the thermal decomposition furnace reduces the residue [55]. Thus, it is expected that the effect of the decomposition residues on the

interconnect performance should be small.

### 6.6.2 Critical review of the different approaches for the integration of dual damascene air-gaps

Other via-first dual damascene air-gap processes using a spin-on thermal degradable sacrificial polymer as a placeholder and SiOC as an inter-layer dielectric have been published [18]. A simplified process flow is shown in Figure 6.6.2. Before spin-coating the sacrificial polymer, a via hole is formed in the SiOC inter-layer dielectric as shown in Figure 6.6.2a. Then, the sacrificial polymer is spin-coated and fills in the via holes. The sacrificial polymer filling the via hole is removed following trench lithography step (Figure 6.6.2b). This requires extra dry-etching time due to the thickness of the material being removed. The extra dry-etching time may change the critical dimensions of the polymer trench pattern in the via hole region due to undercutting and damage the SiOC inter-layer dielectric [65]. The next process steps are Cu metallization (Figure 6.6.2c) and thermal decomposition of the sacrificial polymer (Figure 6.6.2d). Compared to the conventional dual damascene, no additional lithography step and processes are required because the via holes are formed before spin-coating of the sacrificial polymer. This results in a decrease in the number of the process steps. The

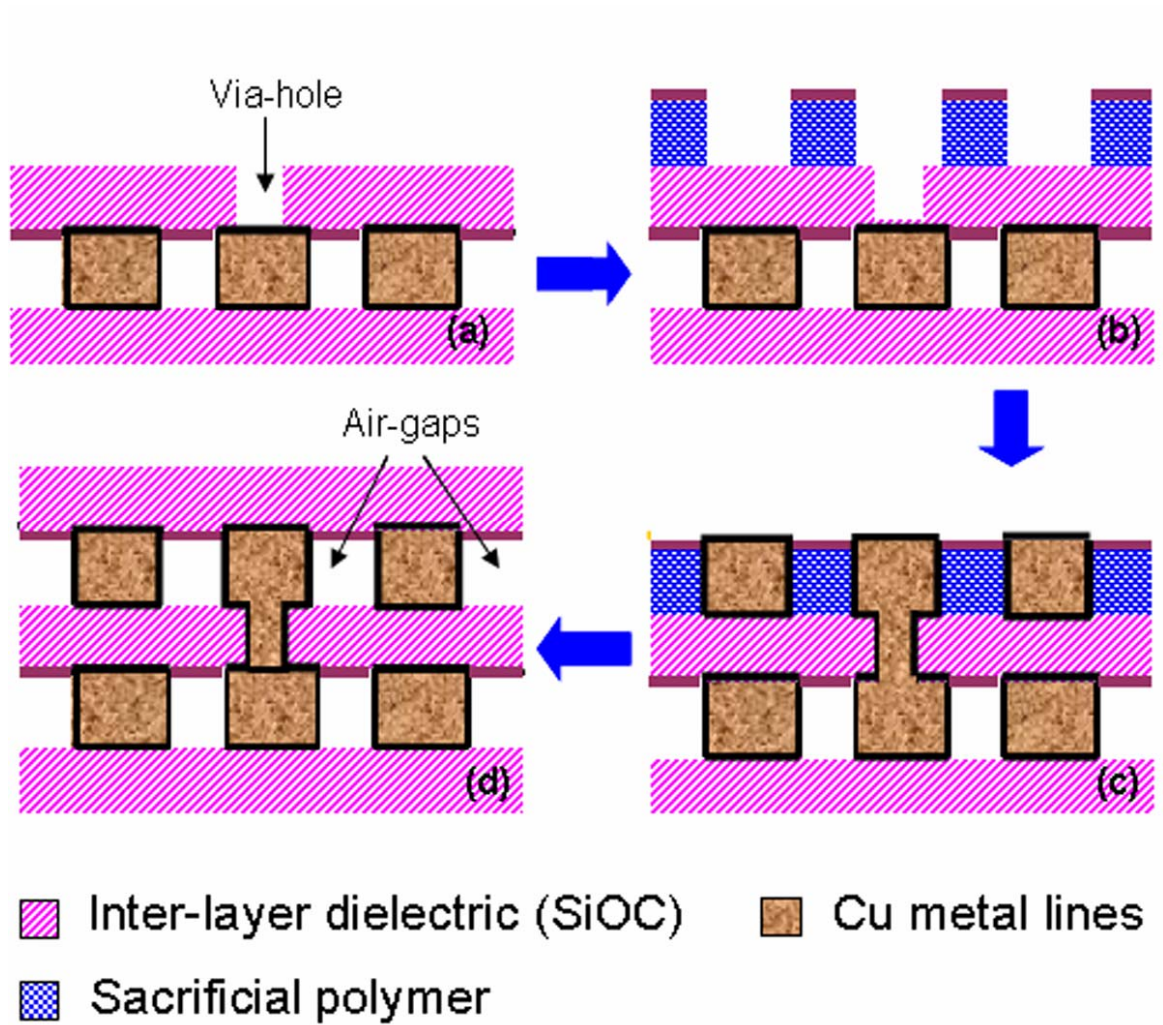


Figure 6.6.2. The process flow of an embedded via-first dual damascene air-gap

using a spin-on thermal degradable sacrificial polymer [31].

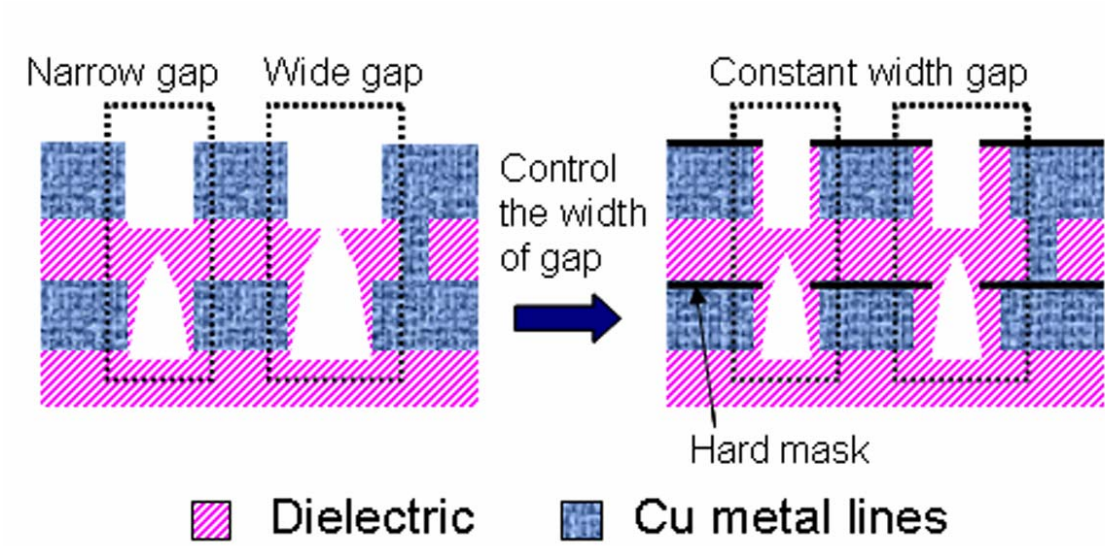
additional layers required are a hard mask on the sacrificial polymer for trench patterning, and a SiCN capping layer to protect Cu lines from the top dielectric layer. The challenges in this approach are the effect of decomposition residue and misalignment of via holes.

The integration of air-gaps in an intra-metal layer using wet etching of a SiO<sub>2</sub> intra-metal dielectric material has been demonstrated in a via-first dual damascene process [19]. The organic inter-layer dielectric is SiLK (Dow Chem. Co.). The dilute hydrofluoric acid solution penetrates into the interconnect structure and dissolves the SiO<sub>2</sub> intra-metal dielectric, while the organic SiLK inter-layer dielectric remains, as shown in Figure 6.1.1b. The additional layers in this approach include a SiC capping layer and a CuSiN self-aligned barrier on the top of the Cu lines. The SiC ( $\epsilon_r = 5.8$ ) capping layer on the top of the dual damascene structure is essential to preventing the diffusion of dilute HF etching solution into regions where it would damage the structure. The SiC raises  $k_{eff}$  of the interconnect structures because of its high dielectric constant. An additional lithography step is necessary to localize the air-gaps to specific regions. The complete removal of the HF etching solution from the interconnect structure can also be a challenge.

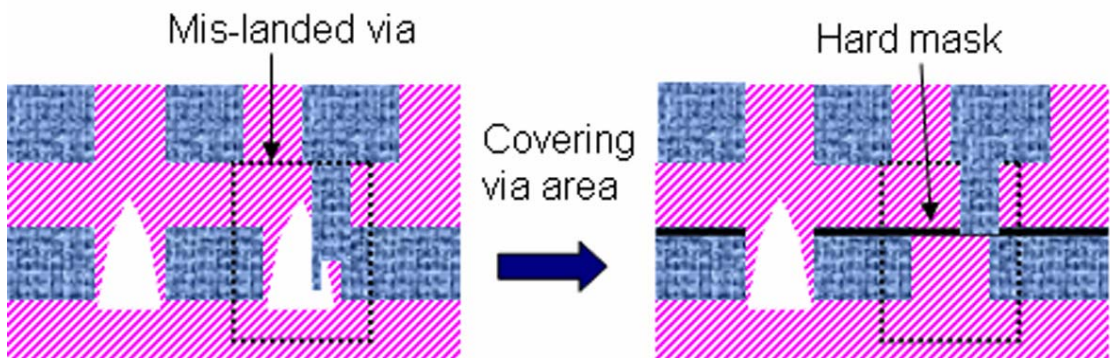
The integration approach of air-gaps using non-conformal deposition of an inter-level dielectric material in a via-first dual damascene process has been

demonstrated [20,21]. After finishing the via-first dual damascene process, the intra-metal dielectric in the dense region is etched back using an additional lithography step as shown in Figure 6.1.1c. Air-gaps are then formed during the non-conformal plasma deposition of an inter-layer dielectric. The plasma etching of the lines for the trench does not use an etch-stop layer. In addition, there is no etch-stop layer in the etch-back process of the intra-metal dielectric. Thus, the etch damage in the inter-layer dielectric may occur [65]. A process to repair the damaged low-k may be required [63-65]. An additional CMP step is required for the planarization of the non-conformal inter-layer dielectric. The air cavity occupies only a portion of the intra-layer dielectric region. The additional layers in this approach are a hard mask, a SiC dielectric liner, and a capping layer. The challenges in the integration of air-gaps by non-conformal deposition of an inter-layer dielectric are breakthrough of the air-cavities during trench etch into the via-level dielectric, and mis-landed vias due to misalignment [66,67], as shown in Figure 6.6.3. In order to avoid the breakthrough of air-cavities into the via-level dielectric during the process, the height of the air-gap is controlled using a hard mask and an additional lithography step. This controls the width of the etched-back area in the intra-metal dielectric region, as shown in Figure 6.6.3a [66]. In order to address the mis-landed via problem shown in Figure 6.6.3b, a hard mask and an additional lithography step are





(a) Breakthrough of air-gaps



(b) Mis-landed via due to misalignment

Figure 6.6.3. The challenges in the air-gap formation during non-conformal

deposition of the inter-layer dielectric (a) Breakthrough of air-gaps,

(b) Un-landed via due to misalignment.



used to exclude air-gaps from underneath the via holes [67]. In the etch back process of the intra-metal dielectric, the hard mask covers the via area and prevents the formation of air-gaps, resulting in the localization of the air-gaps in the desired area.

IBM has recently integrated air cavities into dielectrics [21]. After completing the dual damascene process, the SiCOH intra-metal dielectric in a desired region is selectively etched back using a thin oxide hard mask and an additional non-critical lithography step at the first metal layer and a nanoporous polymer is used. During the lithography step, the width of the etched area in between the Cu lines is kept constant, controlling the width and aspect ratio (H:W) of the air-gap trench. The air-gaps are formed by the non-conformal deposition of the upper SiCOH dielectric layer. Compared to the conventional dual damascene process, eight additional process steps are required. They include the deposition and removal of the hard mask, a non-critical lithography step, etch back of the intra-metal dielectric, and an additional CMP for planarization of the surface of the non-conformal SiCOH dielectric. The advantage of this approach is that no new materials are introduced and air-cavities can be inserted at any level. However, the dry etch damage in the SiCOH may increase the dielectric constant due to carbon depletion [65].

### 6.6.3 Dual Damascene extended Cu/air-gap process

The via-first dual damascene process to extend the air-cavity into the inter-layer dielectric regions is proposed in Figure 6.6.4. After formation of a via hole in Figure 6.6.4a, the trench pattern in the sacrificial polymer is developed by use of an additional lithography step. Then, a metal barrier and copper seed layer are deposited. The wafer is then planarized, and a self-aligned capping layer is deposited as shown in Figure 6.6.4b. After the deposition of the self-aligned capping layer on the top of the copper lines, the sacrificial polymer is stripped by dry or wet etching and the copper lines remain. The remaining Cu lines are used as a hard mask during the etching of the lower inter-layer dielectric to extend the air-gaps into the dielectric layer, as shown in Figure 6.6.4c. Then, a sacrificial polymer is spin-coated and a thin, hard-mask layer is deposited. Gap fill between the copper lines is not likely an issue for the sacrificial polymer because it will be removed in the final thermal decomposition step. In the fabrication of extended air-gaps in Figure 6.2.2c, the surface of the spin-coated sacrificial polymer layer was planarized and no additional CMP step was needed. The thickness of the sacrificial polymer on top of the Cu lines determines the extension height of the air-cavity into the top inter-layer dielectric. After deposition of the thin hard mask, a lithography step is needed to remove the sacrificial polymer from a top of the copper lines resulting in the

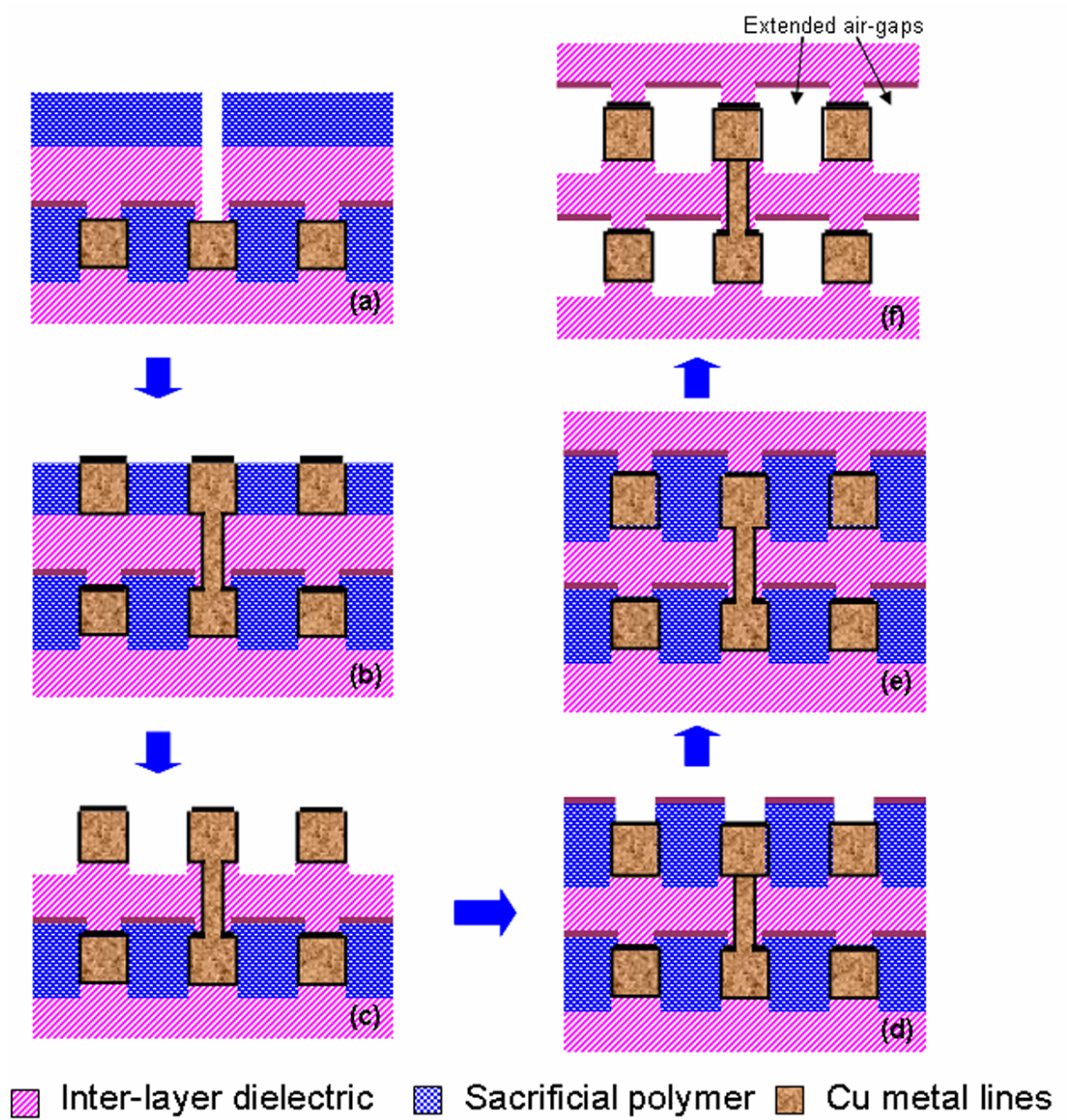


Figure 6.6.4. The proposed fabrication process flow for extended Cu/air-gap

interconnect structure using dual damascene processes.

extension of the air-cavity into the top inter-layer dielectric, as shown in Figure 6.6.4d. In this step, the width of the etched sacrificial polymer pattern above the Cu lines should be smaller than the width of the Cu lines in order to avoid over-etching of the sacrificial polymer. The final process step is the thermal decomposition of the sacrificial polymer in the intra-metal dielectric region (Figure 6.6.4f). Compared to the dual damascene air-gap process in Figure 6.6.1, the additional process steps are etched back at the bottom of the inter-level dielectric layer in Figure 6.6.4c. The sacrificial polymer, on the top of the Cu lines, is removed (Figure 6.6.4d) to extend the air-gap into the inter-layer dielectric region.

## **6.7 Conclusions**

The advantages of the air-gaps as an ultra low-k dielectric and methods of fabrication are presented. The integration of air-gaps or extended air-gaps with low-k inter-level dielectrics could satisfy the requirement for 32 nm node and beyond.

The measured effective dielectric constants of Cu/air-gap (200 nm half pitch and aspect ratio of 1.8) and extended air-gap (extended height of 80 nm on top and 100 nm on the bottom) was 2.42 and 2.17, respectively. Adsorbed moisture increased the capacitance by 7%. However, exposure to HMDS vapor removed the moisture and made the interconnect hydrophobic, resulting in only 0.3% increase at

the highest RH. The fabrication processes of Cu/air-gap structures and extended air-gap using the TD-based thermally decomposable polymers with a dual damascene processes were proposed and compared to other integration approaches.

## CHAPTER 7: CONCLUSIONS

### 7.1 Conclusions of the dissertation

This research has focused on the characterization of thermally decomposable sacrificial polymers and decomposition residues, and the fabrication and characterization of air-gaps and extended air-gaps as an ultra low intra-metal dielectric material using the hard tetracyclododecene (TD) based sacrificial polymer.

Due to the requirement of a harder sacrificial polymer in terms of process reliability, a conventional thermally decomposable norbornene (NB) based sacrificial polymer was hardened by exposure to electron-beam. The effects of electron energy, dose, irradiation temperature, and operating gas on the thermal and mechanical properties of NB-based sacrificial polymer were investigated. The exposure to 5 keV and 10 keV electron beam crosslinked the sacrificial polymer and resulted in improved hardness. However, the thermal properties including thermal stability at 300 °C and amount of residue were degraded due to the oxidation of the polymer films. On the other hand, polymer thin films exposed to 1 keV electron beam became softer than unexposed polymer thin films, because chain scission was preferred to cross-linking. The addition of hydrogen in operating gas and post-exposure heat treatment were useful to reduce the oxidation of the irradiated

polymer thin films. Consequently, even though electron beam exposure could harden the NB-based sacrificial polymer thin films, the thermal properties were degraded after exposure. Therefore hardening polymer thin films by exposure to the electron beam is not desirable.

For the better process reliability, TD-based sacrificial polymer was compared with NB-based sacrificial polymer in terms of hardness, process repeatability and thermal properties. Nanoindentation experiments showed that the TD-based sacrificial polymer was harder than the NB-based polymer and demonstrated better reliability as verified by quantitative SEM image processing over 50 nm width lines. The thermal properties of the TD-based sacrificial polymer were similar to those of the NB-based sacrificial polymer. The surfaces of thin films and decomposition residue were hydrophobic. Thus, it was concluded that the TD-based polymer was a better sacrificial polymer than the NB-based polymer for use in the fabrication of nano-sized air-gaps.

A single layer Cu/air-gaps and extended Cu/air-gaps interconnect structures were fabricated using the lift-off Cu metallization process in order to demonstrate the advantage of the air-gaps and extended air-gaps as an ultra low-k intra-metal dielectric on the reduction of interconnect capacitance. The width and aspect ratio of Cu lines were 210 nm and 1.8, respectively. The half pitch of Cu/air-gaps

interconnect was 200 nm. For the extended air-gaps, air-gaps were extended by 80 nm on top and 100 nm at the bottom SiO<sub>2</sub> inter-layer dielectric. Compared to  $k_{eff} = 4.14$  for the homogeneous PECVD Cu/SiO<sub>2</sub> structure, the measured  $k_{eff}$  of Cu/air-gaps and extended Cu/air-gaps structures were 2.42 and 2.17, respectively and the measured values of  $k_{eff}$  satisfied the requirement for 32 nm node technology and beyond [1]. Thus, the advantages of the air-gaps and extended air-gaps on the reduction of interconnect capacitance were confirmed.

Moisture uptake of interconnect structures can give rise to integration reliability issues, including corrosion of Cu lines, an increase of leakage current and interconnect capacitance. Thus, the effect of moisture uptake of extended Cu/air-gaps interconnect on  $k_{eff}$  and interconnect capacitance was investigated. As the relative humidity (RH) increased from 4% to 92%, the  $k_{eff}$  increased by 7% due to high dielectric constant of water. In order to remove the absorbed moisture and make the interconnect hydrophobic, the extended Cu/air-gaps interconnect structures were exposed to hexamethyldisilazane (HMDS) vapor. After exposure to HMDS vapor, the  $k_{eff}$  of extended Cu/air-gaps interconnect decreased by 1.7% due to removal of the absorbed moisture. At a RH of 86%, the  $k_{eff}$  of the HMDS treated extended air-gap increased only by 0.3% because of hydrophobic surface of the interconnect. As a result, the exposure to HMDS vapor successfully removed the



absorbed moisture and resulted in the formation of a hydrophobic extended Cu/air-gap interconnect structure. .

For the integration of air-gaps and extended air-gaps in an intra-metal layer, a dual damascene air-gap and extended air-gap processes instead of lift-off Cu metallization were proposed. In addition, different integration approaches of air-gaps using dual damascene process were evaluated and compared in terms of production cost, process complexity and reliability. The integration of the air-gaps using thermally decomposable sacrificial polymer as a temporary placeholder needs two lithography steps for via and trench, and a CMP process.

The integration of air-gaps by selective wet etching of the SiO<sub>2</sub> intra-metal dielectric materials required three lithography steps for via, trench and etching solution pathway, and a CMP step was necessary. Furthermore, the existence of residual etching solution in the interconnect structures may cause the long-term reliability issues.

In addition, the use of non-conformal deposition of a inter-layer dielectric materials for the integration of air-gaps also had discoveries to the sacrificial polymer. It the had discovering required three lithography steps for via, trench and etch-back of the intra-metal dielectric, and two CMP processes for the planarization of damascene Cu layer and the upper inter-layer dielectric surface. Several more

processing steps compared to the conventional dual damascene processes were needed for etch back of the intra-layer dielectric materials in the desired, dense region. However, it has been advantages that no new material and process are introduced and the ability to add air-gaps as a “drop-in” to an existing on-chip interconnect process flow minimizes risks.

In conclusion, the use of the hard TD-based sacrificial polymer as a temporary placeholder in between metal lines can improve process reliability for the integration of the air-gaps. The advantages of integration of the air-gaps and extended air-gaps as an ultra low-k intra-metal dielectric material for advanced integrated circuits were verified both by electrostatic modeling and testing of fabricated air-gaps structures. The measured effective dielectric constants of the Cu/air-gaps and extended Cu/air-gaps satisfied the requirement for 32 nm node [1]. Compared to other integration approaches, the fabrication of air-gaps using sacrificial polymers has the advantages in terms of cost, process complexity. Therefore, I believe the air-gap technology as an ultra low-k intra-metal dielectric material must be a promising technique for the advanced integrated circuits.

## 7.2 Future work

In this study, the advantages of air-gaps and extended air-gaps were demonstrated by fabrication, characterization and modeling using TD-based sacrificial polymers. In order to realize air-gap technology for an ultra low-k intra-metal dielectric material, the following proposed future work is suggested.

It is proposed that the dual damascene air-gap process described in this thesis is used to fabricate Cu/air-gap multi-layer structure. For the multi-layer interconnect structures, the effect of air-gaps or extended air-gaps on the electrical performance of the interconnects should be investigated by electrical characterization of the fabricated structures. In addition, integration reliabilities such as leakage current, mean time to failure (MTTF) of electromigration and mechanical strength should be evaluated. From the fabrication of multi-layer Cu/air-gaps interconnect structures and evaluation of the integration reliabilities, the optimal processing parameters for the dual damascene air-gap processes using the harder TD-based sacrificial polymer will be determined.

As a longer term project, using the optimal processing parameters from the work described in the paragraph above, the air-gaps or extended air-gaps should be integrated into the real circuit devices. The effect of air-gap interconnect structures on the improvement of device performance should be investigated by evaluating RC

delay time, power dissipation and cross talk noise. Also, reliability tests should be performed, and the effect of operating temperature, moisture and resistance heat on the performance of the real circuit devices are evaluated.

## REFERENCES

- [1] International Technology Roadmap for Semiconductors, 2006
- [2] International Technology Roadmap for Semiconductors, 2005
- [3] Gordon E. Moore, "No Exponential is Forever ... but We Can Delay 'Forever'", International Solid State Circuits Conference (ISSCC), February 10, 2003.
- [4] IBM web site, "What is interconnect all about?",  
*<http://www-03.ibm.com/chips/about/technology/makechip/interconnect/2a.html>*,  
(accessed September 21, 2007)
- [5] Mark T. Bohr, "Interconnect Scaling- The Real limiter to High Performance ULSI", IEDM, 1995, p. 241.
- [6] Jeff A. Davis and James D. Meindl, "Length, Scaling, and Material Dependence of Crosstalk between Distributed RC Interconnects", IITC, 1999, p. 227-229.
- [7] Shekhar Borkar, "Design challenges of technology scaling", IEEE Micro, 19 (4), 1999, p. 23-29.
- [8] D. Edelstein, J. Heidenreich, R. Goldblatt, W. Cote, C. Uzoh, N. Lustig, P. Roper, T. McDevitt, W. Motsiff, A. Simon, J. Dukovic, R. Wachnik, H. Rathore, R. Schulz, L. Su, S. Luce, and J. Slattery, "Full Copper Wiring in a Sub-0.25 micron CMOS ULSI Technology," *Technical Digest, IEEE International Electron Devices Meeting*, 1997, p. 773.
- [9] D. C. Edelstein, G. A. Sai-Halasz, and Y.-J. Mii, "VLSI On-Chip Interconnection Performance Simulations and Measurements," *IBM J. Res. Develop.* **39**, No. 4, p. 383 (1995).
- [10] D. C. Edelstein, "Advantages of Copper Interconnects," *Proceedings of the 12th International IEEE VLSI Multilevel Interconnection Conference*, 1995, p. 301.

- [11] C. J. F. Böttcher, "Theory of electric polarization", Amsterdam, New York, Elsevier Scientific Pub. Co., 1973.
- [12] Application Note 1217-1, "Basics of measuring the dielectric properties of materials," Hewlett Packard literature number 5091-3300E, 1992.
- [13] N.P. Hacker, G. Davis, L. Figge, and T. Krajewski, "Properties of new low dielectric constant spin-on-silicon oxide based polymers," in *Proc. MRS Symp. Low Dielectric Constant Materials III*, vol. 476, C. Case, P. Kohl, T. Kikkawa, and W. Lee, Eds., 1997, p. 25.
- [14] Y. Ohoka, Y. Ohba, A. Isobayashi, N. Komai, S. Arakawa, R. Kanamura and S. Kadomura, "Integration of High Performance and Low Cost Cu/Ultra Low-k SiOC (k=2.0) Interconnects with Self-formed Barrier Technology for 32nm-node and Beyond", *2007 IITC, San Francisco*, p 67~69.
- [15] M. Aimadeddine, V. Jousseau, V. Arnal, L. Favennec, A. Farcy, A. Zenasni, M. Assous, M. Vilmy, S. Jullian, P. Maury, V. Delaye, N. Jourdan, T. Vanypre, P. Brun, G. Imbert, Y. LeFric, M. Mellier, H. Chaabouni, L.L. Chapelon, K. Hamioud, F. Volpi, D. Louis, G. Passemard, J. Torres, "Robust integration of an ULK SiOCH dielectric (k=2.3) for high performance 32nm node BEOL", *2007 IITC, San Francisco*, p 175 ~ 177.
- [16] P.A. Kohl, D.M. Bhusari, M. Wedlake, F.P. Klemens, J. Miner, B. C. Lee, R.J. Gutmann, "Air-gaps in 0.3 $\mu$ m electrical interconnections", *IEEE EDL*, 21, n°12, 2000, p. 557-559
- [17] Seongho Park, Jeff Krotine, Sue Ann Bidstrup Allen, Paul A. Kohl, "Fabrication of Intra-level Extended Air-Gaps using the harder Sacrificial Polymer Placeholder for Ultra Low-k Dielectrics", *2007 VMIC, Fremont CA*.
- [18] R. Daamen, P.H.L. Bancken, D. Ernur Badaroglu, J. Michelon, V.H. Nguyen, G.J.A.M. Verheijden, A. Humbert, J. Waterloos, A. Yang, J.K. Cheng, L. Chen, T. Martens, R.J.O.M. Hoofman, "Multi-Level Air-Gap Integration for 32/22nm nodes using a Spin-on Thermal Degradable Polymer and a SiCO CVD Hard Mask", *2007 IITC, San Francisco*, p 61~63.

- [19] L.G. Gosset, F. Gaillard, D. Bouchu, R. Gras, J. de Pontcharra, S. Orain, O. Cueto, Ph. Lyan, O. Louveau, G. Passemard, J. Torres, "Multi-Level Cu Interconnects Integration and Characterization with Air Gap as Ultra-Low K Material Formed using a Hybrid Sacrificial Oxide / Polymer Stack", *2007 IITC, San Francisco*, p.58~60.
- [20] T. Harada, A. Ueki, K. Tomita, K. Hashimoto, J. Shibata, H. Okamura, K. Yoshikawa, T. Iseki, M. Higashi, S. Maejima, K. Nomura, K. Goto, T. Shono, S. Muranka, N. Torazawa, S. Hirao, M. Matsumoto, T. Sasaki, S. Matsumoto, O. Ogawa, M. Fujisawa, A. Ishii, M. Matsuura, T. Ueda, "Extremely Low Keff (~1.9) Cu Interconnects with Air Gap Formed Using SiOC", *2007 IITC, San Francisco*, p. 141~143.
- [21] IBM, "IBM Brings Nature to Computer Chip Manufacturing", *IBM's press release*, Armonk, NY, 03 May 2007.
- [22] R.A. Shick, B.L. Goodall, L.H. McIntosh, S. Jarayaman, P.A. Kohl, S.A. Bidstrup-Allen and N.R. Grove, "New Olefinic Interlevel Dielectric Materials for Multi-Chip Modules", *IEEE MCMC*, 1996, p. 182-187.
- [23] Nicole R. Grove, Paul A. Kohl, Sue Ann Bidstrup Allen, Saikumar Jayaraman and Robert Shick, "Functionalized Polynorbornene Dielectric Polymers: Adhesion and Mechanical Properties", *Journal of Polymer Science: Part B: Polymer Physics*, 1999, 37, p. 3003-3010.
- [24] Michael D. Wedlake and Paul A. Kohl, "Thermal decomposition kinetics of functionalized polynorbornene", *J. Mater. Res.*, 2002, 17(3), p. 632-640.
- [25] S.H. Park, J. Krotine, S.A. Bidstrup, P.A. Kohl, "Air-gaps for ultra low-k interconnects fabricated with hardened sacrificial polymer", the 208<sup>th</sup> ECS conference, Los Angeles, California, Oct. 2005.
- [26] R.H. Havemann and Shin-puu Jeng, "Multilevel Interconnect Structure with Air gaps Formed Between Metal Leads", 1995, U.S. patent No 5,461,003.
- [27] M.B. Anand, M. Yamada and H. Shibata, "NURA: A Feasible, Gas-Dielectric Interconnect Process", 1996 Symposium on VLSI Technology Digest of Technical Papers, p. 82.

- [28] M.B. Anand, M. Yamada and H. Shibata, "Use of Gas as Low-k Interlayer Dielectric in LSI's: Demonstration of Feasibility", IEEE Transactions on electron devices, 1997, 44(11), p. 1965-1971.
- [29] B.P. Shieh, L.C. Bassman, D.-K. Kim, K.C. Saraswat, M.D. Deal, J.P. McVittie, R.S. List, S. Nag, and L. Ting, "Integration and Reliability Issues for Low Capacitance Air-Gap Interconnect Structures", 1998 IITC, p. 125-127.
- [30] Paul A. Kohl, Qiang Zhao, Kaushal Patel, Douglas Schmidt, Sue Ann Bidstrup-Allen, Robert Shick, and S. Hayaraman, "Air-Gaps for Electrical Interconnections", Electrochemical and Solid-State Letters, 1998, 1(1), p. 49-51.
- [31] Xiaoqum Wu, Hollie A. Reed, Yong Wang, Larry E. Rhodes, Ed Elce, R. Ravikiran, Robert A. Shick, Clifford L. Henderson, Sue Ann Bidstrup Allen, and Paul A. Kohl, "Fabrication of Microchannels Using Polynorbornene Photosensitive Sacrificial Materials", Journal of Electrochemical Society, 2003, 150(9), p. H205-H213.
- [32] Nicole R. Grove, Paul A. Kohl, Sue Ann Bidstrup Allen, Saikumar Jayaraman, and Robert Shick, "Functionalized Polynorbornene Dielectric Polymers: Adhesion and Mechanical Properties", Journal of Polymer Science, 1999, 37, p. 3003-3010.
- [33] SeongHo Park, Jeff Krotine, Sue Ann Bidstrup Allen, and Paul A Kohl, "Electron-beam hardening of thin films of functionalized polynorbornene copolymer", Journal of Electronic Materials, 2006, 35(5), p. 1112-1121.
- [34] L.G. Gosset, V. Arnal, P. Prindle, R. Hoofman, G. Verheijden, R. Daamen, L. Broussous, F. Fusalba, M. Assous, R. Chatterjee, J. Torres, D. Gravestejin, and K.C. Yu, "General review of issues and perspectives for advanced copper interconnects using air-gap as ultra low-K material", 2003 IITC, p. 65-67.
- [35] L.G. Gosset, A. Farcy, J. de Pontcharra, Ph. Lyan, R. Daamen, G.J.A.M. Verheijden, V. Arnal, F. Gaillard, D. Bouchu, P.H.L. Bancken, T. Vandewyer, J. Michelon, V. Nguyen Hoang, R.J.O.M. Hoofman, and J. Torres, "Advanced Cu interconnects using air gaps", Microelectronic Engineering, 2005, 82, p. 321-332.



- [36] B. Shieh, K.C. Saraswat, J.P. McVittie, S. List, S. Nag, M. Islamraja, and R. H. Havemann, "Air-Gap Formation During IMD Deposition to Lower Interconnect Capacitance", IEEE Electron Device Letters, 1998, 19(1), p. 16-18.
- [37] Tetsuya Ueda, Eiji Tamaoka, Kyoji Yamashita, Nobuo Aoi and Shuichi Mayumi, "A Novel Air Gap Integration Scheme for Multi-level Interconnects using Self-aligned Via Plugs", 1998 Symposium on VLSI Technology Digest of Technical Papers, p. 46-47.
- [38] V. Arnal, J. Torres, Ph. Gayet, M. Haond, Ch. Vérove, B. Descouts, Ph. Spinelli, in Proceedings of the AMC, 2000, p. 71-86.
- [39] V. Arnal, J. Torres, Ph. Gayet, R. Gonella, Ph. Spinelli, M. Guillermet, Ch. Vérove, in Proceedings of the IITC 2001, p. 298-300.
- [40] V. Arnal, J. Torres, J.-Ph. Reynard, Ph. Gaillet, Ch. Vérove, M. Guillermet, Ph. Spinelli, "Optimization of CVD dielectric process to achieve reliable ultra low-k air-gaps", Microelectronic Engineering, 60 (2002), p. 143-148.
- [41] L.G. Gosset, V. Arnal, Ph. Brun, M. Broekaart, C. Monget, N. Casanova, M. Rivoire, J.-C. Oberlin, J. Torres, "Integration SiOC air-gaps in copper interconnects", Microelectronic Engineering, 70 (2003), p. 274-279.
- [42] J.-P. Gueneau De Mussy, G. Beyer, K. Maex, in: E. Zschech, C. Whelan, T. Mikolajick, Materials for information technology, Springer, 2005.
- [43] F. Gaillard, J. de Pontcharra, L.G. Gosset, Ph. Lyan, D. Bouchu, R. Daamen, O. Louveau, P. Besson, G. Passemard, J. Torres, "Chemical etching solutions for air-gap formation using a sacrificial oxide/polymer approach", Microelectronic Engineering, 83 (2006), p. 2309-2313.
- [44] T. Y. Tsui, G. M. Pharr, "Substrate effects on nanoindentation mechanical property measurement of soft films on hard substrates", Journal of Materials Research, 14(1), p. 292 - 301, 1999.
- [45] The National Technology Roadmap for semiconductors, Semiconductor Industry Association, San Jose, CA, 1997.

- [46] International Technology Roadmap for Semiconductors, 2001.
- [47] N.P. Hacker, G. Davis, L. Figge, and T. Krajewski, "Properties of new low dielectric constant spin-on-silicon oxide based polymers," in *Proc. MRS Symp. Low Dielectric Constant Materials III*, vol. 476, C. Case, P. Kohl, T. Kikkawa, and W. Lee, Eds., 1997, p. 25.
- [48] Punit Chiniwalla, Yiqun Bai, Edmund Elce, Robert Shick, W. Christopher McDougall, Sue Ann Bidstrup Allen, and Paul A. Kohl, "Crosslinking and decomposition reactions of epoxide functionalized polynorbornene. Part I. FTIR and thermogravimetric analysis", *J. Appl. Poly. Sci.*, vol. 89, 2003, p. 568-577.
- [49] J. I. Goldstein, D. E. Newbury, P. Echlin, D.C. Joy, C. Fiori, and E. Lifshin, "*Scanning Electron Microscopy and X-ray Microanalysis*", Plenum Press, NY, 1981.
- [50] P. Fouassier, J.F. Rabek, "*Radiation curing in polymer science and technology*", Elsevier Applied **Science**, NY, 1993.
- [51] Rahul Manepalli, Kimberly D. Farnsworth, Sue Ann Bidstrup Allen, and Paul A. Kohl, "Multilayer electron-beam curing of polymer dielectric for electrical interconnections", *Electrochemical and Solid-State Letters*, vol. 3(5), 2000, p. 228.
- [52] Rahul N. Manepalli, "Electron beam curing of thin film polymer dielectrics", Dissertation, Georgia Institute of Technology, 2000.
- [53] TriboIndenter user's manual, Hysistron Inc., 2001.
- [54] Robert P. Lattimer, "Pyrolysis field ionization mass spectrometry of hydrocarbon polymers", *Journal of Analytical and Applied Pyrolysis*, vol. 39, 1997, p. 115-127.
- [55] Nicole R. Grove, "Characterization of functionalized polynorbornenes as interlevel dielectrics", Dissertation, Georgia Institute of Technology, 1997.

- [56] G. Khanarian, and Hoechst Celanese, "Optical properties of cyclic olefin copolymers", *Opt. Eng.*, 40, p. 1024-1029, 2001.
- [57] McNally, D, "Uses and processing of cyclic olefin copolymers", *PLASTICS ENGINEERING*, 56(6), p. 51, 2000.
- [58] W.C. Oliver, G.M. Pharr, "An improved technique for determining hardness and elastic modulus using load and displacement sensing indentation experiments", *Journal of Materials Research*, 7(6), p. 1564, 1992.
- [59] "Methods of Surface Characterization-Volume 5: Beam Effects, Surface Topography, and Depth Profiling in Surface Analysis", Alvin W. Czanderna, Theodore E. Madey and Cedric J. Powell, Kluwer Academic Publishers, 2002.
- [60] Peter Sigmund, "Theory of Sputtering. I. Sputtering Yield of Amorphous and Polycrystalline Targets", *Physical Review*, 1969, 184(2), p. 383-416.
- [61] Y. Uchida, S. Hishiya, N. Fujii, K. Kohmura, T. Nakayama, H. Tanaka, and T. Kikkawa, "Effect of moisture adsorption on the properties of porous-silica ultra low-k films", *Microelectronic Engineering*, 2006, 83, p. 2126-2129.
- [62] Dow Corning, "A guide to Silane Solutions".
- [63] T. Rajagopalan, B. Lahlouh, J.A. Lubguban, N. Biswas, S. Gangopadhyay, J. Sun, D.H. Huang, S.L. Simon, D. Toma and R. Butler, "Investigation on hexamethyl-disilazane vapor treatment of plasma-damaged nanoporous organosilicate films", *Applied Surface Science*, 2006, 252, p. 6323-6331.
- [64] T.C. Chang, Y.S. Mor, P.T. Liu, T.M. Tsai, C.W. Chen, Y.J. Mei and S.M. Sze, "Recovering Dielectric Loss of Low Dielectric Constant Organic Siloxane during the Photoresist Removal Process", *Journal of The Electrochemical Society*, 2002, 149 (8), p. F81-F84.
- [65] O. Richard, F. Iacopi, H. Bender and G. Beyer, "Sidewall damage in silica-based low-*k* material induced by different patterning plasma processes studied by energy filtered and analytical scanning TEM", *Microelectronic Engineering*, 2007, 84(3), p. 517-523.

- [66] R. Daamen, P.H.L. Bancken, V.H. Nguyen, A. Humbert, G.J.A.M. Verheijden and R.J.O.M. Hoofman, "The evolution of multi-level air-gap integration towards 32 nm node interconnects", *Microelectronic Engineering*, 2007, 84, p. 2177-2183.
- [67] J. Noguchi, T. Oshima, T. Matsumoto, S. Uno, K. Sato, N. Konishi, T. Saito, M. Miyauchi, S. Hotta, H. Aoki, T. Kikuchi, K. Watanabe, K. Kikushima, "Misalignment-Free Air-gap (MFAG) Interconnect with Via Base Structure for 45/65 nm node and below", 2006 IITC, p. 167-169.
- [68] PHI X-ray Photoelectron Spectroscopy handbook (Physical Electronics Co.)
- [69] CAMECA web page : <http://www.cameca.fr/html/static.html> (accessed October 15, 2007)